THE EFFECT OF A WAKE-MOUNTED SPLITTER PLATE ON THE FLOW AROUND A SURFACE-MOUNTED FINITE-HEIGHT SQUARE PRISM

A Thesis Submitted

to the College of Graduate Studies and Research

in Partial Fulfilment of the Requirements

for the Degree of Master of Science

in the Department of Mechanical Engineering,

University of Saskatchewan

Saskatoon, Saskatchewan, Canada

By

Ayodele Rufus Ogunremi

PERMISSION TO USE

I agree that the Libraries of the University of Saskatchewan can make this thesis available for inspection. Permission for copying of this thesis in any manner, in whole or in part, for scholarly purposes may be granted by my supervisor, Prof. D. Sumner, the Head of the Department of Mechanical Engineering, or the Dean of the College of Graduate Studies and Research. It is understood that any copying or publication or use of this thesis, or parts thereof, for financial gain is prohibited without my written permission. Proper recognition shall be given to me and to the University of Saskatchewan in any scholarly use which may be made of any material in my thesis.

Requests for permission to copy or to make other use of material in this thesis, in whole or part, should be addressed to:

Head of the Department Mechanical Engineering,

University of Saskatchewan,

57 Campus Drive,

Saskatoon, Saskatchewan, S7N 5A9

Canada

ABSTRACT

The flow around a finite square prism has not been studied extensively when compared with an “infinite” (or two-dimensional) square prism. In the present study, the effect of a wake-mounted splitter plate on the flow around a surface-mounted square prism of finite height was investigated experimentally using a low-speed wind tunnel. Of specific interest were the combined effects of the splitter plate length and the prism’s aspect ratio on the vortex shedding, mean drag force coefficient, and the mean wake. Four square prisms of aspect ratios AR = 9, 7, 5 and 3 were tested at a Reynolds number of Re = 7.4×10^4 and a boundary layer thickness of δ/D = 1.5. Splitter plate lengths of L/D = 1, 1.5, 2, 3, 5, and 7, were tested, with all plates having the same height as the prism. Measurements of the mean drag force were obtained with a force balance, and measurements of the vortex shedding frequency were obtained with a single-component hot-wire probe. A seven-hole pressure probe was used to measure the time-averaged wake velocity at a Reynolds number of Re = 3.7×10^4 for AR = 9 and 5 with splitter plates of lengths L/D = 1, 3, 5, and 7. These measurements were carried out to allow for a better understanding of how the splitter plate affects the mean wake of the finite prism.

The results show that the splitter plate is a less effective drag-reduction, but more effective vortex-shedding-suppression, device for finite square prisms than it is for infinite square prisms. Significant reduction in the mean drag coefficient was realized only for short prisms (of AR $\leq$ 5) when long splitter plates (of $L/D \geq 5$) were used. A splitter plate of length L/D = 3 was able to suppress vortex shedding for all aspect ratios tested. However, for square prisms of aspect ratios AR $\leq$ 7, the splitter plate is a less effective vortex-shedding-suppression device when compared to its use with finite circular cylinders, i.e. longer splitter plates are needed for vortex shedding suppression with square prisms. Wake measurements showed distinct wake velocity fields for the two prisms tested. For the prism of AR = 9, a

strong downwash flow in the upper part of the wake became weaker towards the ground plane. For the prism of AR = 5, the downwash remained strong close to the ground plane. With splitter plates installed, the downwash became weaker for both prisms. The splitter plate was found to narrow the wake width, especially close to the ground plane, and led to the stretching of the streamwise vortex structures in the vertical direction, and increased entrainment towards the wake centreline in the cross-stream direction.

ACKNOWLEDGMENTS

I would like to appreciate my supervisor, Prof. D. Sumner, for his advice, support, guidance and insight throughout the research program. Thanks for giving me this research opportunity. The technical assistance of Mr. Dave Deustcher and Engineering Shops is well acknowledged and appreciated. Many thanks to my advisory committee members, Prof. J.D. Bugg and Prof. D.J. Bergstrom, for their positive criticisms, useful comments and suggestions that helped improve my research. I want to acknowledge the support and encouragements received from my wife, daughter, Mom and Dad, and my siblings that helped me in many ways to make my Master's program a success.

Financial support from the Natural Sciences and Engineering Research Council of Canada (NSERC) and a Saskatchewan Innovation and Opportunity Scholarship are acknowledged and appreciated.

Finally, to Him who is able to do far more abundantly beyond all that we ask or think, according to the power that works within us, to Him be the glory forever and ever.

DEDICATION

This dissertation is dedicated to my wife, Deborah Ogunremi, and daughter, Precious Ogunremi. I love you both.

TABLE OF CONTENTS

NOMENCLATURE

English Symbols

AR	aspect ratio of the finite square prism
C_D	mean drag force coefficient
C_{D0}	mean drag force coefficient for the case of no splitter plate
D	width of the prism [mm], diameter of the cylinder [mm]
f	vortex shedding frequency [Hz]
F_D	mean drag force [N]
F_L	mean lift force [N]
G	gap between the rear of the prism and the leading edge of the splitter plate [mm]
H	height of the prism or boundary layer shape factor [mm]
H_{sp}	height of the splitter plate [mm]
L	length of the splitter plate [mm]
P_∞	freestream static pressure [kPa]
q_∞	freestream dynamic pressure [Pa]
R	gas constant for air [J/(kgK)]
Re	Reynolds number based on the width of the prism
Re_x	Reynolds number based on the distance from the leading edge of the ground plane
Re_θ	Reynolds number based on boundary layer momentum thickness
St	Strouhal number
St_0	Strouhal number for the case of no splitter plate
T	thickness of the splitter plate [mm]
T_∞	freestream temperature [°C]
U_∞	freestream velocity [m/s]
$\overline{U}, U$	mean streamwise velocity component [m/s]

u streamwise velocity component [m/s]

$\overline{V}$ mean cross-stream velocity component [m/s]

$\overline{W}$ mean wall-normal velocity component [m/s]

x streamwise coordinate [mm]

y cross-stream coordinate [mm]

z wall-normal coordinate [mm]

Greek Symbols

α incidence angle [^{o}]

δ boundary layer thickness [mm]

δ^* boundary layer displacement thickness [mm]

θ boundary layer momentum thickness [mm]

μ_∞ freestream dynamic viscosity [Ns/m^2]

ν_∞ freestream kinematic viscosity [m^2/s]

ρ_∞ freestream fluid density [kg/m^3]

ω_x mean streamwise vorticity component [s^{-1}]

CHAPTER ONE

INTRODUCTION

1.1 Bluff Bodies

Bluff bodies are non-streamlined objects, shapes or structures that resist the motion of a moving fluid. As a result of such resistance, bluff bodies experience very high drag forces. Examples include prisms, cubes, cones, cylinders and spheres. On the other hand, streamlined bodies are objects that offer minimal resistance to fluid flow. These bodies are designed in such a way that friction can be reduced between the object and the fluid, i.e. the flow follows the body's contours (little or no separation and a very narrow wake). Examples are aerofoils and wings. Flow around bluff bodies is complex, and depending on the range of Reynolds number, the flow field is characterized by regions of separated flow, periodic vortex shedding and a wide wake downstream of the body.

As one of the most important research topics of bluff-body aerodynamics, the flow around an "infinite" or two-dimensional square prism has been widely investigated both numerically and experimentally over the past century (Bearman and Trueman, 1972; Dutta et al., 2003; Igarashi, 1984; Lee, 1975; Lyn et al., 1995; Norberg, 1993; Obasaju, 1983; Yen and Yang, 2011). Features of this flow include flow separation from the upstream corners of the prism, the periodic, alternate formation and shedding of vortices from opposite sides of the prism, as well as a regular pattern of vortices in the wake known as the Kármán vortex street.

Many engineering applications, however, involve the flow around surface-mounted finite-height bluff bodies, such as buildings, bridges and bridge supports, and power station smokestacks. Hence, they are three-dimensional rather than two-dimensional in structure.

Figure 1.1 shows a schematic of the flow around a surface-mounted finite-height square prism of side length, D, and height, H, where x is the streamwise coordinate, y is the cross-stream coordinate, and z is the wall-normal coordinate. Here, the prism is mounted normal to a ground plane and is partially immersed in a flat-plate boundary layer, where $U(z)$ is the incoming mean flow velocity profile, U_∞ is the freestream velocity outside the boundary layer on the ground plane, and δ is the boundary layer thickness. A rectangular splitter plate of length, L, thickness, T, and height, H_{sp} is mounted in the wake of the prism. For such a body, the flow field is influenced by the flow around the free end and the flow around the prism-ground plane junction, which cause the local flow field to become strongly three-dimensional.

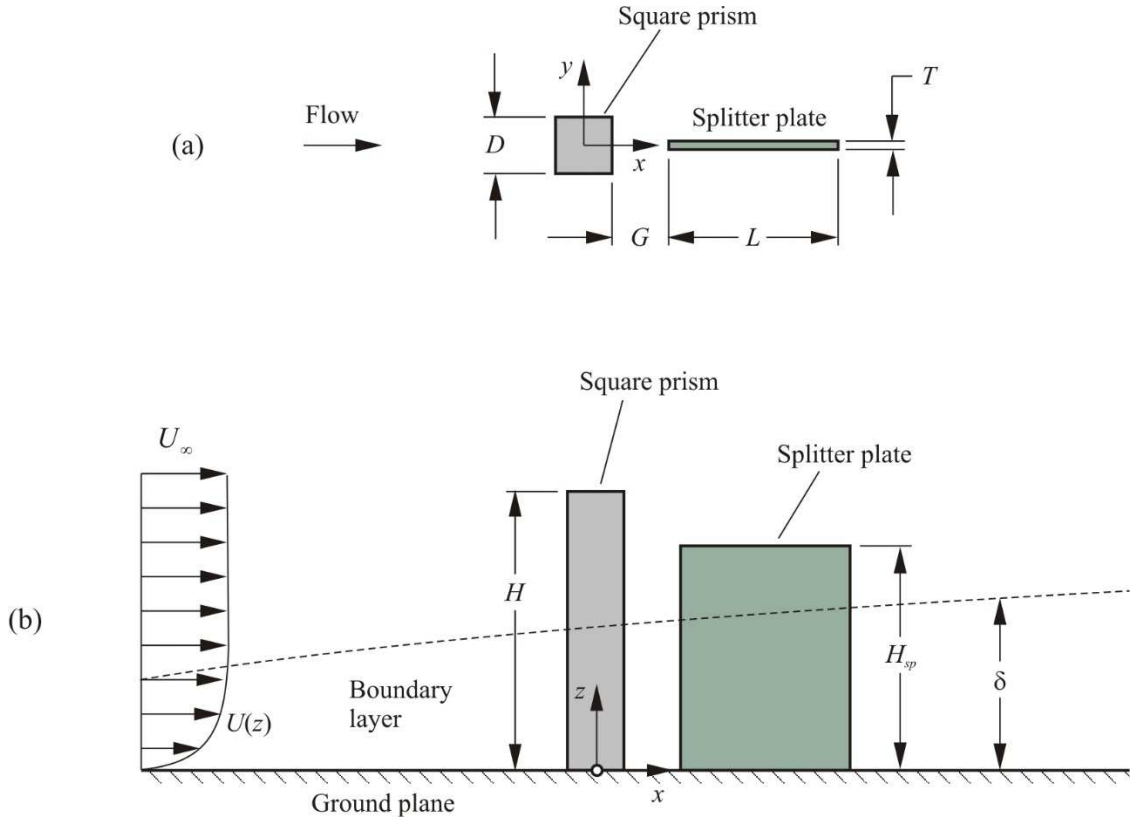

Figure 1.1: Schematic of a finite square prism mounted normal to a ground plane with a splitter plate located on the wake centreline: (a) top view (b) side view.

When a body moves through a fluid, it experiences a drag force comprised of two components, namely the frictional drag and the pressure drag. According to Smits (2000), frictional drag comes from friction between the surface of the body and the moving fluid. This type of drag is associated with boundary layer development and is sensitive to Reynolds number. On the other hand, pressure drag is related to the body's overall shape and cross-sectional area. It comes from motions that are set up in the fluid by the presence of the body. Unlike the frictional drag, pressure drag is linked to wake formation and is less sensitive to Reynolds number. Frictional drag is largely due to viscosity. While frictional drag is very important for attached flows, and is a function of the body's surface area in contact with the fluid, pressure drag is important for separated flows and is related to the body's frontal area. For the flow around a bluff body at a high Reynolds number, pressure drag is the dominant factor contributing to the total drag force. Reducing the total drag can therefore be accomplished by preventing flow separation and/or reducing the surface area in contact with the fluid. This reduction in drag is often necessary as it lowers the wind loading of structures thereby reducing failures. Also, in the automobile industry, drag reduction reduces wind resistance and fuel consumption and hence reduces the environmental impact of harmful emissions. To achieve drag reduction of bluff bodies, research has been conducted on the use of both active and passive flow control systems and devices (Akilli et al., 2005; Amitay et al., 1998; Beak and Sung, 1998; Henning and King, 2005; Igbalajobi et al., 2013; Lee and Kim, 1997; and others).

The periodic formation and shedding of vortices in an alternating way, from either side of a bluff body, can cause alternating low-pressure zones on the sides of the body, leading potentially to flow-induced vibration and noise. When the vibration frequency is close to the natural frequency of the bluff body, resonance may occur, which may lead to structural failure. To prevent or minimize this effect, different researchers have been looking

at ways to re-configure or change the wake characteristics by either weakening or suppressing vortex shedding from bluff bodies, using different flow control systems.

The use of a “splitter plate”, which is a passive means of flow control to reduce drag, suppress vortex shedding, and reduce tendency for flow-induced vibration, has been examined for two-dimensional bluff bodies (e.g., infinite cylinders and infinite square prisms). For surface-mounted finite-height bluff bodies (e.g., finite cylinders and finite square prisms), the effectiveness of a wake-mounted splitter plate has not been extensively studied, and the changes in the flow field (downstream) of such bodies are not well understood. This is the motivation for the research described in this thesis.

1.2 Objectives

The complex nature of the flow fields of three-dimensional bluff bodies, such as the finite square prism, poses significant challenges for measurement and visualization. In this thesis research project, the flow around a surface-mounted finite-height square prism, partially immersed in a flat-plate boundary layer with a splitter plate mounted on the wake centreline, is investigated experimentally. Of great interest are the combined effects of the splitter plate length and prism aspect ratio on the vortex shedding and mean drag force coefficient. Also, the mean velocity in the wake of the prism and splitter plate will be studied. The objectives of the study are the following:

- To determine whether a splitter plate is an effective drag-reduction passive flow control device for a finite square prism;
- To determine whether a splitter plate is an effective vortex-shedding-suppression passive flow control device for a finite square prism;
- To study the effect of prism aspect ratio (AR) on vortex shedding and the mean drag force coefficient;

- To study the effect of splitter plate length (L/D) on vortex shedding, the mean drag force coefficient, and the mean velocity field in the wake of the prism;
- To compare the results to those from finite and infinite cylinders, as well as infinite square prisms, with and without splitter plates.

1.3 Scope

The present study is similar to that of Igbalajobi et al. (2013), with two main differences: (i) the use of finite square prisms rather than finite circular cylinders, and (ii) making velocity measurements in the wake to study the mean flow field, so as to have a better understanding of the splitter plate effects in the wake. The experiments were conducted in a low-speed closed-return wind tunnel at the University of Saskatchewan. The test section floor consists of an already installed aluminum ground plane and a fully developed turbulent boundary layer was produced on the ground plane at the location of the finite square prism.

Four different, smooth, square prism models, all of the same width, D = 31.5 mm, were tested. The prisms have different heights, giving prisms with AR = 9, 7, 5, and 3, similar to the experiments of McClean and Sumner (2012, 2014) at the University of Saskatchewan. Each of the prisms tested was mounted to a six-component force balance located below the test section at a distance of 900 mm from the leading edge of the ground plane. Each prism extended vertically into the test section through a hole in the ground plane, and was partially immersed in the turbulent boundary layer developed on the ground plane. A relatively constant boundary layer thickness ratio of approximately $\delta/D \approx 1.5$ was used. This is similar to the earlier studies by Adaramola et al. (2006), Igbalajobi et al., (2013), McClean and Sumner (2012, 2014) and Sumner et al. (2004). Most studies of finite cylinders and prisms in the literature have had a constant boundary layer thickness, as varying the boundary layer thickness, while keeping Reynolds number constant, is experimentally

difficult. For most of the experiments, the freestream velocity, U_∞, was set at 40 m/s, giving a Reynolds number, based on prism width (D) of Re = 7.4×10^4 (same as previous study of Igbalajobi et al. (2013)). This Reynolds number was chosen to get higher and more accurate drag force, F_D, measurements, and to be able to more accurately measure the small changes in drag that occur due to the influence of the splitter plates. For the wake measurements, a lower Reynolds number of Re = 3.7×10^4 was used in order to minimize heating of the wind tunnel airflow over the course of the experiments.

For each prism, six different splitter plates were tested, with length ratios of L/D = 1, 1.5, 2, 3, 5 and 7 (L/D = 0 corresponds to the no splitter plate condition). In all cases, the height of the plate matched the height of the prism being tested, i.e., H_{sp}/H = 1. The plates were constructed from aluminum plate and had sharp edges on all sides. During the experiments, the plates were fastened in a cantilevered fashion to the ground plane immediately behind the prism. A gap of about 0.5 mm between the plate's leading edge and the prism's rear surface was ensured throughout the experiment so that the plate did not contact the prism and affect the drag force measurements. A splitter plate thickness-to-diameter ratio of T/D = 0.1 was used for the prisms of AR = 7, 5 and 3. However, for AR = 9, a thickness ratio of T/D = 0.15 was used to prevent vibration and ensure structural rigidity.

1.4 Thesis Outline

The main part of this thesis is comprised of five chapters. Chapter 2 gives a review of the background information and previous studies on the flow around infinite and finite square prisms, and the use of splitter plates. The experimental apparatus and the instrumentation used during the course of the research, as well as the physical models, are described in Chapter 3. Chapters 4 and 5 contain the results and discussion of the research work. In Chapter 4, the results obtained for the mean drag coefficient and vortex shedding

measurements behind the prism (AR = 9, 7, 5, and 3) with and without the splitter plate are presented and discussed. The results obtained for the time-averaged wake velocity field measurements behind the prism (AR = 9 and 5 only) with and without the splitter plate are presented and discussed in Chapter 5. A summary of the findings, the conclusions, and contributions and some recommendations for future work, are presented in Chapter 6.

CHAPTER TWO

LITERATURE REVIEW

2.1 Introduction

In this chapter, a brief review of the literature is presented. Section 2.2 is focussed on the flow around an infinite square prism. Flow around a finite square prism is presented in Section 2.3, while the use of splitter plates is presented in Section 2.4.

2.2 Flow around an Infinite Square Prism

A prism is considered to have an "infinite length" if the flow around it is free of "end effects." Therefore, the wake structure, velocities, and other properties do not change along the prism's span or length. The flow around an infinite square prism has been studied extensively over the years. The flow field is characterized by flow separation from the upstream corners of the prism, the periodic, alternate formation and shedding of vortices from opposite sides of the prism, as well as a regular pattern of vortices in the wake known as a Kármán vortex street (Figure 2.1). Research has shown that the fixed separation points at the upstream corners (prism set at zero incidence angle, $\alpha = 0^o$) cause the mean drag coefficient, C_D (= $F_D/(q_\infty DH)$, where F_D is the mean drag force, q_∞ is the freestream dynamic pressure, H is the prism's height and D is the prism's width) to become relatively insensitive to Reynolds number when compared to the more familiar case of an infinite circular cylinder. Mean drag coefficient measurements for infinite square prisms have been carried out experimentally by many different researchers (e.g., Bearman and Trueman, 1972; Dutta et al., 2003; Igarashi, 1984; Lee, 1975; Lyn et al., 1995; Norberg, 1993; Obasaju, 1983; Yen and Yang, 2011). Experiments have also shown that the Strouhal number, St (=fD/U_∞, where f is the vortex

shedding frequency, U_∞ is the freestream velocity and St is based on the prism's width, D) of an infinite prism is relatively insensitive to Reynolds number for Re ≈ 10^4 to 10^5 (e.g., Okajima, 1982).

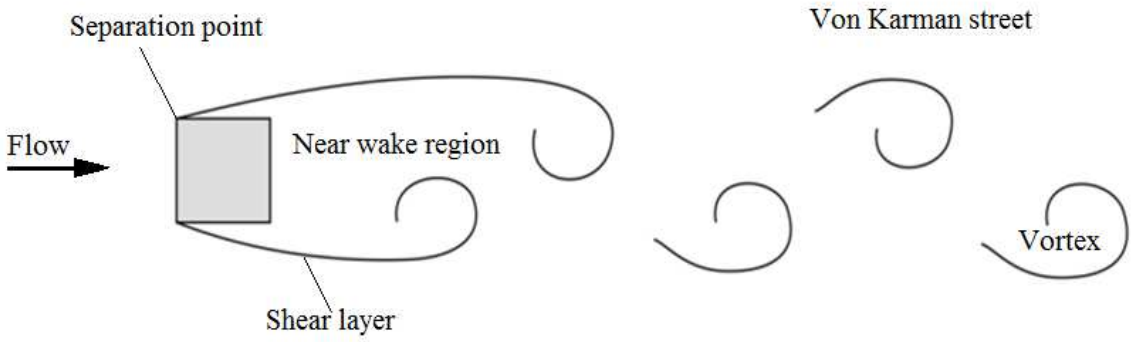

Figure 2.1: Schematic of the flow structure around an infinite square prism.

In their study, Yen and Yang (2011) identified three flow structure modes exhibited by an infinite square prism in the range of Re = 4×10^3 to 3.6×10^4 when the incidence angle, α, adjusted from 0° to 45°. These modes are the "leading-edge mode", the "separation bubble mode", and the "attached flow mode" (for Re > 2×10^4). The leading-edge separation mode, where the flow separates from the two upstream corners of the prism, occurs for $0° \leq \alpha \leq 9°$ to 11°. For 9° to $11° \leq \alpha \leq 27°$ to 30°, the separation bubble mode occurs, where a small separation bubble is formed on the prism's side just behind the leading upstream corner. Here, the flow separates from the leading corner and reattaches to the side surface after separation. The attached flow mode in which the separation bubble disappears and the flow is attached along the prism's side surface occurs for 27° to $30° \leq \alpha \leq 45°$. In addition, the mean lift force coefficient, C_L ($=F_L/(q_\infty DH)$, where F_L is the mean lift force and the lift coefficient is based on the prism width, D) was found to be insensitive to Re, the minimum C_D occurs at $\alpha = 12^o$, and the minimum (most negative) C_L occurs at $\alpha = 13^o$. The minimum and maximum Strouhal numbers occur at $\alpha = 0^o$ and $\alpha = 15^o$. Other experimental studies on the effects of

incidence angle revealed the same behavioural pattern for C_D, C_L and St (e.g., Huang et al., 2010; Igarashi, 1984; Knisely, 1990; Lee, 1975; Norberg, 1993; Obasaju, 1983).

In a second study, Yen and Yang (2012) reclassified these three modes and identified four main flow patterns, for low-turbulence flow at Re = 8×10^4. These are the "separation bubble flow pattern" for $0° < \alpha < 23°$, the "separation flow pattern" for $23° < \alpha < 34°$, the "leading-edge separation flow pattern" for $34° < \alpha < 43°$, and the "boundary-layer attached flow pattern" for $\alpha > 43°$. Figure 2.2 shows the various flow patterns with their incidence angles. Igarashi (1984) recognised four flow patterns for the infinite square prism based on the incidence angle in the range Re = 3.85×10^3 to 7.7×10^4.

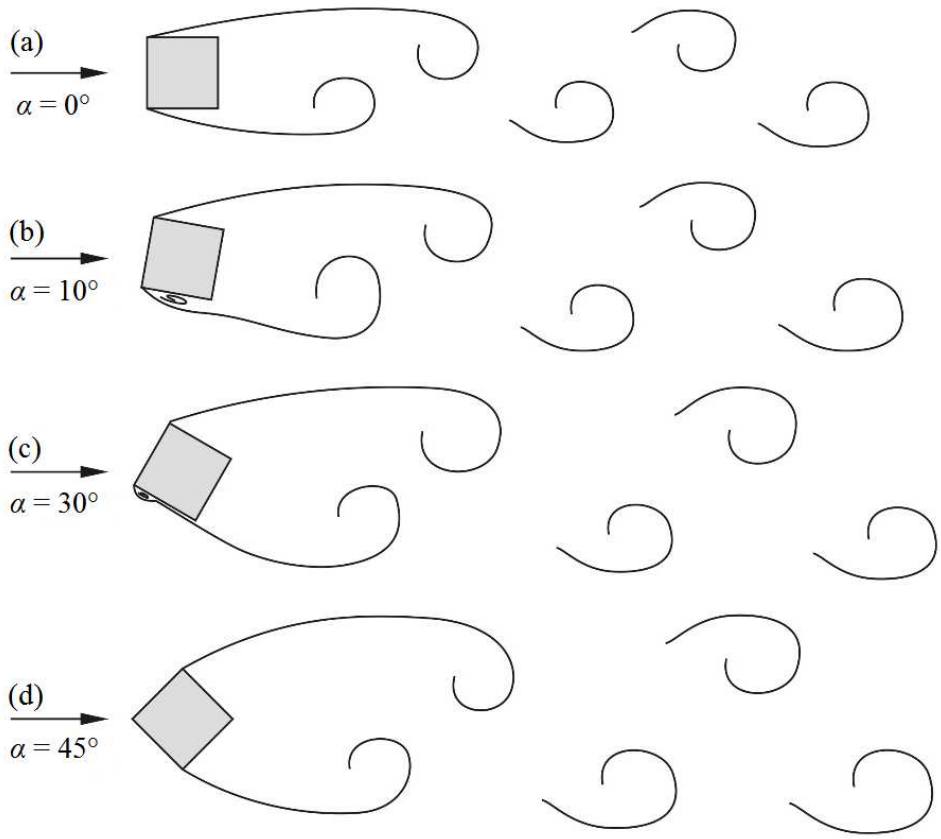

Figure 2.2: Schematics of the main flow patterns for an infinite square prism at Re ≈ 10^4 using the classification systems in the literature.

These flow patterns were designated as the “perfect separation flow pattern (symmetric)” which occurs for $0° \leq \alpha \leq 5°$, the “perfect separation flow pattern (asymmetric)”, for $5° < \alpha < 13°$, the “reattachment flow pattern”, which occurs for 14° to $15° \leq \alpha \leq 35°$, and the “wedge flow pattern” for $35^{o} \leq \alpha \leq 45^{o}$. Huang et al. (2010) classified the flow patterns as “subcritical flow”, where there is no reattachment of the separated shear layer onto the lower surface ($\alpha < \alpha_{critical}$), “supercritical flow”, where a separation bubble occurs on the lower surface ($\alpha > \alpha_{critical}$), and “wedge flow” ($\alpha = 45°$).

In the present thesis research project, it should be noted that the effects of incidence angle were not examined, and the square prisms remained aligned normal to the incident flow (at $\alpha = 0°$).

2.3 Flow around a Finite Square Prism

The flow around a finite square prism has not been widely studied when compared to the infinite prism because of its complexity. In the infinite prism case, the wake is not affected by the ends of the prism so that the wake structures and the velocity fields do not change along the prism span. For the finite square prism, the flow is more complex and is strongly three-dimensional. In addition to the flow features of an infinite prism (Section 2.2), the finite square prism has other flow features which are similar to those of a finite circular cylinder. The flow features include the Kármán vortex shedding from the sides of the prism, a pair of time-averaged counter-rotating streamwise tip vortices in the upper part of the wake, a pair of time-averaged counter-rotating streamwise base vortices near the ground plane, the horseshoe vortex at the junction between the prism and the ground plane, a downward-directed velocity, known as “downwash”, induced by the streamwise tip vortex pair, an upward-directed velocity, known as “upwash”, situated closer to the ground plane, and a

mean recirculation zone above the free end. A schematic of the finite prism flow field is shown in Figure 2.3.

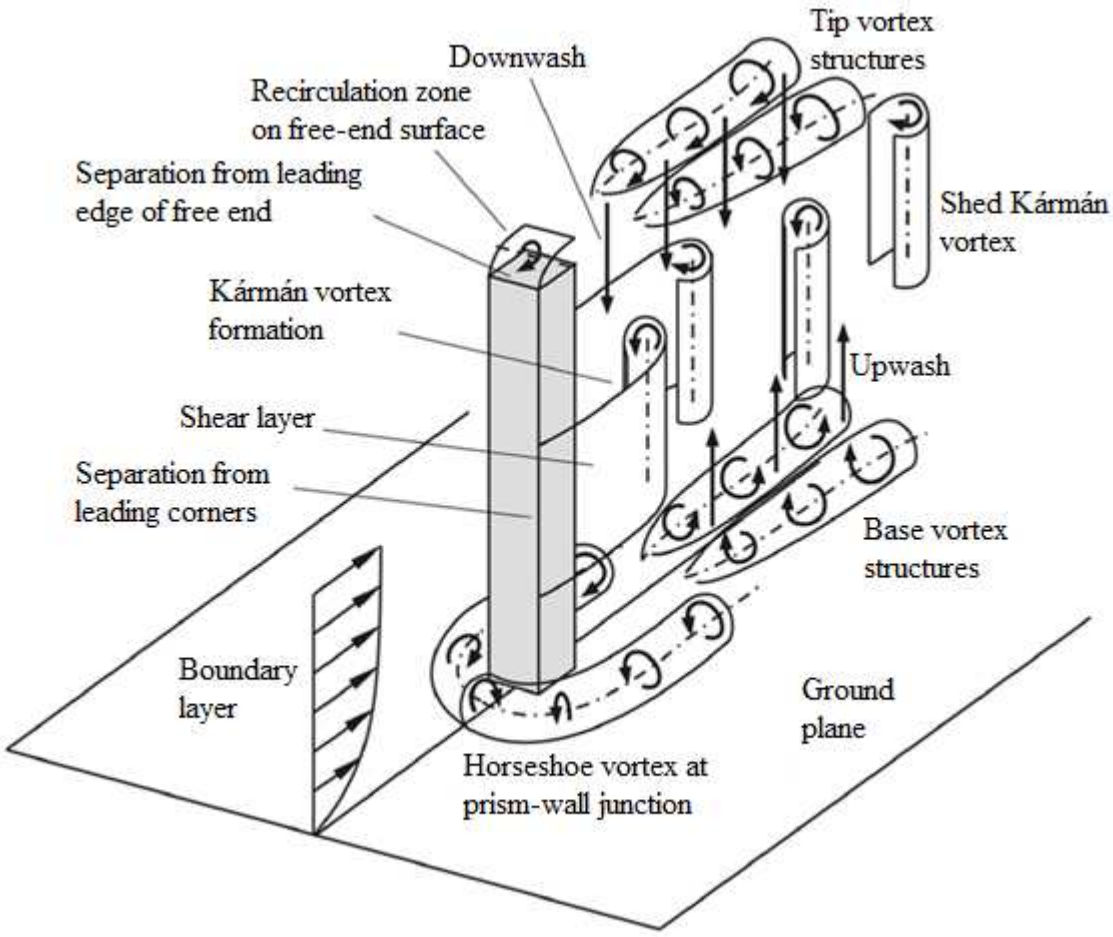

Figure 2.3: Schematic of the flow features around a finite square prism (figure produced by D. Sumner and used with permission).

The boundary layer thickness (δ/D or δ/H) as well as the prism aspect ratio (AR = H/D) are some of the parameters that influence the flow field of a finite square prism. From the literature (e.g., Adaramola et al. (2006) and Sumner et al. (2004)), finite circular cylinders of small aspect ratios (less than the "critical aspect ratio") have a wake structure different from those of higher aspect ratios. According to Kawamura et al. (1984), the critical aspect ratio is sensitive to the boundary layer thickness, and increases as δ/D or δ/H increases. For finite cylinders greater than the critical aspect ratio, the flow pattern is characterized by the presence of the anti-symmetric Kármán vortex shedding, whereas, for cylinders less than the

critical aspect ratio, the wake structure is often described as symmetric "arch vortex shedding". In their studies, Adaramola et al. (2006) and Sumner et al. (2004) suggested that the critical aspect ratio of a finite circular cylinder lies between AR = 5 and AR = 3, where the experimental conditions were similar to the present thesis research project. For a finite square prism, McClean and Sumner (2012, 2014) also suggested that the critical aspect ratio is between AR = 5 and AR = 3, again using similar experimental conditions; however, the results of Rostamy et al. (2012), also under similar conditions, suggested that the prism of AR = 5 might be below the critical aspect ratio instead.

Wang et al. (2004) carried out an experiment to investigate the flow around finite-height square prisms of AR = 7 to AR = 3 at Re = 9.3×10^3. The flow was measured using hot-wire anemometry and particle image velocimetry (PIV) techniques. They found that at AR = 3, spanwise vortex shedding is largely suppressed and the near wake is dominated by the tip and the base vortices. At AR = 5 and 7, periodic spanwise vortex shedding occurs over almost the whole height except very close to the ground plane. It was also observed that as the tip vortex grows, the base vortex decays and the higher the AR, the longer the recirculation region.

Sarioglu and Yavuz (2000) experimentally studied vortex shedding from finite rectangular cross-section prisms in a wind tunnel. Measurements were taken at Re = 1×10^4 to 2×10^5 with three rectangular models with width-to-height ratios (D/H) of 0.5, 1.0 and 2.0. From their measurements, they found that the Strouhal numbers decreased with increasing width-to-height ratios.

Sarode et al. (1981) measured the mean aerodynamic force coefficients for surface-mounted finite-height square prisms of AR = 1.14 to 10 at Re = 2.2×10^4. The prisms were immersed in an atmospheric boundary layer. They found that the incidence angle effects on C_D were significant for the more slender prisms of AR = 6.36 and 10, while for the smaller

aspect ratios of AR = 1.14, 2.27, and 3.64, the incidence angle effects on C_D were much less significant. They also found that as the aspect ratio decreases, the mean lift coefficient reduced in magnitude.

McClean and Sumner (2012, 2014) investigated the effects of aspect ratio and incidence angle on the aerodynamic forces and vortex shedding for a surface-mounted finite square prism. Their experiments were conducted at a Reynolds number of 7.2×10^4 for AR = 11, 9, 7, 5, and 3; the incidence angle was varied from α = 0° to 45°. They found that the mean drag coefficient, C_D, mean lift coefficient, C_L, and Strouhal number, St, of the finite square prism are very sensitive to α. This is similar to what was observed for infinite square prisms. However, the variation of C_D and St with α is less evident than for the infinite square prism. For all aspect ratios tested, they observed that the critical incidence angle associated with the minimum C_D, the maximum C_L (magnitude), and the maximum St, occurred at α_{critical} = 15° to 18°, which was higher than the typical range of critical incidence angles for infinite square prisms.

Many of these studies have focused on the effects of aspect ratio and incidence angle on the flow around finite square prisms. In the present study, the combined effects of aspect ratio and splitter plate length for four finite square prisms of AR = 9, 7, 5, and 3 are investigated.

2.4 Splitter Plates

Both active and passive bluff body flow control mechanisms have been investigated for many decades and applied in experiments. Overviews of active and passive flow control techniques are given by Gad-el-Hak (2000), Zdravkovich (1981) and Choi et al. (2008). Active control techniques control vortex shedding or reduce drag through adding or removing momentum or energy. Passive bluff body flow control techniques do not require any external

energy. Examples of passive flow control systems are helical wires, small secondary control cylinders, and splitter plates.

According to Zdravkovich (1981), the high drag forces and vortex shedding experienced by bluff bodies have led to the use of passive flow control devices in an attempt to change the characteristics of the wake, and thereby reduce the drag and weaken or suppress vortex shedding. One such passive flow control device is the "splitter plate", which is a thin, flat, two-dimensional plate usually mounted behind a bluff body parallel to the flow on the wake centreline.

The use of splitter plates to control the flow around an infinite cylinder (of diameter D) has been extensively studied experimentally (Akilli et al., 2005; Anderson and Szewczyk, 1997; Apelt et al., 1973; Apelt and West, 1975; Gerrard, 1966; Nakamura, 1996; Unal and Rockwell, 1987; and others) and numerically (Dehkordi and Jafari, 2010; Hwang et al., 2003; Kwon and Choi, 1996; and others). The effectiveness of the splitter plate for vortex shedding suppression and drag reduction depends largely on flow parameters, such as the Reynolds number, Re, and geometrical parameters, such as the plate's length, L/D, and thickness, T/D (Akilli et al., 2005; Anderson and Szewczyk, 1997; Apelt et al., 1973; Apelt and West, 1975; Nakamura, 1996; Unal and Rockwell, 1987).

For an infinite cylinder with a wake-mounted splitter plate, the mean drag coefficient decreases with an increase in the splitter plate length. Studies show that the drag coefficient has a local minimum between L/D = 1 to 1.5 and a local maximum near L/D = 2. After additional reduction in C_D for $2 < L/D < 4.5$, the drag coefficient then becomes insensitive to further changes in L/D (Apelt et al., 1973, Apelt and West, 1975).

The Strouhal number behaviour with L/D is also nonlinear, similar to the C_D behaviour, with a tendency to a reduction in St with increasing L/D until vortex shedding becomes suppressed (Anderson and Szewczyk, 1997; Apelt et al., 1973; Apelt and West,

1975; Gerrard, 1966). For splitter plates with $L/D < 2$, the St behaviour is complex and may be higher or lower than the value for an isolated cylinder. Splitter plates of $L/D > 2$ result in reduction of the Strouhal number below the isolated-cylinder value, with suppression of vortex shedding for $L/D > 4$. At $L/D = 1$, both a local minimum value of St and a local minimum of C_D coincide (Apelt et al., 1973, Apelt and West, 1975), and suppression of vortex shedding happens at the point where C_D becomes insensitive to additional increases in plate length (for $L/D > 4.5$).

For the case of the surface-mounted finite-height circular cylinder (Adaramola et al., 2006, Igbalajobi et al., 2013, Sumner et al., 2004), additional parameters that can potentially affect the splitter plate's effectiveness include AR, δ/H or δ/D, and the relative height of the splitter plate, H_{sp}/H.

In one of the few studies of splitter plates that looked at a finite-height bluff body, Igbalajobi et al. (2013) studied experimentally the effect of a wake-mounted splitter plate on the flow around a finite cylinder at $Re = 7.4\times10^4$ for cylinder aspect ratios of AR = 9, 7, 5, and 3. In their study, $\delta/D = 1.5$ and L/D ranged from 1 to 7. For drag reduction, they found that the splitter plate is less effective for a finite cylinder compared to an infinite cylinder (the maximum reduction in C_D was 12% for AR = 9, compared to 32% for an infinite cylinder with a splitter plate of $L/D = 7$ (Apelt and West, 1975)). Meaningful reduction in the mean drag coefficient occurred only for AR = 9 with splitter plates of $L/D = 1$ to 3; unusually, lengthening the splitter plate further led to C_D increasing and returning to the value obtained for the isolated cylinder. For suppressing vortex shedding, depending on AR, the splitter plate seemed to be more effective for a finite cylinder than for an infinite cylinder: a finite cylinder of AR = 9 needed splitter plates of $L/D \geq 5$ for vortex shedding suppression, similar to the infinite cylinder case; however, for AR = 3, vortex shedding suppression occurred for $L/D \geq 1$, and for AR = 7 and 5 it occurred for $L/D \geq 1.5$ (Igbalajobi et al., 2013).

Flow around infinite square prisms with splitter plates has not been extensively studied or investigated like the case of the infinite cylinder. Ali et al. (2011) carried out a numerical simulation of the flow around a square prism with a splitter plate at Re = 150, for L/D = 0.5 to L/D = 6. Three regimes were identified: for short plate lengths ($0 \leq L/D \leq 1$), the shear layers extend further downstream before rolling up; for intermediate plate lengths ($1.25 \leq L/D \leq 4.75$), the shear layers began to roll-up closer to the trailing edge of the plate, where a "secondary vortex" formed; for long plate lengths ($L/D \geq 5$), the shear layers from the prism reattach onto the splitter plate surface. A splitter plate of length L/D = 6 was able to reduce the mean drag coefficient by 21%. Like the infinite cylinder, the effect of the splitter plate on the Strouhal number was found to be nonlinear. Very short splitter plates ($L/D \leq 1.25$) tended to reduce the Strouhal number. An increase in Strouhal number then occurred for short splitter plates from $1.5 \leq L/D \leq 2$. For $3 \leq L/D \leq 6$, St tended to decrease once again.

Hasan and Budair (1994) investigated the effect of a splitter plate as well as the gap, G, between the trailing edge of a square prism and the leading edge of the splitter plate over a range of Re = 1.2×10^4 to 2.4×10^4. For gaps of $G/D \leq 3$, the Strouhal number was lowered compared to the case of no splitter plate, while for $G/D > 3$ it increased and returned to the no splitter plate condition.

Mansingh and Oosthuizen (1990) investigated the effect of splitter plates on the wake flow behind a rectangular prism over a range of Re = 0.35×10^3 to 1.15×10^3. Splitter plate lengths of L/D = 1, 2 and 3 were used. Their results were consistent with those of circular cylinders, indicating that splitter plates alter the vortex formation behaviour in the wake, which leads to a reduction in the Strouhal number and a lowering of the drag coefficient by up to 50%.

For the surface-mounted finite-height square prism, the combined effects of aspect ratio, Reynolds number and splitter plate length on the mean drag coefficient, vortex shedding, and wake structure, have not been extensively studied, and this is the motivation for this M.Sc. thesis research project.

CHAPTER THREE

EXPERIMENTAL APPARATUS AND INSTRUMENTATION

3.1 Introduction

This chapter describes the experimental apparatus and instrumentation used for this study. Section 3.2 presents detailed information about the wind tunnel. The square prism models and splitter plates used in the study are described in Section 3.3. A description of the instrumentation is given in Section 3.4, and the boundary layer measurements above the wind tunnel's ground plane are described in Section 3.5. Measurement uncertainty is briefly summarized in Section 3.6.

3.2 Wind Tunnel

All experiments were carried out in a low-speed, closed-return wind tunnel located in the Department of Mechanical Engineering, University of Saskatchewan (Figure 3.1). A 75-kW variable-pitch fan drives the airflow inside the tunnel. This fan can produce freestream velocities up to U_∞ = 50 m/s within the test section. The airflow generated by the fan passes through the return passage where it expands through two sets of turning vanes located at the top and bottom corners of the tunnel. The vanes redirect the airflow through 180°. At the exit of the turning vanes are located screens which reduce the turbulence intensity of the airflow. The flow then passes through the low-speed test section (settling chamber of dimensions 2.97 m (height) × 2.4 m (width) × 7.0 m (length)) and enters the high-speed test section through a 7:1 contraction section. The high-speed test section (Figure 3.2) is where the experimental apparatus (square prism models, splitter plates, probes, three-axis

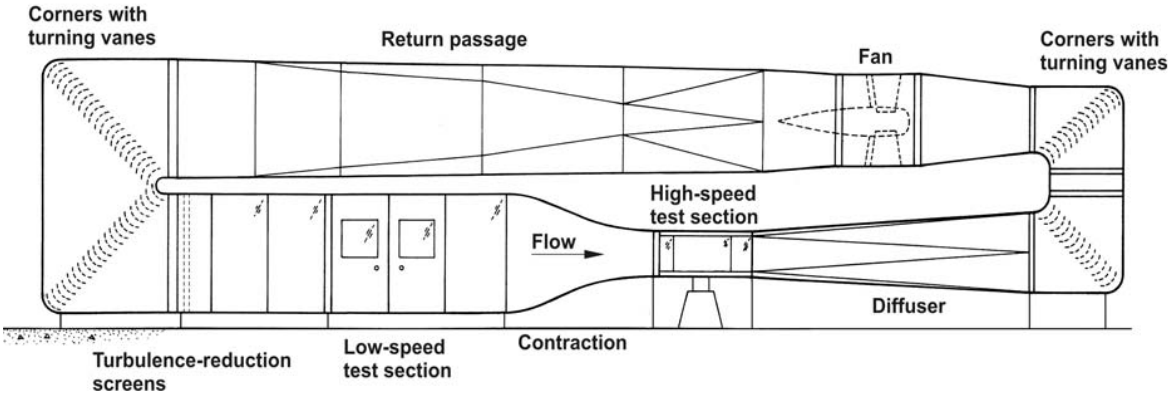

Figure 3.1: Schematic diagram of the University of Saskatchewan's low-speed wind tunnel. (Figure reproduced here with the permission of D. Sumner.)

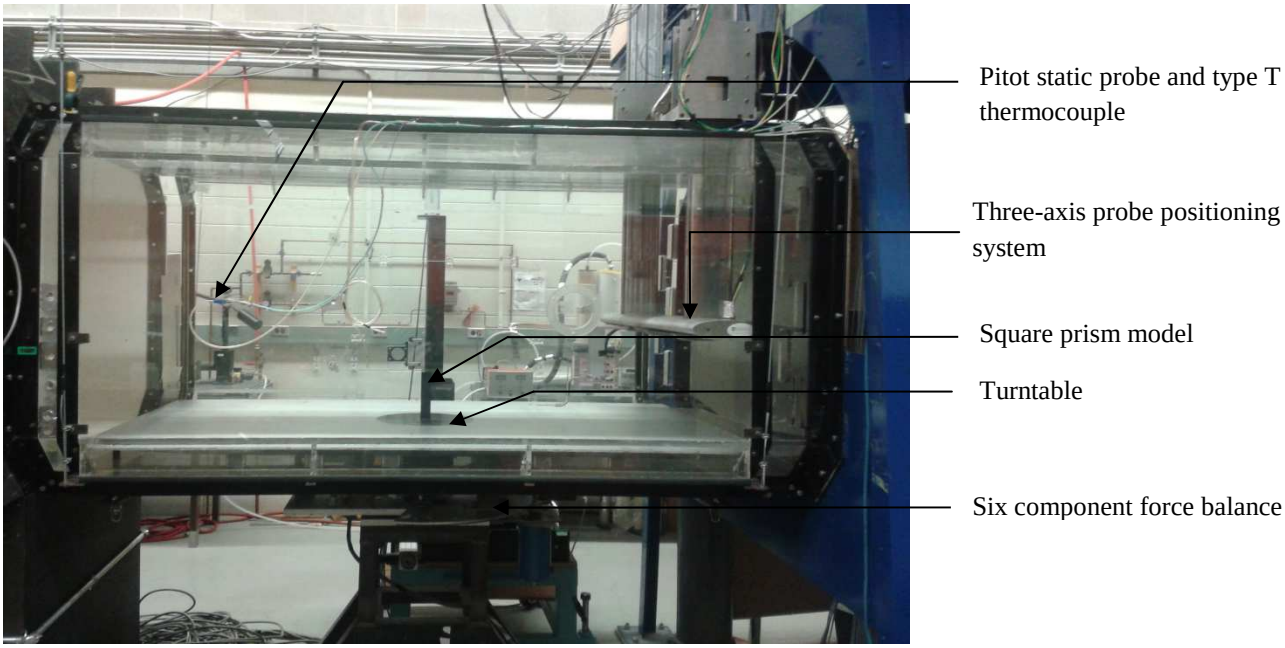

Figure 3.2: Wind tunnel test section. Flow is from left to right.

probe positioning system, etc.) are installed. The test section has dimensions of 0.91 m (height) × 1.13 m (width) × 1.96 m (length). The streamwise freestream turbulence intensity in this test section is less than 0.6% and the mean velocity non-uniformity outside the test section wall boundary layers is less than 0.5%. The section's sidewalls are made of Plexiglas thereby aiding the visualization of the experimental apparatus. This section is fitted with a

computer controlled turntable (modified to include holes used to firmly hold the splitter plates in place) for mounting the test models. In the present experiments, the turntable was not rotated, but remained in a fixed position with the prism oriented normal to the flow at α = 0°. A fully developed turbulent flat-plate boundary layer is produced on the ground plane at the location of the test models. The prisms and splitter plates were mounted normal to this ground plane and were partially immersed in this boundary layer. After passing through the high-speed test section, the airflow enters the diffuser and returns to the fan and recirculates again.

3.3 Experimental Models

Four different, smooth, square prisms, all of the same width, D = 31.5 mm, were used throughout the experiments. The square prisms had sharp edges on all sides. Each prism had a different height, resulting in prisms of aspect ratios of AR = 9, 7, 5, and 3 (Figure 3.3). Similar to the experiments of Adaramola et al. (2006), Igbalajobi et al. (2013), Sumner et al. (2004), and McClean and Sumner (2012, 2014), each prism was mounted to a six-component force balance positioned below and outside the test section, see Figure 3.2, at a distance of 900 mm from the leading edge of the ground plane. The prisms extended into the test section through a hole in the turntable with a gap of about 1 mm around the prisms and were partially immersed in the turbulent boundary layer of the ground plane. The gap is to prevent direct contact between the prisms and the ground plane which will affect the drag force measurements. At this location and at U_∞ = 40 m/s, the boundary layer thickness was δ = 47 mm, which corresponded to δ/D = 1.5 and δ/H ranging from δ/H = 0.2 (for AR = 9) to δ/H = 0.5 (for AR = 3). The solid blockage ratio (the ratio of the frontal area of the prism to the cross-sectional area of the test section) ranged from 0.9% (for AR = 9) to 0.3% (for AR = 3) and no wall interference corrections were made.

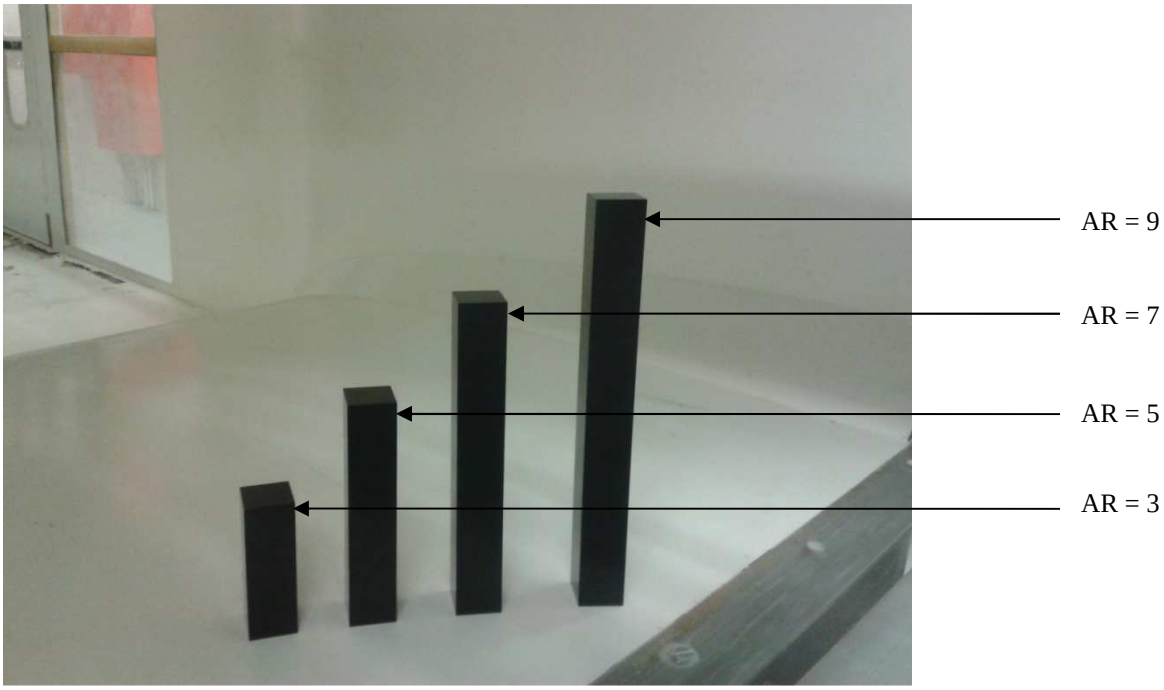

Figure 3.3: Finite-height square prism models.

For investigating the effects of a splitter plate on the flow around the square prisms, six different splitter plates were tested, with length ratios of L/D = 1, 1.5, 2, 3, 5 or 7. The plates were made from aluminum (AR ≤ 5) and steel (AR ≥ 7) with sharp edges on all sides. Figure 3.4 shows a splitter plate mounted along the wake centreline to the ground plane immediately behind the prism. A gap of 0.5 mm existed between the rear surface of the prism and the leading edge of the plate to prevent direct contact between the plate and prism which would affect the drag force measurement. This gap corresponds to a ratio of G/D = 0.016; according to Cardell (1993), gaps of G/D < 0.13 should have no effect on the mean base pressure and vortex shedding frequency. In all cases, the prisms and plates were of the same height, i.e. H_{sp}/H = 1. The thickness ratio of the splitter plates was T/D = 0.1 for the prisms of AR = 3, 5 and 7. For AR = 9, a thicker splitter plate of T/D = 0.15 was used to prevent vibration.

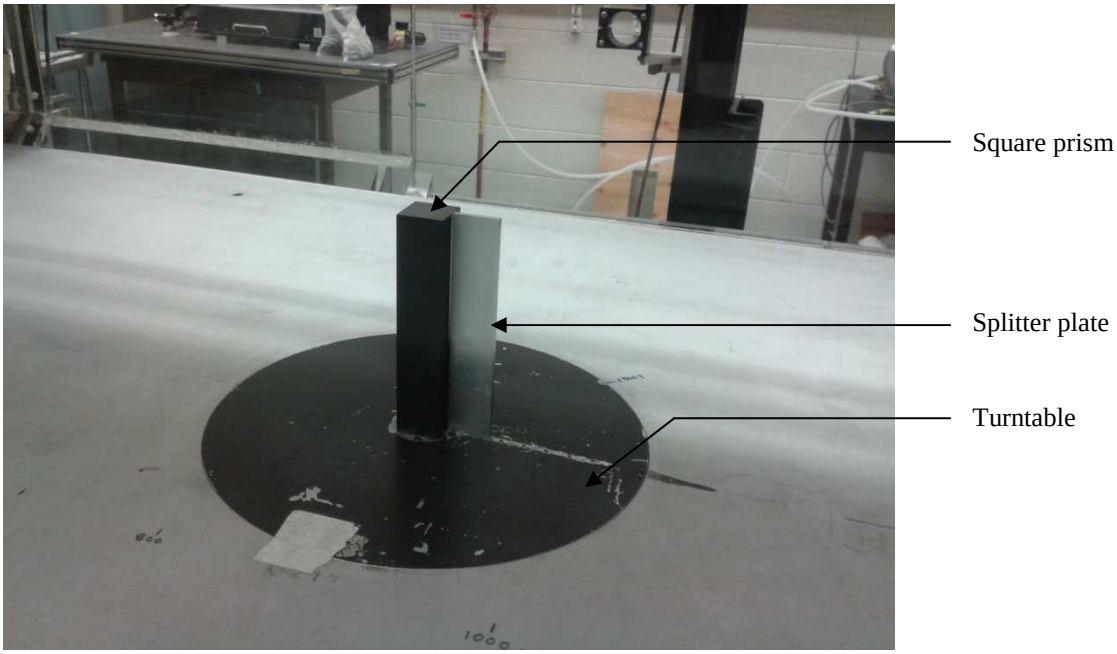

Figure 3.4: Finite-height square prism of AR = 5 and splitter plate of L/D = 1.5. Note that flow is from left to right.

3.4 Instrumentation

The wind tunnel data were acquired using a computer with a 1.8-GHz Intel Pentium 4 processor, a National Instruments PCIe-6259 16-bit data acquisition board and LabVIEW software. Figure 3.5 shows some of the details of the data acquisition and wind tunnel control systems. The freestream conditions were obtained with a Pitot-static probe (United Sensor, 3.2-mm diameter) and Datametrics Barocel absolute and differential pressure transducers (described below). The Pitot-static probe was mounted on the side wall of the test section (see Figure 3.2) at about 400 mm from the contraction exit, 340 mm above the ground plane and 190 mm into the test section. With this, the effect of wall proximity is eliminated, hence no wall-proximity correction factor was used. The probe measures the total and static pressures at the same point in the flow and is equipped with a built-in thermocouple (type T) for measuring total temperature as well. Such a dual capability permits immediate calculation of flow velocity, density, viscosity and other related properties of the moving air flow. This type

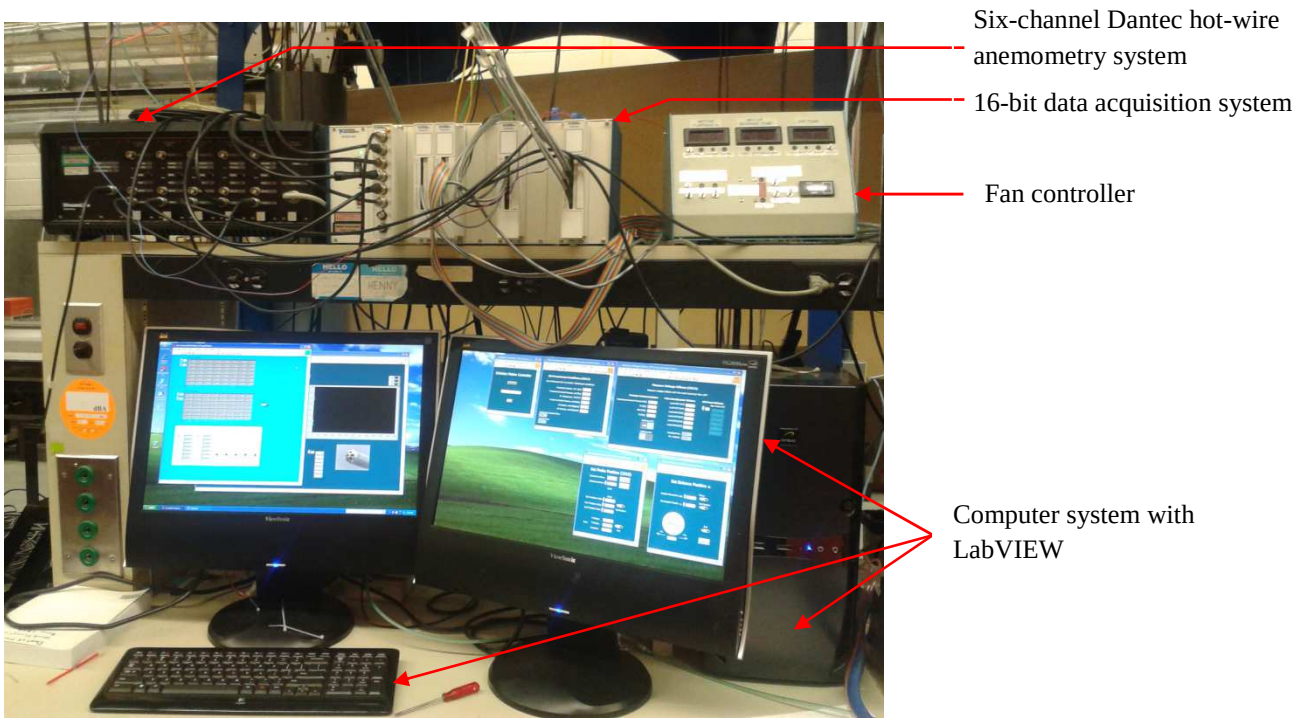

Figure 3.5: Data acquisition system and wind tunnel control system.

of probe is insensitive to turbulence errors and is not affected by Reynolds number except at very low velocities (Bryer and Pankhurst, 1971).

The density of the air (ρ_∞) was calculated using the ideal gas equation,

$$\rho_\infty = \frac{P_\infty}{RT_\infty}, \tag{3.1}$$

where R is the gas constant for air (287 J/(kgK)), T_∞(K) is the freestream temperature, and P_∞ (Pa) is the absolute freestream static pressure. The kinematic viscosity of the air, v_∞, is calculated using the Sutherland correlation as given below (White, 2003):

$$v_\infty = 1.453 \times 10^{-6} \frac{T_\infty^{1.5}}{\rho_\infty (T_\infty + 110.4)}. \tag{3.2}$$

The dynamic viscosity of the air, μ_∞, is calculated by multiplying the kinematic viscosity by its density, i.e.,

$$\mu_\infty = v_\infty \rho_\infty. \tag{3.3}$$

A pressure transducer converts the pressure (as measured by the probes) into a DC output voltage proportional to the input pressure. The pressures and temperatures are sampled

at 1 kHz for 10 s (averaging time). Four different pressure transducers, namely a Datametrics Barocel absolute pressure transducer (Model 600A-1000T-513-H21X-4), a Datametrics Barocel differential pressure transducer (Model 590D-10W-2QB-VIX-4D), a BOC Edwards differential pressure transducer (Model 590DF) and a Validyne Model P55D differential pressure transducer were used for this study. The Datametrics Barocel absolute pressure transducer was used to measure the absolute freestream static pressure, P_∞, and the Datametrics Barocel differential pressure transducer was used to measure the freestream dynamic pressure, q_∞. The BOC Edwards differential pressure transducer was used to measure the reference pressure for calibration of the seven-hole pressure probe (described below). The Validyne P55D differential pressure transducer was connected to a United Sensor boundary layer Pitot tube, which was used to measure the boundary layer's mean velocity profile.

Measurements of the prism's mean drag force were made using an external six-component force balance, a multiple-axis force transducer (Figure 3.2) with interacting load cells which are used to determine the three forces (drag, lift and side forces) and the three moments (rolling, pitching and yawing moments) that act on models during testing. The output from the load cells is measured as a voltage signal which is proportional to the applied load (force). The drag force measurements were made at U_∞ = 40 m/s, which corresponded to Re = 7.4×10^4. Like the pressures and temperatures, the forces were sampled at 1 kHz for 10 s.

Vortex shedding frequency measurements were made with a six-channel Dantec Dynamics Streamline constant temperature hot-wire anemometry system (Figure 3.5) and a Dantec 55P11 single wire probe. The hot-wire probe was not calibrated since it was only used to find the power spectrum of the streamwise velocity fluctuations. The output (anemometer) was connected to the data acquisition system. The probe was positioned at 4.5D downstream of the trailing edge of the prism-plate combination (in the wake of the combined body) at x/D

= L/D + 5 (where x/D is in the streamwise direction measured from the centre of the prism), at a fixed cross-stream position of y/D = 2 and allowed to vary along the height of the prism-plate combination from z/D = 0.5 (close to the ground plane) to 0.5D below the free end of the prism (i.e., until z/D = 2.5 to 8.5 for AR = 3 to 9, respectively), with a 0.5D increment. The probe location was chosen to ensure that the measurements were taken outside the recirculation zone and within the wake width to ensure that strong vortex shedding peaks would appear in the power spectra. Similar hot-wire probe positioning was used by Igbalajobi et al. (2013) for the finite-cylinder splitter plate experiments. The vortex shedding experiments were conducted at a Reynolds number of Re = 7.4×10^4 (corresponding to a freestream velocity of U_∞ = 40 m/s).

Measurements of the time-averaged wake velocity field behind the prism with and without the splitter plate were made with a seven-hole pressure probe. Similar measurements were made by Sumner et al. (2004) and Adaramola et al. (2010) using the same probe and similar instrumentation. The seven-hole probe (Figure 3.6) is a non-nulling, directional velocity probe used to measure the local time-averaged velocity vector. The seven-hole pressure probe used in the present study was manufactured by Engineering Shops at the University of Saskatchewan. The probe is conical in shape with a cone angle of 30° and 3.45 mm in diameter. It is comprised of seven, close-packed 1-mm diameter stainless steel tubes (one inner hole or port surrounded by six outer holes or ports), fitted into an outer stainless steel sleeve (Figure 3.6(a)).

The probe can be used to measure three velocity components of the flow at flow angles up to 80° from the probe axis. Calibration of a seven-hole probe requires subjecting the probe to flows of a known direction (Sumner, 2002). The two calibration data-reduction methods commonly employed for seven-hole probes are the polynomial curve-fit method

developed by Gallington (1980) and the direct-interpolation method of Zilliac (1993). The results presented in this thesis were calculated using the direct-interpolation method of Zilliac

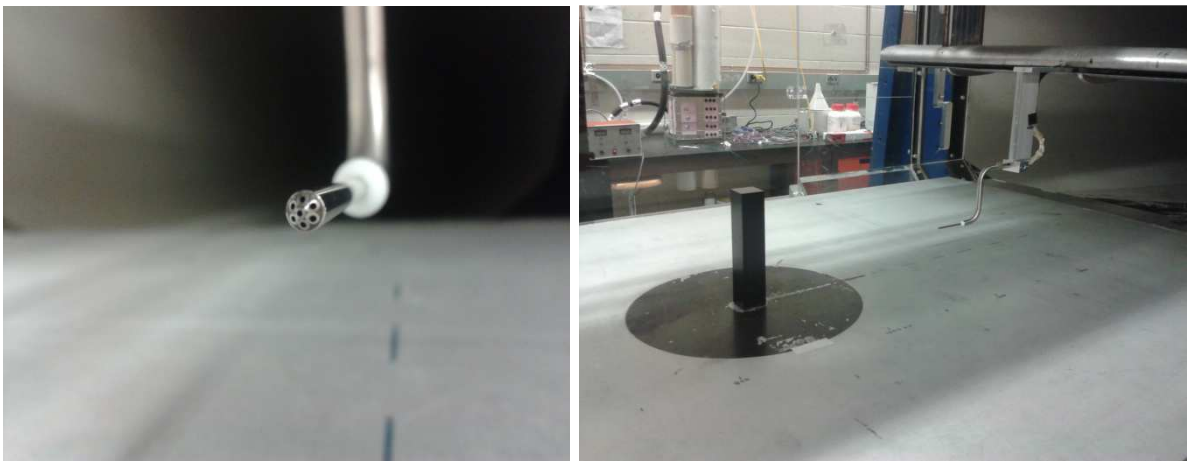

(a) (b)

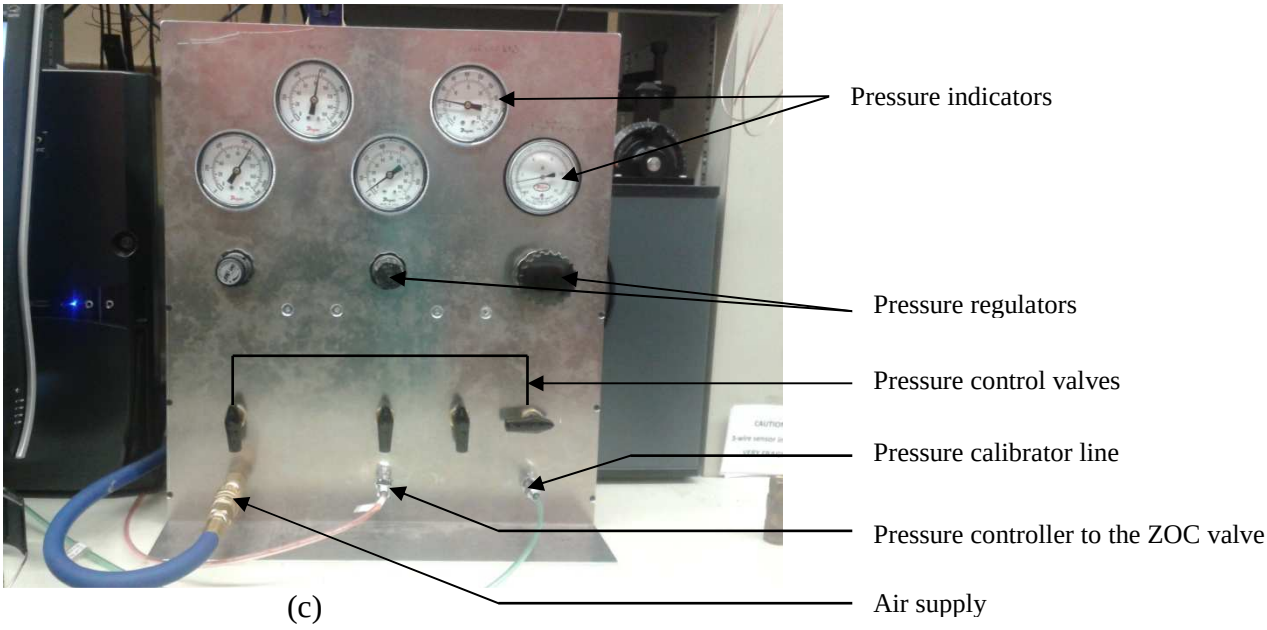

(c)

Figure 3.6: The seven-hole pressure probe; (a) the seven pressure holes, (b) position in the wind tunnel (flow is from left to right), (c) pressure control panel.

since it proved to be slightly more accurate than the polynomial curve-fit method (Sumner, 2002). Experiments with the probe were conducted at a Reynolds number of Re = 3.7×10^4 corresponding to a freestream velocity of U_∞ = 20 m/s. The probe was positioned downstream (Figure 3.6(b)) at x/D = 10 (streamwise), was allowed to vary from y/D = −3 to

+3 (cross-stream) and *z* ranged from approximately *D*/3 (close to the ground plane) to 1*D* above the prism free end in the wall-normal direction with approximately *D*/6 increments in both the *y* and *z* directions. Figure 3.6(c) shows the pressure control panel for the seven-hole probe.

The seven-hole probe measures seven pressures at each location with a Scanivalve ZOC-17 pressure scanner. The Scanivalve ZOC (Zero, Operate, Calibrate) electronic pressure scanner makes use of individual pressure sensors for each pressure input. A calibration valve allows the ZOC pressure sensors to be automatically calibrated "online", i.e., when measurements are being taken. The BOC Edwards differential pressure transducer provides an accurate reference pressure for online calibration checks of the ZOC's eight pressure transducers. For this experiment, calibration was done at every 200 mm of vertical travel of the probe. For this study, one ZOC with eight pressure input channels (ZOC-17IP/8Px) was used (Figure 3.7).

Figure 3.7: Scanivalve ZOC pressure scanner used for the seven-hole probe measurements.

3.5 Boundary Layer Measurement

Measurements of the boundary layer velocity profiles and properties were made using a United Sensor boundary layer Pitot tube and a Validyne P55D differential pressure

transducer at a freestream velocity of U_∞ = 40 m/s. The probe was positioned at three different streamwise positions corresponding to x/D = 0, 5 and 10 (where x/D = 0 corresponds to the centre of the prism). Table 3.1 shows a summary of the boundary layer measurements on the ground plane. In this table, x/D = 0 (900 mm from the ground plane leading edge) is the location of the models, however the models were removed during the boundary layer measurements. The boundary layer thickness, δ, was obtained at the location where the streamwise mean velocity component is 99% of the freestream velocity i.e., $u = 0.99U_\infty$, for each of the streamwise probe positions.

The mean velocity profiles are presented in Figure 3.8. The boundary layer profiles all nearly collapsed onto a common curve suggesting that the boundary layer was fully developed.

The boundary layer data for the seven-hole probe experiments made at U_∞ = 20 m/s are presented in Table 3.2 (these data are from Rostamy (2012)).

Table 3.1: Summary of boundary layer measurements on the ground plane for the finite prism experiments, U_∞ = 40 m/s.

Location, x/D	Boundary layer thickness, δ (mm)	Displacement thickness, δ^* (mm)	Momentum thickness, θ (mm)	Shape factor, $H = \delta^*/\theta$	Reynolds number based on x, Re_x	Reynolds number based on θ, Re_θ	δ/D
0	47	3.8	3.3	1.1	2.1E+06	7.9E+03	1.5
5	49	5.3	4.3	1.2	2.5E+06	1.0E+04	1.6
10	51	5.2	4.3	1.2	2.8E+06	1.0E+04	1.6

Table 3.2: Summary of boundary layer measurements on the ground plane for the finite prism experiments, U_∞ = 20 m/s (data are from Rostamy (2012)).

Location, x/D	Boundary layer thickness, δ (mm)	Displacement thickness, δ^* (mm)	Momentum thickness, θ (mm)	Shape factor, $H = \delta^*/\theta$	Reynolds number based on x, Re_x	Reynolds number based on θ, Re_θ	δ/D
0	51	5.7	4.6	1.3	1.2E+06	5.9E+03	1.6
5	54	6.1	4.9	1.2	1.4E+06	6.6E+03	1.7
10	56	6.3	5.0	1.2	1.6E+06	6.8E+03	1.8

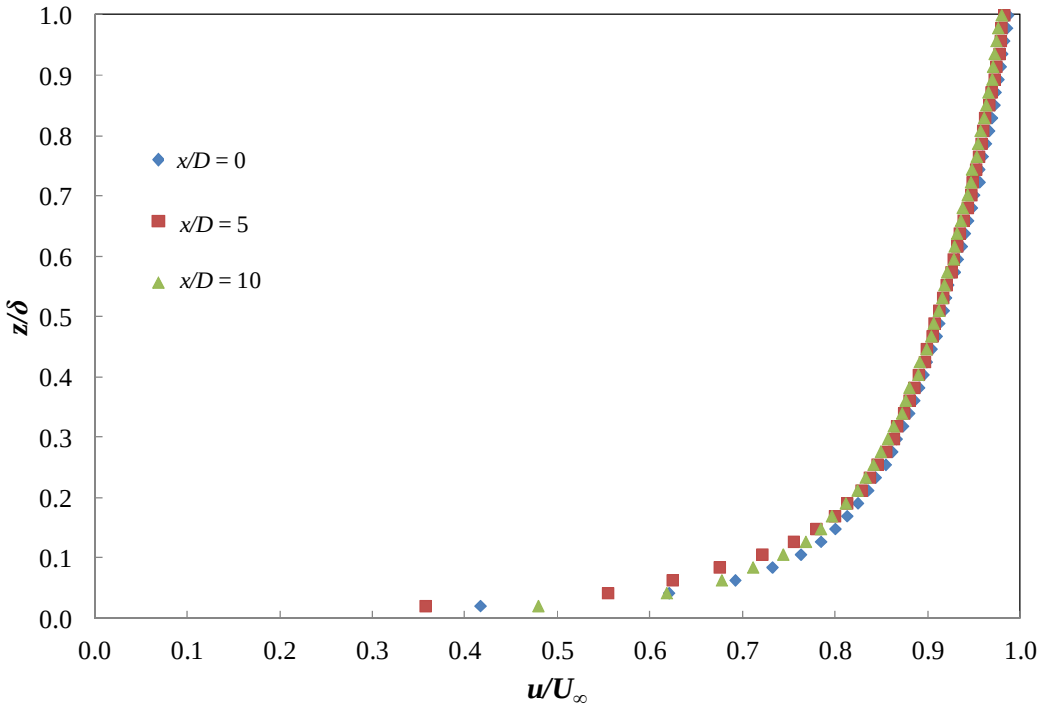

Figure 3.8: The ground plane boundary layer mean velocity profiles at three different locations at a freestream velocity of U_∞ = 40 m/s: x/D = 0, x/D = 5, and x/D = 10, where x = 0 corresponds to the location of the prism.

3.6 Uncertainty Estimate

Since the instrumentation, data acquisition and the test environment to some extent have influence on the accuracy of the measurement system, and since errors cannot be totally eliminated in measurements, efforts were taken to minimize the sources of errors. For all the measurements, errors introduced by the data acquisition system were small, and were therefore neglected. For the mean drag coefficient, the largest contributing error was the uncertainty in the drag force measured by the force balance and its calibration; the error in the freestream dynamic pressure was comparatively small. For the Strouhal number, the largest contributing error was the increment of the frequency axis in the power spectrum; the error in the freestream velocity was comparatively small. For the seven-hole probe measurements,

the largest contributor to the overall uncertainty came from the calibration data reduction method; the errors in the individual pressure measurements were small. Table 3.3 gives the summary of the uncertainty level in some of the measurement parameters.

Table 3.3: Summary of measurement uncertainty for selected measurements.

Parameter	Uncertainty
Drag coefficient, C_D (from Igbalajobi et al. (2013))	± 1% to ± 3%, depending on the prism aspect ratio
Strouhal number, St (from Igbalajobi et al. (2013))	± 0.2%
Wake velocity magnitude from seven-hole probe (from Adaramola et al. (2010))	± 5%
Freestream density, ρ_∞	± 2%
Freestream velocity, U_∞	± 1.5%

CHAPTER FOUR

RESULTS AND DISCUSSION – DRAG COEFFICIENT AND VORTEX SHEDDING

4.1 Introduction

In this chapter, the results obtained for the mean drag coefficient and vortex shedding measurements behind the prism with and without the splitter plate are presented and discussed. Measurements of the mean drag force coefficient (Section 4.2) were obtained with a force balance, and measurements of the vortex shedding frequency (Sections 4.3 and 4.4) were obtained with a single-component hot-wire probe positioned 4.5D downstream from the trailing edge of the prism-plate combination (in the wake of the combined body) at $x/D = L/D + 5$, $y/D = 2$ and allowed to vary along the height of the prism-plate combination from $z/D = 0.5$ (close to the ground plane) to 0.5D below the free end of the prism (i.e., to $z/D = 8.5$ to 2.5 for AR = 9 to 3, respectively), with a 0.5D increment. The experiments were conducted at a Reynolds number of $Re = 7.4\times10^4$ (corresponding to a freestream velocity of $U_\infty = 40$ m/s) for aspect ratios of AR = 9, 7, 5 and 3. The boundary layer thickness on the ground plane relative to the side length of the square prism was $\delta/D = 1.5$. The splitter plates were mounted on the wake centreline with negligible gap (0.5 mm) between the prism base and the plate's leading edge. Splitter plate lengths relative to the prism side length ranged from $L/D = 1$ to 7 (1, 1.5, 2, 3, 5 and 7), and the plate height was always equal to the prism height.

4.2 Mean Drag Coefficient

Data for the mean drag coefficient for the finite square prism with and without splitter plates are presented in Table 4.1 and represented graphically in Figure 4.1(a). Data from

selected infinite square prism and splitter plate experiments are included for reference. Note that the mean drag coefficients measured in these experiments are that of the square prism only; because the splitter plates were not attached to the prisms, the drag experienced by the splitter plates was not measured.

Table 4.1: Mean drag coefficient (C_D) measurements, Re = 7.4×10^4. Infinite prism data are from Park and Higuchi (1998).

L/D	AR = 9 (Uncertainty ±0.01)	AR = 7 (Uncertainty ±0.01)	AR = 5 (Uncertainty ±0.02)	AR = 3 (Uncertainty ±0.03)	Infinite prism
0	1.43	1.43	1.47	1.35	2.26
1	1.46	1.41	1.38	1.27	1.80
1.5	1.43	1.40	1.35	1.24	Not measured
2	1.42	1.38	1.33	1.23	1.62
3	1.38	1.36	1.31	1.21	Not measured
5	1.38	1.35	1.30	1.21	1.47
7	1.38	1.34	1.30	1.20	Not measured

For the finite square prism with no splitter plate (L/D = 0), the mean drag coefficients (ranging from C_D = 1.47 to 1.35) are lower than that of the infinite square prism (C_D = 2.26). This is largely due to the flow field around the finite prism being three-dimensional and the downwash flow which originates at the prism's free end and descends into the wake. This is similar to what was observed for a finite circular cylinder by Igbalajobi et al. (2013). However, for the finite square prism, it is noted that as the aspect ratio increases, C_D increases to a maximum value at AR = 5 (similar to McClean and Sumner (2012, 2014)), then decreases to a constant value for AR = 7 and 9. This is in contrast with the finite circular cylinder where an increase in AR is accompanied by an increase in C_D.

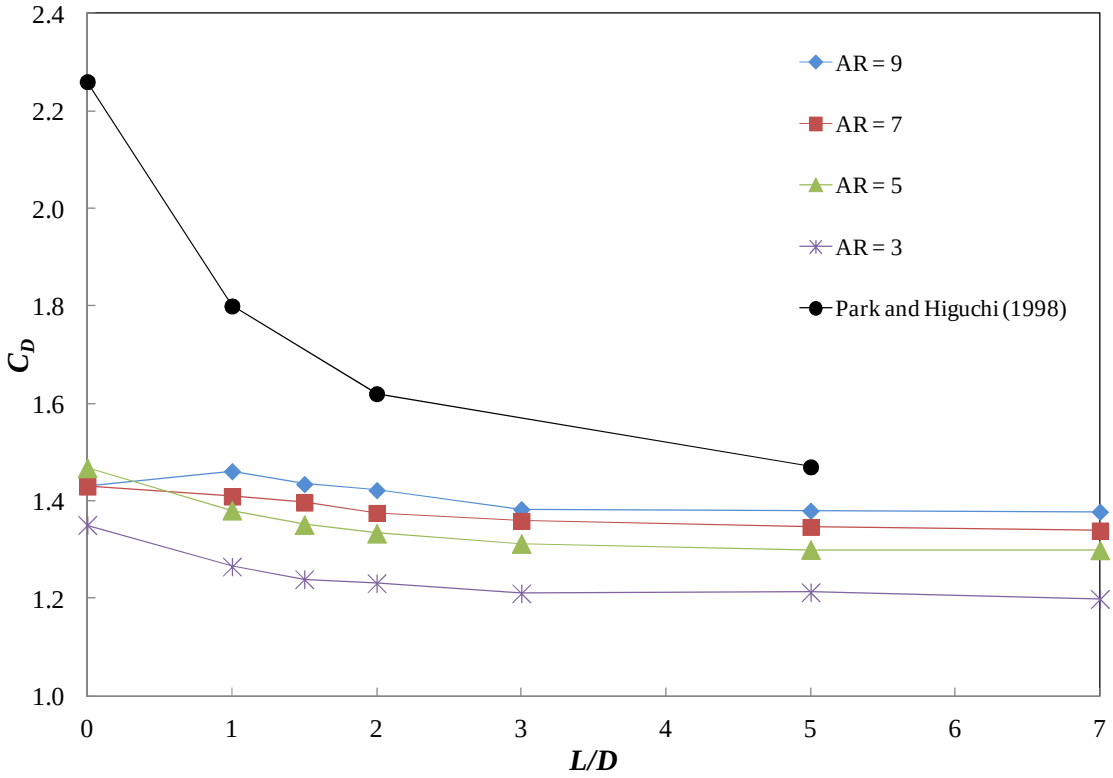

(a)

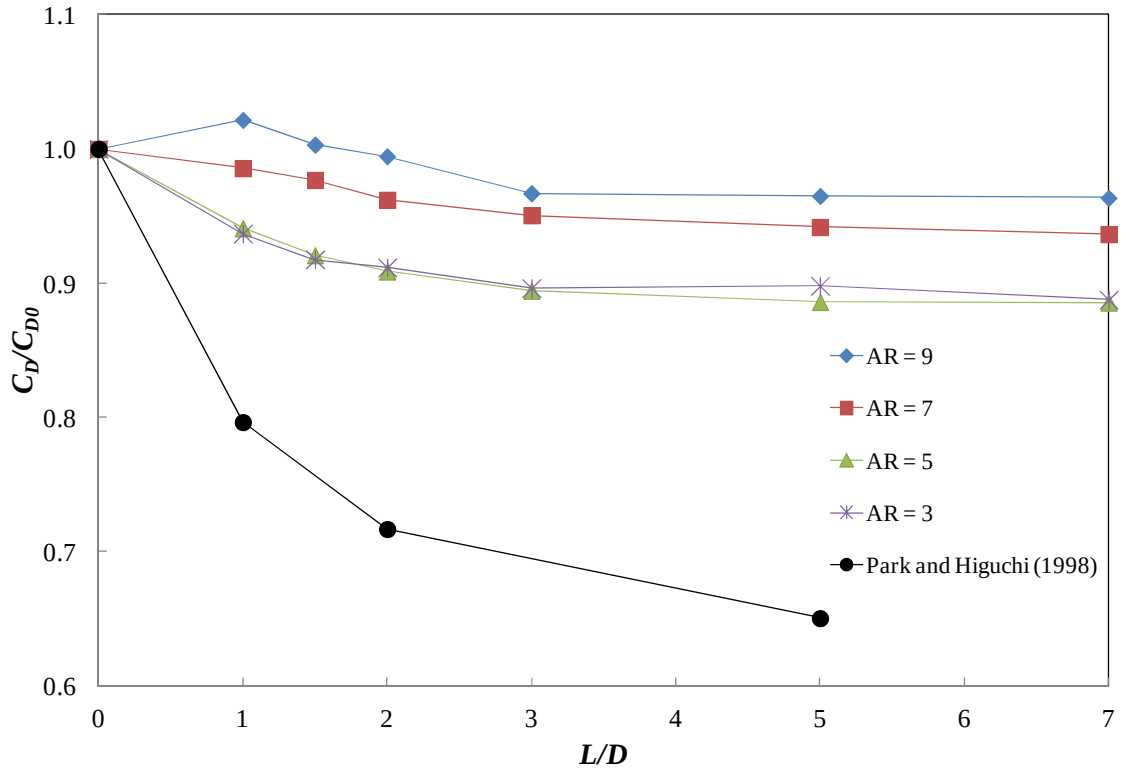

(b)

Figure 4.1: (a) Mean drag coefficient of a finite square prism with a splitter plate; (b) Normalized mean drag coefficient. Data from the present study, Re = 7.4×10^4; Infinite prism data are from Park and Higuchi (1998).

With a splitter plate of length L/D = 1 installed (Figure 4.1(a)), a slight reduction in the mean drag coefficient is observed for all the aspect ratios except for AR = 9 where there is a small increase (2%) in the C_D. For longer plates, $L/D \geq 1.5$, C_D for AR = 9 decreases to the no-splitter-plate value and then follows the C_D reduction trend like the other prisms (AR = 7, 5 and 3). With the uncertainty level in the measurement, C_D tends to become constant (for all the aspect ratios) for $L/D \geq 3$. In general, the C_D decreases as L/D is increased.

The highest reduction in drag in the experiments occurred for the square prism of AR = 5 with splitter plates of $L/D \geq 5$, where there is an 11% drag reduction from C_D = 1.47 to C_D = 1.30. A similar reduction of 11% is seen for the prism of AR = 3 with a splitter plate of L/D = 7 (from C_D = 1.35 to C_D = 1.20). When compared with the infinite square prism, a 35% drag reduction was obtained for L/D = 5 (Park and Higuchi (1998)). Hence, the splitter plate is more effective at reducing the drag of an infinite square prism than for a finite prism.

For the prisms of AR = 9 and AR = 7, the drag reduction is much lower and almost negligible for some prism-plate combinations. In contrast, Igbalajobi et al. (2013) observed that for a finite circular cylinder-splitter plate combination, the highest drag (C_D) reduction was 12% for AR = 9 (the most slender cylinder) and short splitter plates ($L/D \leq 3$).

In Figure 4.1(b), the mean drag coefficient data are plotted normalized with the drag coefficient for the case of no splitter plate, C_{D0}, which removes dependencies on Reynolds number and aspect ratio. The graph more clearly illustrates the reduced effectiveness of the splitter plate for the finite square prism. This graph also shows the distinct splitter plate behaviour for AR = 9. A local maximum mean drag coefficient occurs at L/D = 1, similar to what is seen in the finite circular cylinder-plate combination with L/D = 1.5 (Igbalajobi et al., 2013). In addition, the behaviour of the data for AR = 3 and 5 are the same and distinct from the other two aspect ratios. This behaviour supports the existence of a different flow pattern for the two short prisms which suggests that for the present experimental conditions, AR = 3

and 5 are below the critical aspect ratio. This contrasts with what McClean and Sumner (2012, 2014) reported in their study where the critical aspect ratio was found to be between AR = 3 and 5.

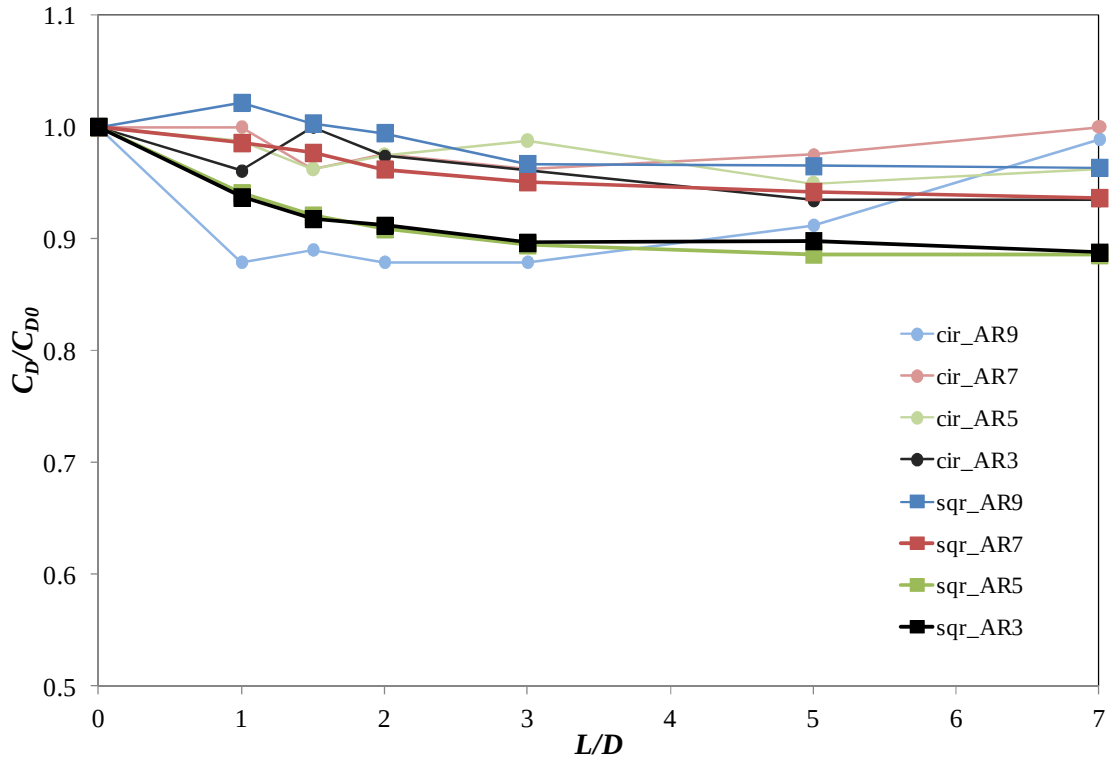

Figure 4.2: Normalized mean drag coefficient of a finite circular cylinder (cir) and finite square prism (sqr) with a splitter plate for different aspect ratios (AR). Finite circular cylinder data are from Igbalajobi et al. (2013). For both data sets, Re = 7.4×10^4.

Figure 4.2 shows the normalized mean drag coefficient plot (combined) of a finite circular cylinder (data from Igbalajobi et al. (2013)) and finite square prism (present study). The plot shows that for a square prism, the mean drag reduces as the splitter plate length is increased (except for AR = 9 and L/D = 1). Comparing the aspect ratios, the square prism has its highest C_D reduction (%) with longer splitter plates (11% for AR = 3, L/D = 7; 11% for AR = 5, $L/D \geq 5$; 6% for AR = 7, L/D = 7; and 4% for AR = 9, L/D = 7). In contrast, finite circular cylinders have their highest C_D reduction (%) with longer splitter plates for AR $\leq$ 5 (7% for AR = 3, $L/D \geq 5$; and 5% for AR = 5, L/D = 5) and shorter splitter plates for AR $\geq$ 7

(4% for AR = 7, L/D = 1.5 to 3; and 12% for AR = 9, L/D = 1 to 3). It is noted that for AR ≤ 5, both the circular cylinder and the square prism-plate combination have their highest drag reduction (%) at splitter plate lengths of $L/D \geq 5$. On the contrary, for higher aspect ratios (AR = 7 and 9), the highest drag reduction (%) occurred at splitter plate lengths of L/D = 1.5 to 3 for the circular cylinder and L/D = 7 for the square prism. This behaviour could be as a result of the fixed separation points, as well as wider and taller wake of the square prism. Hence, longer splitter plates would be needed to produce a noticeable reduction in drag.

4.3 Strouhal Number and Vortex Shedding at Mid-Height

The Strouhal number data at the mid-height position (z/H = 0.5) with and without splitter plates are presented in Table 4.2 and Figure 4.3. The absence of a Strouhal number in Table 4.2 shows that no vortex shedding peak was found, i.e. vortex shedding from the square prism has been suppressed. Data from selected infinite square prism and splitter plate experiments are included for reference. For the finite square prism, the Strouhal numbers are all lower than the case of the infinite square prism. The data behave similarly to the infinite square prism with a maximum value obtained at L/D = 0 (no splitter plate) and decreasing as L/D increases until full suppression of vortex shedding is achieved. This behaviour (see Table 4.2) is consistent with what was reported by Hasan and Budair (1994) and Park and Higuchi (1998) for infinite square prisms. However, the infinite prism numerical data of Park and Higuchi (1998) show a much greater reduction in St compared to the experimental data of Hasan and Budair (1994).

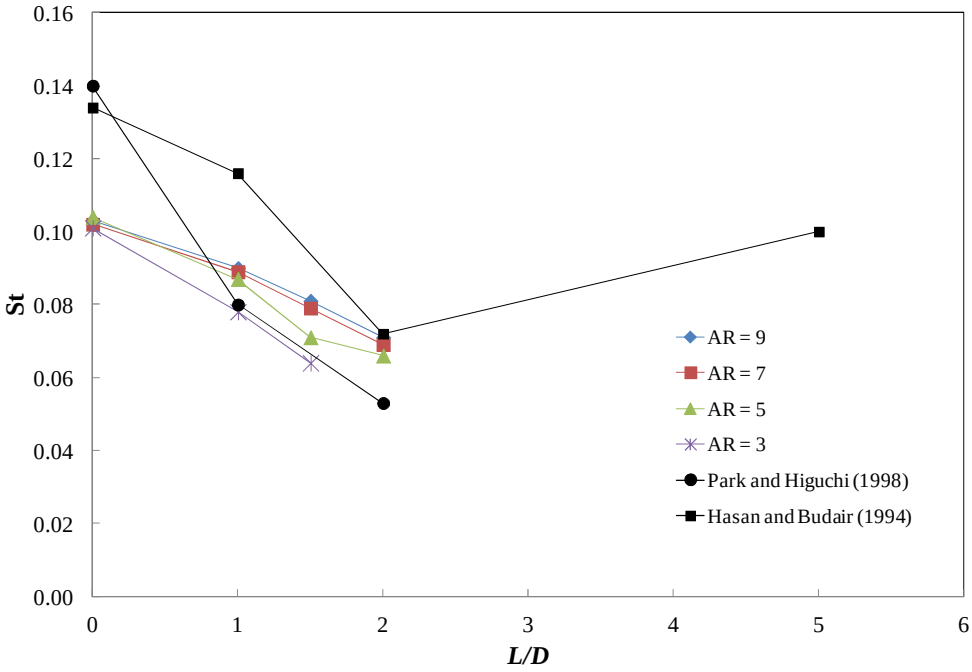

(a)

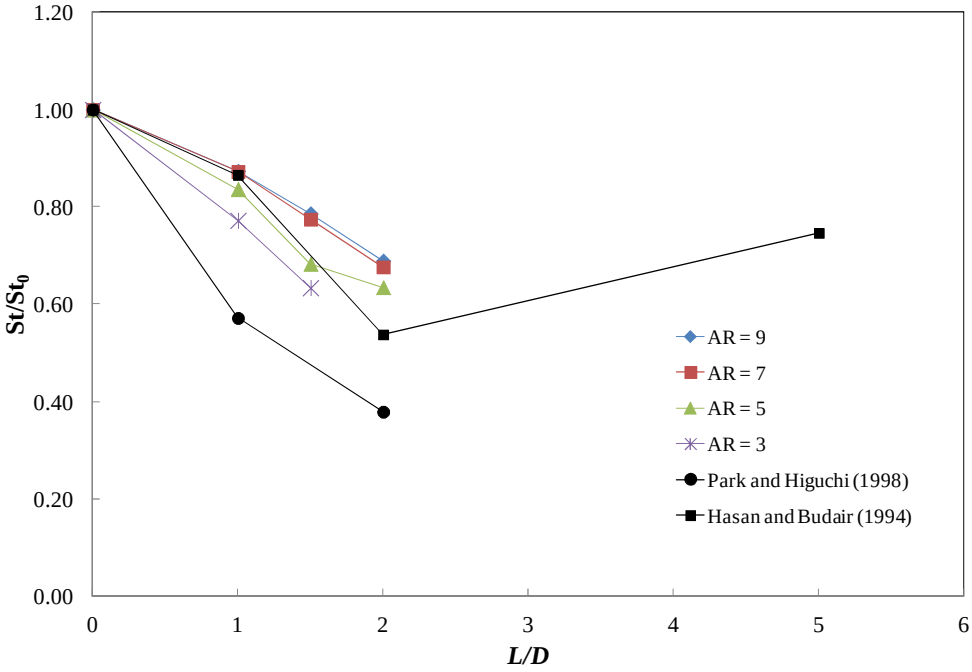

(b)

Figure 4.3: (a) Strouhal number at mid-height (z/H = 0.5) for a finite square prism with a wake-mounted splitter plate; (b) Normalized Strouhal number at mid-height. Data from the present study, Re = 7.4×10^4; Infinite prism data are from Park and Higuchi (1998) and Hasan and Budair (1994), Re = 1.2×10^4 – 2.4×10^4.

Table 4.2: Strouhal number (St) measurements at mid-height (z/H = 0.5), Re = 7.4×10^4. Infinite prism data are from Park and Higuchi (1998) [1] and Hasan and Budair (1994) [2], Re = $1.2\times10^4 - 2.4\times10^4$.

L/D	AR = 9 (Uncertainty ± 0.002)	AR = 7 (Uncertainty ± 0.002)	AR = 5 (Uncertainty ± 0.002)	AR = 3 Uncertainty ± 0.002)	Infinite prism	
					[1]	[2]
0	0.103	0.102	0.104	0.101	0.140	0.134
1	0.090	0.089	0.087	0.078	0.080	0.116
1.5	0.081	0.079	0.071	0.064	Not measured	Not measured
2	0.071	0.069	0.066	-	0.053	0.072
3	-	-	-	-	-	Not measured
5	-	-	-	-	-	0.100
7	-	-	-	-	-	-

Complete vortex shedding suppression is observed for AR = 3 with splitter plates of $L/D \geq 2$. For AR $\geq$ 5, splitter plates of $L/D \geq 3$ result in complete vortex shedding suppression. This is consistent with what was reported by Park and Higuchi (1998) for an infinite prism. Comparing this with the finite circular cylinder, splitter plates are more effective at suppressing vortex shedding from the circular cylinder especially for AR $\leq$ 7 (Igbalajobi et al., 2013). For a finite cylinder of AR = 3, complete vortex shedding suppression occurred beginning with the shortest splitter plate length, L/D = 1; for finite cylinders of AR = 5 and 7, complete vortex shedding suppression occurred with splitter plate lengths of $L/D \geq 1.5$. In contrast, however, for AR = 9, splitter plates are more effective for the square prism than the circular cylinder, with lengths $L/D \geq 3$ for the prism as against $L/D \geq 5$ needed for the cylinder to suppress vortex shedding.

Figure 4.4 shows the normalized Strouhal number data at the mid-height (z/H = 0.5) of a finite circular cylinder (data from Igbalajobi et al. (2013)) and finite square prism

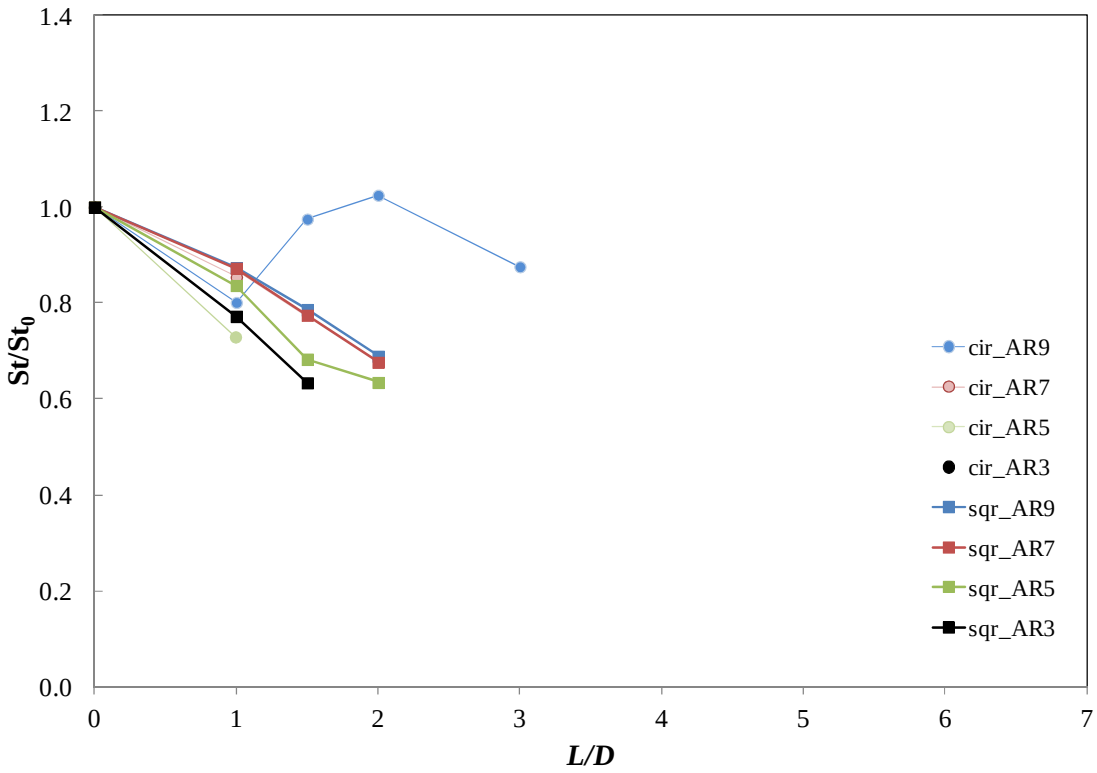

Figure 4.4: Normalized Strouhal number of a finite circular cylinder (cir) and finite square prism (sqr) with a splitter plate for different aspect ratios (AR). Finite circular cylinder data are from Igbalajobi et al. (2013). For both data sets, Re = 7.4×10^4.

(present study). The plot shows that for a square prism, the Strouhal number reduces as the splitter plate length is increased. This behaviour is also noticed for the finite circular cylinder except for AR = 9. It is also noted that while a splitter plate of length L/D = 3 will suppress vortex shedding from a square prism for all aspect ratios, L/D = 1.5 will be sufficient to suppress vortex shedding with a circular cylinder for all aspect ratios (except for cylinder of AR = 9, where longer plates of $L/D \geq 5$ are needed).

Further information on the splitter plate's effectiveness on a finite square prism can be seen in the power spectra (Figure 4.5). A peak in the power spectrum indicates the presence of a periodic flow (in this case, vortex shedding) with a recognized frequency (Strouhal number). A strong vortex shedding signal is represented by a tall peak, while a short peak represents a weak vortex shedding signal. As the peak becomes narrower, vortex shedding

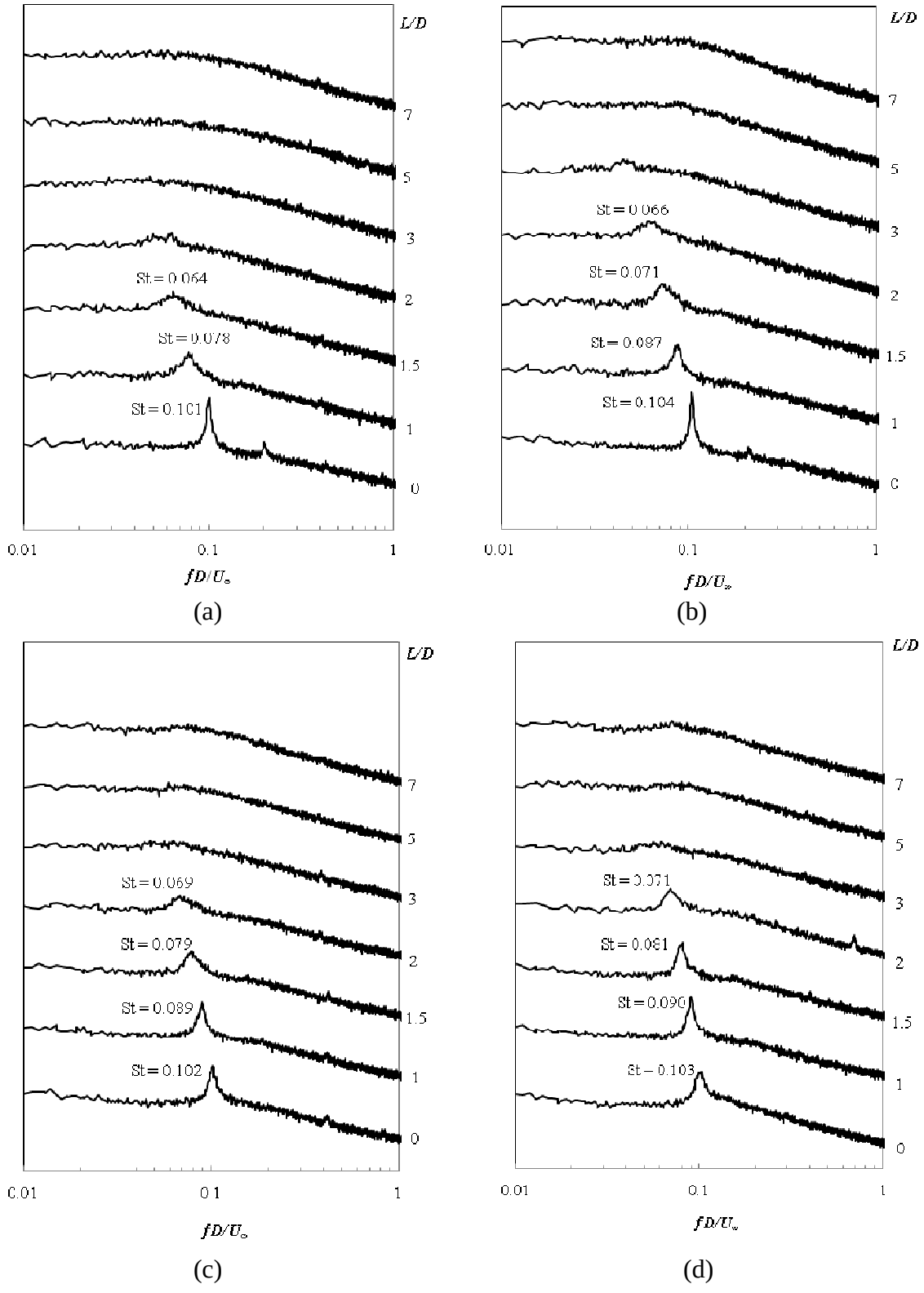

Figure 4.5: Power spectra for measurements at mid-height (z/H = 0.5) for a finite square prism: (a) AR = 3, (b) AR = 5, (c) AR = 7, (d) AR = 9. Each spectrum represents the average of 100 individual spectra. The vertical scale is arbitrary but the same scale is used for each spectrum.

frequency becomes more regular (steady) while a wide (broad) peak represents a more irregular vortex shedding frequency. The absence of a peak indicates the suppression or absence of periodic vortex shedding.

For the case of no splitter plate (L/D = 0), strong vortex shedding peaks are seen for all four aspect ratios, and their Strouhal numbers are independent of aspect ratio. Their values compare favourably with the results from McClean and Sumner (2012, 2014), where St = 0.102 for AR = 3, St = 0.105 for AR = 5, St = 0.101 for AR = 7 and St = 0.100 for AR = 9 (Re = 7.2×10^4, δ/D = 1.5) were obtained.

For AR = 3, Figure 4.5(a), the addition of a splitter plate of L/D = 1 reduces the magnitude of the Strouhal number from St = 0.101 to St = 0.078 and the vortex shedding peak becomes weaker and more broad-banded. For the splitter plate of L/D = 1.5, the magnitude is reduced to St = 0.064 and the vortex shedding peak becomes wider. For longer plates ($L/D \geq 2$), no discernible peaks are found in the power spectra indicating that vortex shedding has been suppressed. For AR = 5, 7 and 9, Figures 4.5(b,c,d), vortex shedding still occurs with the splitter plate of L/D = 2, although the vortex shedding peak has become more broad-banded. For longer plates ($L/D \geq 3$), no discernible peaks are found in the power spectra indicating that vortex shedding has been suppressed.

4.4 Strouhal Number and Vortex Shedding along the Height

The power spectra obtained along the height of the square prism, from 0.5D near the ground plane to 0.5D from the free end, are shown in Figures 4.6, 4.7, 4.8 and 4.9 for AR = 3, 5, 7 and 9, respectively. The spectra clearly show vortex shedding peak variation along the prism height. The sharp peaks seen in some of the spectra at high frequencies are due to electronic noise present in the wind tunnel. Also, other small peaks seen close to the free end are due to the freestream flow which is not related to the prism and splitter plate. These

small-magnitude peaks are present even when there was no prism and splitter plate in the wind tunnel test section.

4.4.1 Power Spectra along the Height for AR = 3

The power spectra for the cylinder of AR = 3 are shown in Figure 4.6 for x/D = 5 (for the prism) and $x/D = L/D + 5$ (for the prism-plate combination) measurement positions. From Figure 4.6(a), i.e. for the prism of AR = 3 without a splitter plate (L/D = 0), very strong vortex shedding peaks are found at all measurement locations along the height of the prism, including positions close to the ground plane and near the free end. This behaviour is consistent with what was reported by Igbalajobi et al. (2013) for a finite cylinder of AR = 3, but contrasts with what Sumner et al. (2004) reported for finite circular cylinders of AR = 3 where vortex shedding peaks were much weaker. However, in the experiments of Sumner et al. (2004), the boundary layer was much thicker (δ/D = 2.6) than in the experiments of Igbalajobi et al. (2013) and the present study (δ/D = 1.5). The influence of δ/D on the flow around a square prism has not been extensively studied. Therefore, conclusions cannot be drawn on the effect of the boundary layer difference.

For the splitter plate of length L/D = 1, Figure 4.6(b), the power spectrum is similar to what was observed for the case of no splitter plate although the vortex shedding peaks are slightly weaker and more broad-banded. The peaks become weaker as L/D increases (L/D = 1.5; Figure 4.6(c)). With splitter plate of lengths of $L/D \geq 2$, Figures 4.6(d,e,f,g), vortex shedding peaks disappear for AR = 3. This indicates complete vortex suppression for the prism.

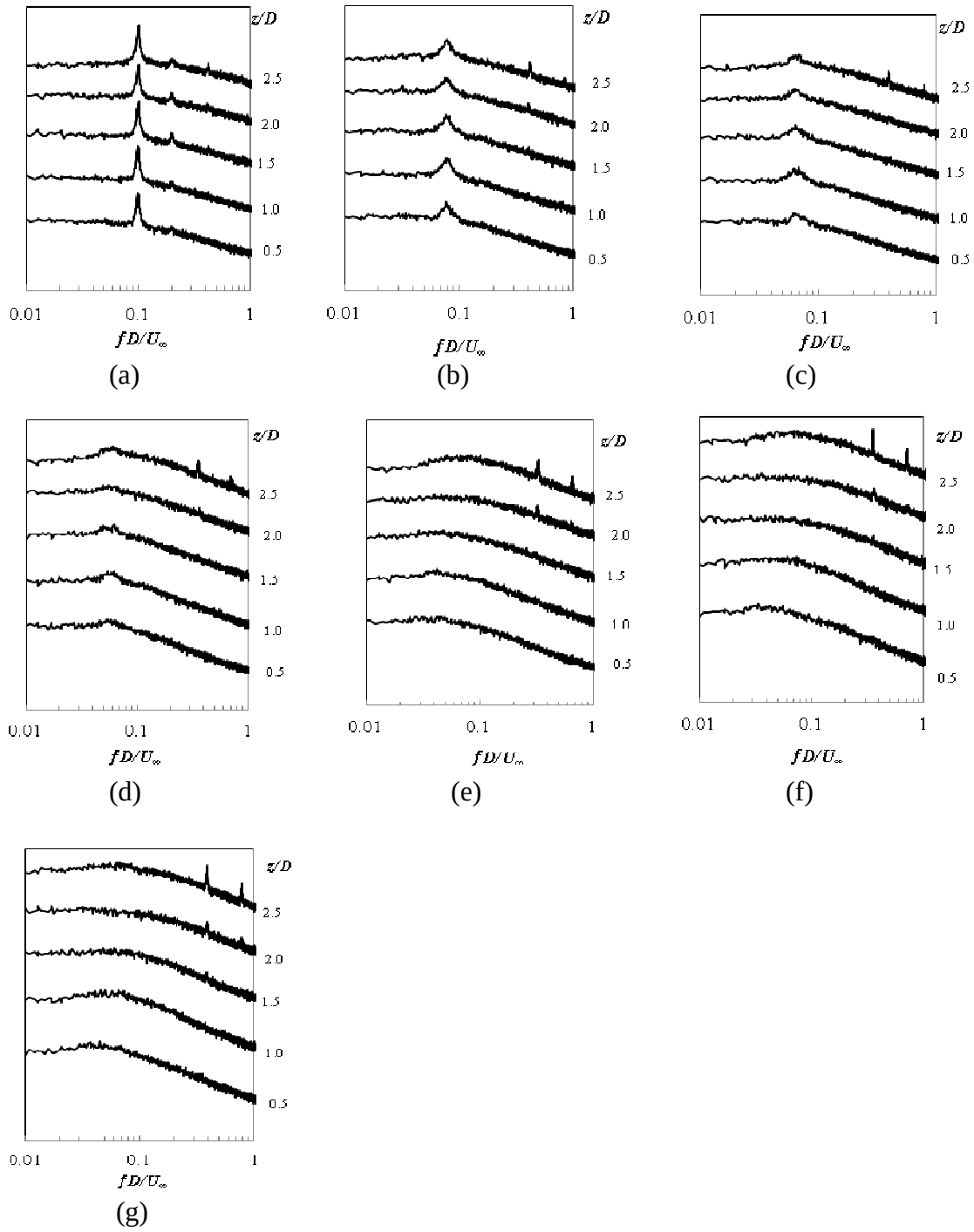

Figure 4.6: Power spectra for a finite square prism of AR = 3 with a wake-mounted splitter plate, Re = 7.4×10^4, hot-wire probe positioned downstream of the plate at $x/D = L/D + 5$, $y/D = 2$, and allowed to vary in the wall-normal direction (varying z/D): (a) $L/D = 0$, $x/D = 5$; (b) $L/D = 1$, $x/D = 6$; (c) $L/D = 1.5$, $x/D = 6.5$; (d) $L/D = 2$, $x/D = 7$; (e) $L/D = 3$, $x/D = 8$; (f) $L/D = 5$, $x/D = 10$; (g) $L/D = 7$, $x/D = 12$. The vertical scale is arbitrary but the same scale is used for each spectrum.

4.4.2 Power Spectra along the Height for AR = 5

The power spectra for the cylinder of AR = 5 are shown in Figure 4.7 for x/D = 5 (for the prism) and $x/D = L/D + 5$ (for the prism-plate combination) measurement positions. For the case of no splitter plate, L/D = 0 (Figure 4.7(a)), very strong vortex shedding peaks are found at all measurement locations along the height of the prism, including positions close to the ground plane and near the free end. This behaviour also is consistent with what was reported by Igbalajobi et al. (2013) but contrasts with what Sumner et al. (2004) reported for finite circular cylinders of AR = 5 where vortex shedding peaks were much weaker close to the ground plane.

For the splitter plate of L/D = 1, the results for the prism of AR = 5 (Figure 4.7(b)), are similar to what was observed for the case of no splitter plate except that the vortex shedding peaks are weaker and more broad-banded. This contrasts with what Igbalajobi et al. (2013) observed in their study for the same aspect ratio and splitter plate combination for a circular cylinder. The same trend is observed for L/D = 1.5 (Figure 4.7(c)).With a splitter plate of length L/D = 2, Figure 4.7(d), weaker and broad-banded vortex shedding peaks are found. For $L/D \geq 3$, Figures 4.7(e,f,g), vortex shedding peaks disappear for prisms of AR = 5. This contrasts with what Igbalajobi et al. (2013) observed for similar cylinder-plate combinations where weaker vortex shedding peaks were found close to the cylinder free end for $L/D \geq 3$.

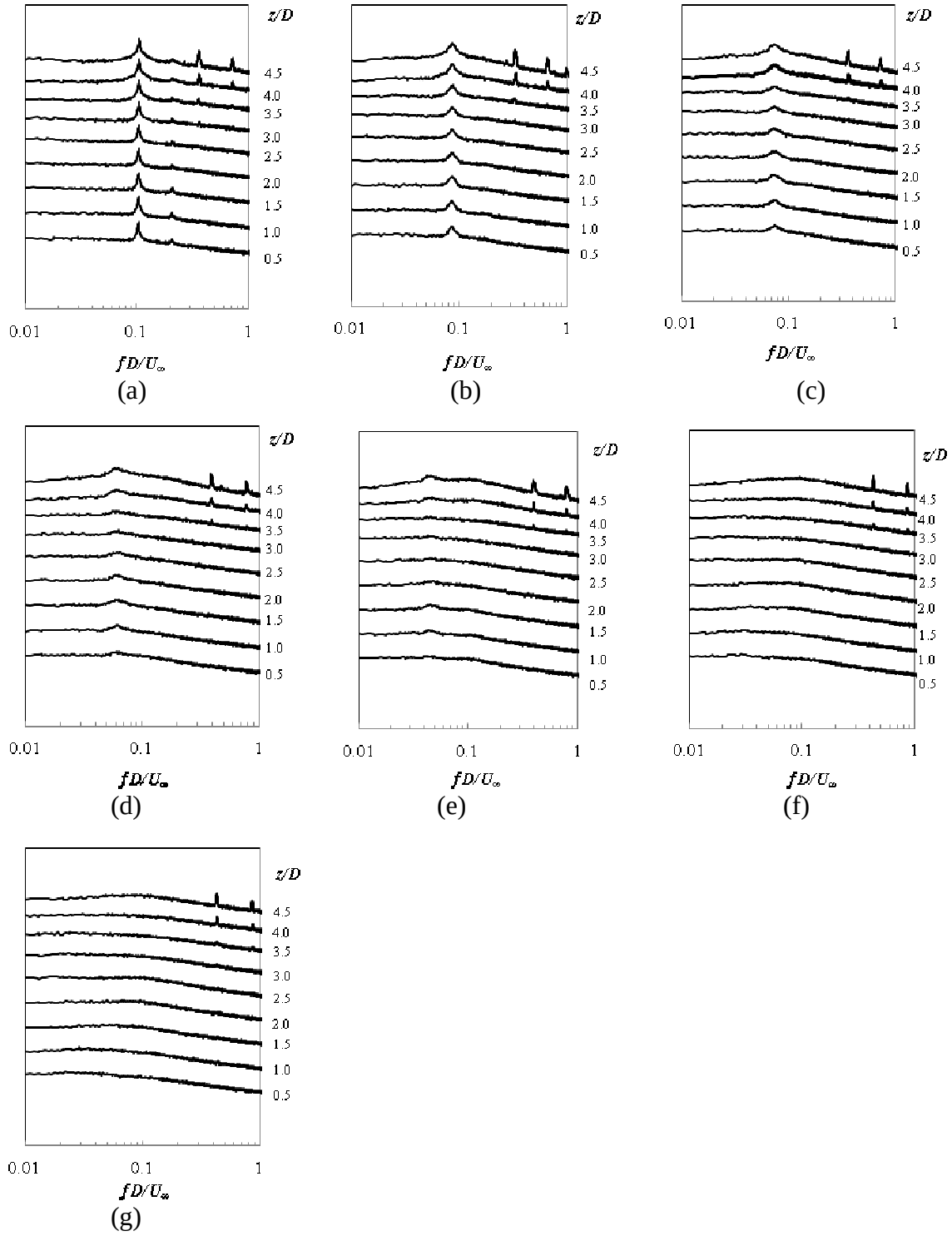

Figure 4.7: Power spectra for a finite square prism of AR = 5 with a wake-mounted splitter plate, Re = 7.4×10^4, hot-wire probe positioned downstream of the plate at $x/D = L/D + 5$, $y/D = 2$, and allowed to vary in the wall-normal direction (varying z/D): (a) $L/D = 0$, $x/D = 5$; (b) $L/D = 1$, $x/D = 6$; (c) $L/D = 1.5$, $x/D = 6.5$; (d) $L/D = 2$, $x/D = 7$; (e) $L/D = 3$, $x/D = 8$; (f) $L/D = 5$, $x/D = 10$; (g) $L/D = 7$, $x/D = 12$. The vertical scale is arbitrary but the same scale is used for each spectrum.

4.4.3 Power Spectra along the Height for AR = 7

The power spectra for the cylinder of AR = 7 are shown in Figure 4.8 for x/D = 5 (for the prism) and $x/D = L/D + 5$ (for the prism-plate combination) measurement positions, respectively. From Figure 4.8(a), i.e. without a splitter plate (L/D = 0), weaker vortex shedding peaks are encountered along the entire prism height (weaker and more broad-banded especially near the free end). Although weaker, no absence of vortex shedding was encountered. This is in contrast with the finite circular cylinder where vortex shedding peaks were absent for AR = 7 at positions close to the ground plane (Igbalajobi et al., 2013; Sumner et al., 2004).

With a splitter plate of L/D = 1, the result for the prism of AR = 7 (Figure 4.8(b)) is similar to what was observed for the case of no splitter plate although the vortex shedding peaks are slightly weaker and more broad-banded. The same pattern is observed for L/D = 1.5 and 2 (Figures 4.8(c,d)). With splitter plate of lengths of $L/D \geq 3$, Figures 4.8(e,f,g) vortex shedding peaks disappear along the prism height.

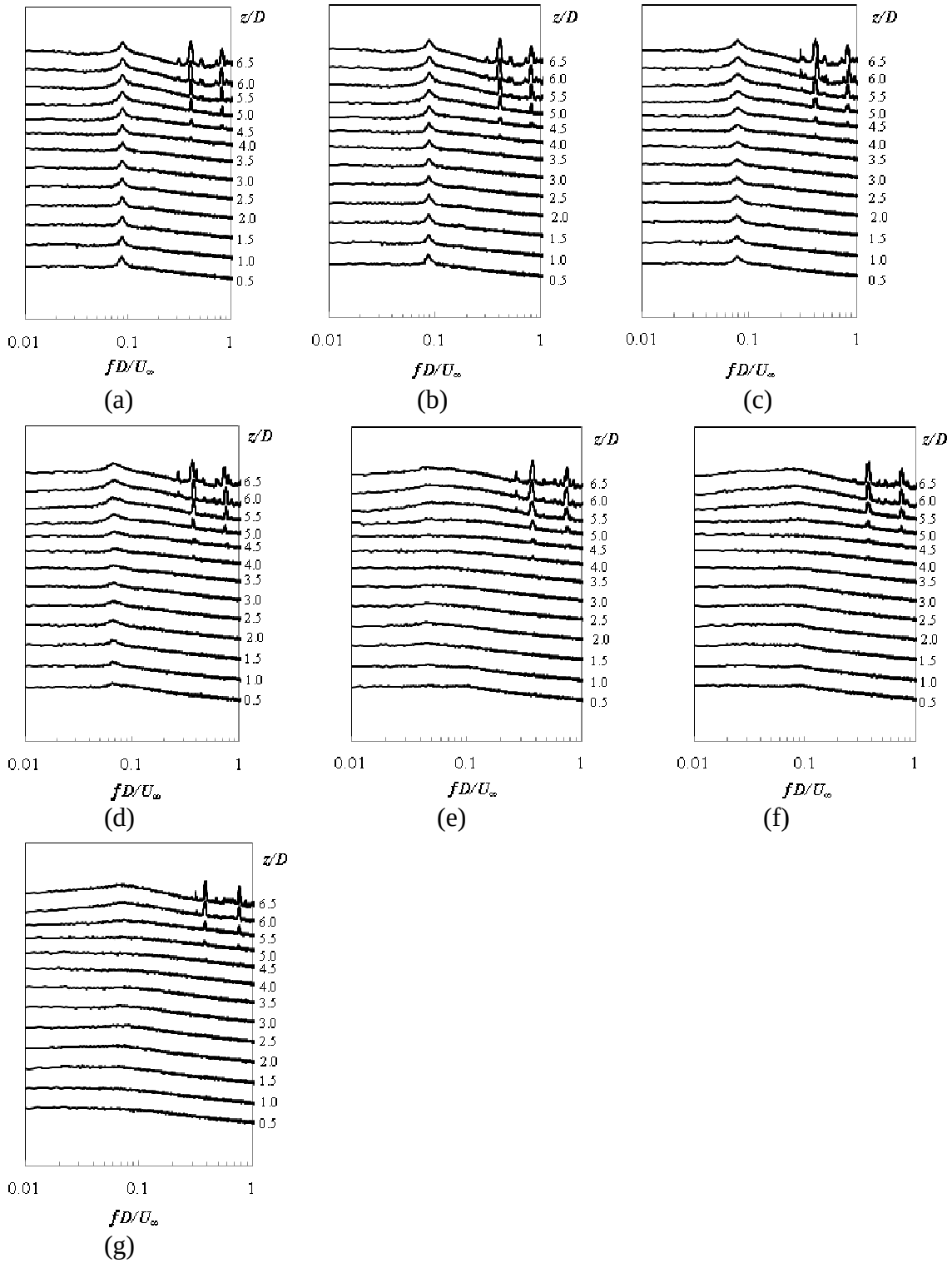

Figure 4.8: Power spectra for a finite square prism of AR = 7 with a wake-mounted splitter plate, Re = 7.4×10^4, hot-wire probe positioned downstream of the plate at $x/D = L/D + 5$, $y/D = 2$, and allowed to vary in the wall-normal direction (varying z/D): (a) $L/D = 0$, $x/D = 5$; (b) $L/D = 1$, $x/D = 6$; (c) $L/D = 1.5$, $x/D = 6.5$; (d) $L/D = 2$, $x/D = 7$; (e) $L/D = 3$, $x/D = 8$; (f) $L/D = 5$, $x/D = 10$; (g) $L/D = 7$, $x/D = 12$. The vertical scale is arbitrary but the same scale is used for each spectrum.

4.4.4 Power Spectra along the Height for AR = 9

The power spectra for the cylinder of AR = 9 are shown in Figure 4.9 for x/D = 5 (for the prism) and $x/D = L/D + 5$ (for the prism-plate combination) measurement positions. From Figure 4.9(a), i.e. the no splitter plate (L/D = 0) condition, weaker vortex shedding peaks are encountered along the entire prism height (weaker and more broad-banded especially near the free end). Although weaker, no absence of vortex shedding was encountered. This is in contrast with the finite circular cylinder where vortex shedding peaks were absent for AR = 9 at positions close to the ground plane and the free end (Igbalajobi et al., 2013; Sumner et al., 2004).

For the splitter plate of L/D = 1, (Figure 4.9(b)), the vortex shedding peaks look stronger than for the case of no splitter plate, especially near the free end. The same pattern was observed for L/D = 1.5 and 2 (Figure 4.9(c,d)). However, weaker and broad-banded vortex shedding peaks are found with L/D = 2. For $L/D \geq 3$, vortex shedding peaks disappear. The only exception is L/D = 7 (Figure 4.9(g)) where vortex shedding peaks (although weak and broad-banded) reappear in the power spectra at $z/D \geq 7.0$, indicating that the splitter plate of L/D = 7 may act to shift vortex shedding away from the ground plane.

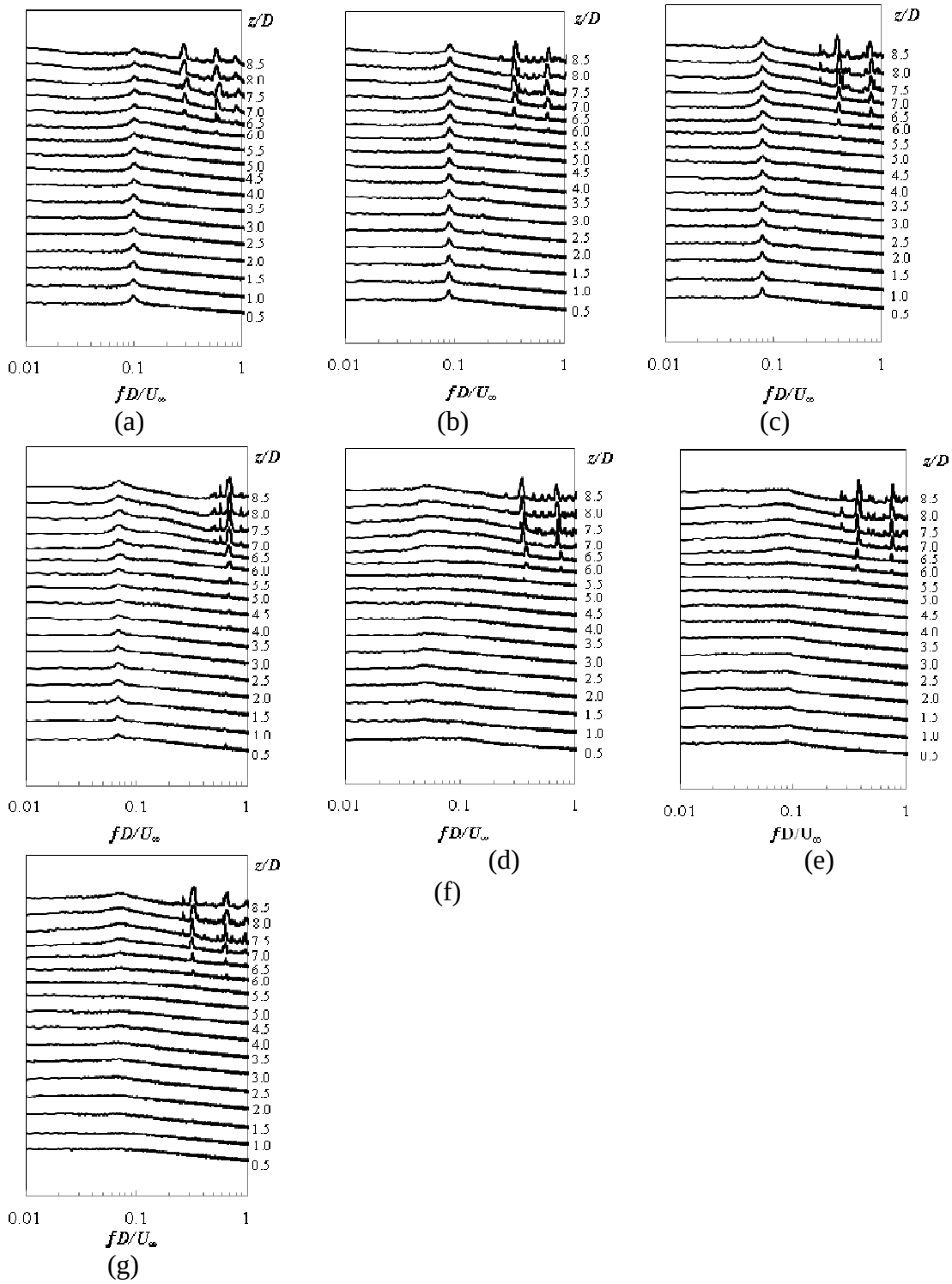

Figure 4.9: Power spectra for a finite square prism of AR = 9 with a wake-mounted splitter plate, Re = 7.4×10^4, hot-wire probe positioned downstream of the plate at $x/D = L/D + 5$, $y/D = 2$, and allowed to vary in the wall-normal direction (varying z/D): (a) $L/D = 0$, $x/D = 5$; (b) $L/D = 1$, $x/D = 6$; (c) $L/D = 1.5$, $x/D = 6.5$; (d) $L/D = 2$, $x/D = 7$; (e) $L/D = 3$, $x/D = 8$; (f) $L/D = 5$, $x/D = 10$; (g) $L/D = 7$, $x/D = 12$. The vertical scale is arbitrary but the same scale is used for each spectrum.

4.5 Summary

For the finite square prism with no splitter plate (L/D = 0), the mean drag coefficients (ranging from C_D = 1.47 to 1.35) were lower than that of the infinite square prism (e.g., Lee (1975) obtained C_D = 2.04 at Re = 1.76×10^5, Norberg (1993) obtained C_D = 2.15 at Re = 1.3×10^4, Park and Higuchi (1998) obtained C_D = 2.26, Taylor and Vezza (1999) obtained C_D = 2.38 at Re = 2.0×10^4, Yen and Yang (2011) obtained C_D = 2.02 at Re = 3.6×10^4). They obtained these values when the prism was at zero-incidence (α = 0°), similar to the orientation of this present experiment. This is consistent with previous finite square prism and finite circular cylinder experiments (e.g., Igbalajobi et al. (2013), McClean and Sumner (2012, 2014)). The lower mean drag coefficient can be attributed to finite prism's three-dimensional flow field and the downwash descending into the wake from the flow over the prism's free end.

A splitter plate of length $L/D \geq 3$ reduces the mean drag coefficient to a nearly constant value for all the prisms tested. The reduction ranges from 4% for AR = 9 (for $L/D \geq 5$) to 11% for AR = 3 (for L/D = 7). A similar trend in the C_D reduction behaviour was observed for AR = 5 and AR = 3 which is distinct from AR = 9 and AR = 7. This suggests that both AR = 5 and 3 are below the critical aspect ratio for this experiment.

In terms of the splitter's plate effect on vortex shedding, a plate of sufficient length ($L/D \geq 3$) was able to suppress Kármán vortex shedding for all of the prisms tested. Therefore, a splitter plate of length $L/D \geq 3$ will suppress vortex shedding as well considerably reduce the mean drag coefficient for all the prisms tested.

CHAPTER FIVE

RESULTS AND DISCUSSION – WAKE MEASUREMENTS

5.1 Introduction

In this chapter, the results obtained for the time-averaged wake velocity field measurements behind the prism with and without the splitter plate are presented and discussed. The measurements were made with a seven-hole probe. The experiments were conducted at a Reynolds number of Re = 3.7×10^4 (corresponding to a freestream velocity of U_∞ = 20 m/s) for aspect ratios of AR = 9 (presented in Section 5.2) and AR = 5 (presented in Section 5.3). These aspect ratios were chosen because each represents an example of the two main wake structures for the finite square prism. The splitter plates were mounted on the wake centreline with negligible gap (0.5 mm) between the prism base and the plate's leading edge. Splitter plate lengths of L/D = 1, 3, 5 and 7 were used and the plate height was always equal to the prism height. These measurements were carried out to allow for a better understanding of how the splitter plate affects the mean wake of the finite prism. The probe was positioned downstream at x/D = 10 (streamwise), was allowed to vary from y/D = −3 to +3 (cross-stream) and z ranged from approximately $D/3$ (close to the ground plane) to 1D above the prism free end in the wall-normal direction with approximately $D/6$ increments in both the y and z directions.

5.2 Wake Measurements for AR = 9

The velocity mean vector field, streamwise mean velocity contours, cross-stream mean velocity contours, wall-normal mean velocity contours, and the time-averaged

streamwise vorticity contours were obtained for the finite square prism of aspect ratio AR = 9 (different wake structure from lower aspect ratios). The results are presented below.

5.2.1 Velocity Vector Fields

The time-averaged mean velocity vector field for AR = 9 is shown in Figure 5.1. For the no splitter plate ($L/D = 0$) case, Figure 5.1(a), the velocity vector field at $x/D = 10$ shows the strong downwash (downward-directed velocity vectors) behind the prism and below the free end (tip). This, however, weakens along the prism axis towards the ground plane, similar to the case of the finite circular cylinder (Sumner et al., 2004). However, no noticeable upwash (upward-directed velocity vectors) flow from the ground plane is seen near the ground plane. This contrasts with what is observed for a finite circular cylinder of similar aspect ratio (Sumner et al., 2004).

With the splitter plates (Figures 5.1(b,c,d,e)), only small difference is observed in the velocity vector fields. However, the downwash becomes weaker as the splitter plate length increases ($L/D > 1$).

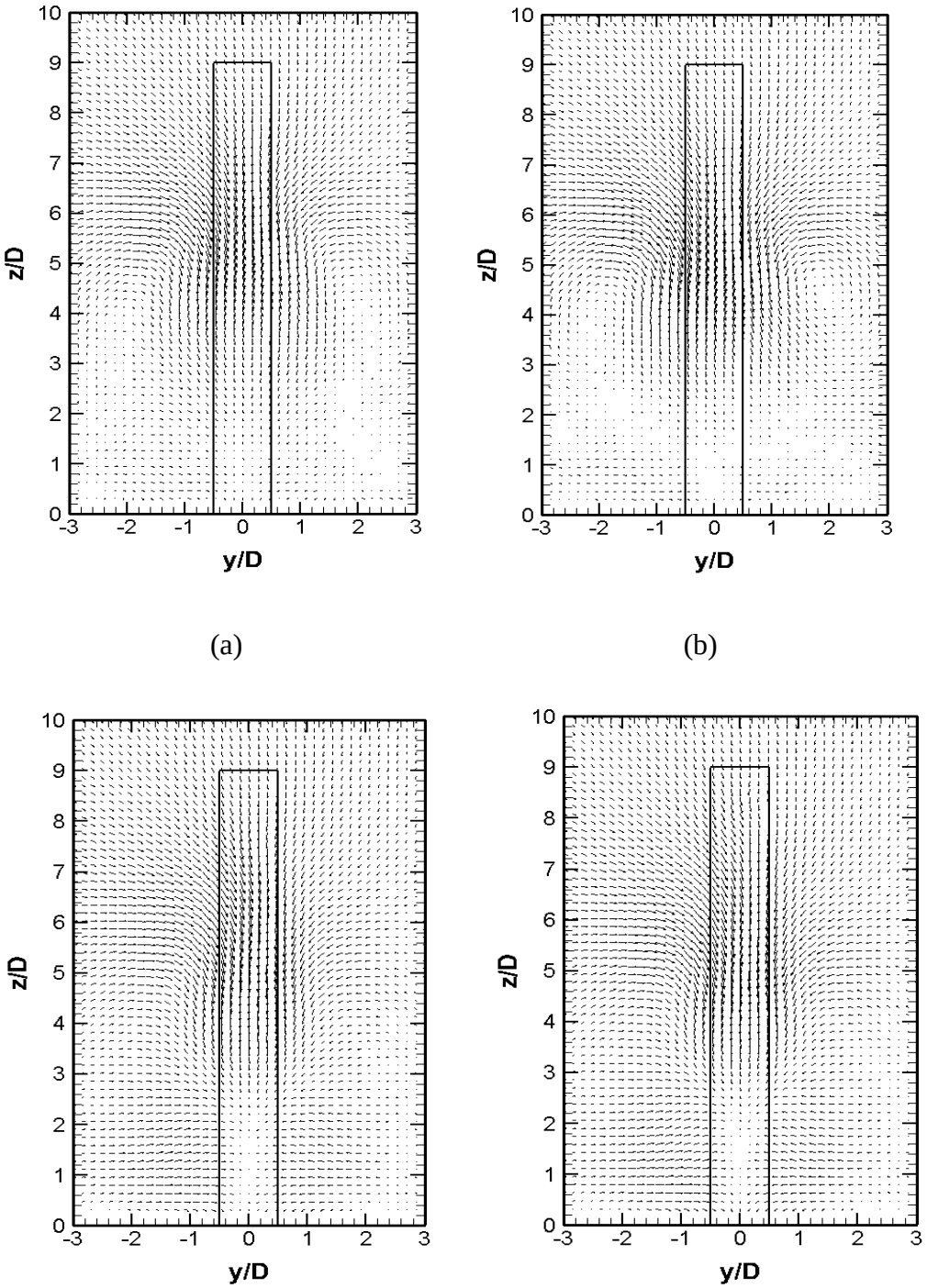

Figure 5.1: Mean velocity vector field in the wake of the square prism, AR = 9, x/D = 10: (a) L/D = 0, (b) L/D = 1, (c) L/D = 3, (d) L/D = 5, (e) L/D = 7.

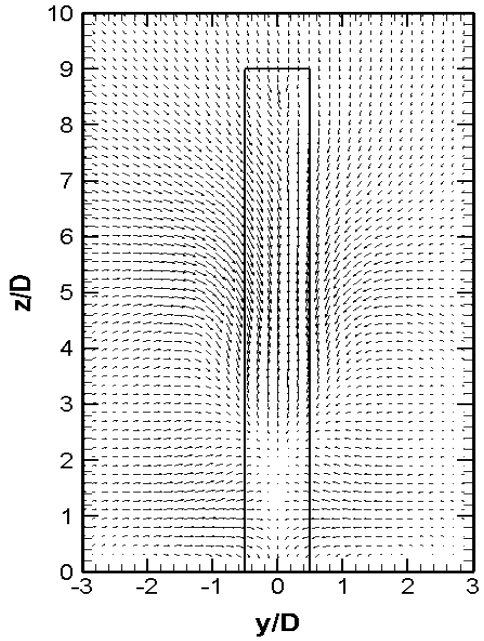

(e)

Figure 5.1 (continued)

5.2.2 Streamwise Mean Velocity

The time-averaged streamwise velocity field ($\overline{U}/U_\infty$) in the cross-stream (y-z) plane is shown as a contour plot in Figure 5.2. For the no splitter plate (L/D = 0) case, Figure 5.2(a), the lowest mean streamwise velocity ($\overline{U}/U_\infty$ = 0.35 contour) is found to be concentrated in a region behind the prism which originates from z/H = 0.1 (close to the ground plane) and rises along the prism height up to z/H = 0.4 (close to the prism's mid-height position). This is in contrast with the finite circular cylinder where lowest mean streamwise velocity ($\overline{U}/U_\infty$ = 0.6 contour) is only found in a region well above the ground plane (z/H = 0.4). In addition, only one peak ($\overline{U}/U_\infty$ = 0.95 contour) is recognized. This is similar to a finite circular cylinder of the same aspect ratio as observed by Adaramola et al. (2006) but has a wider wake width.

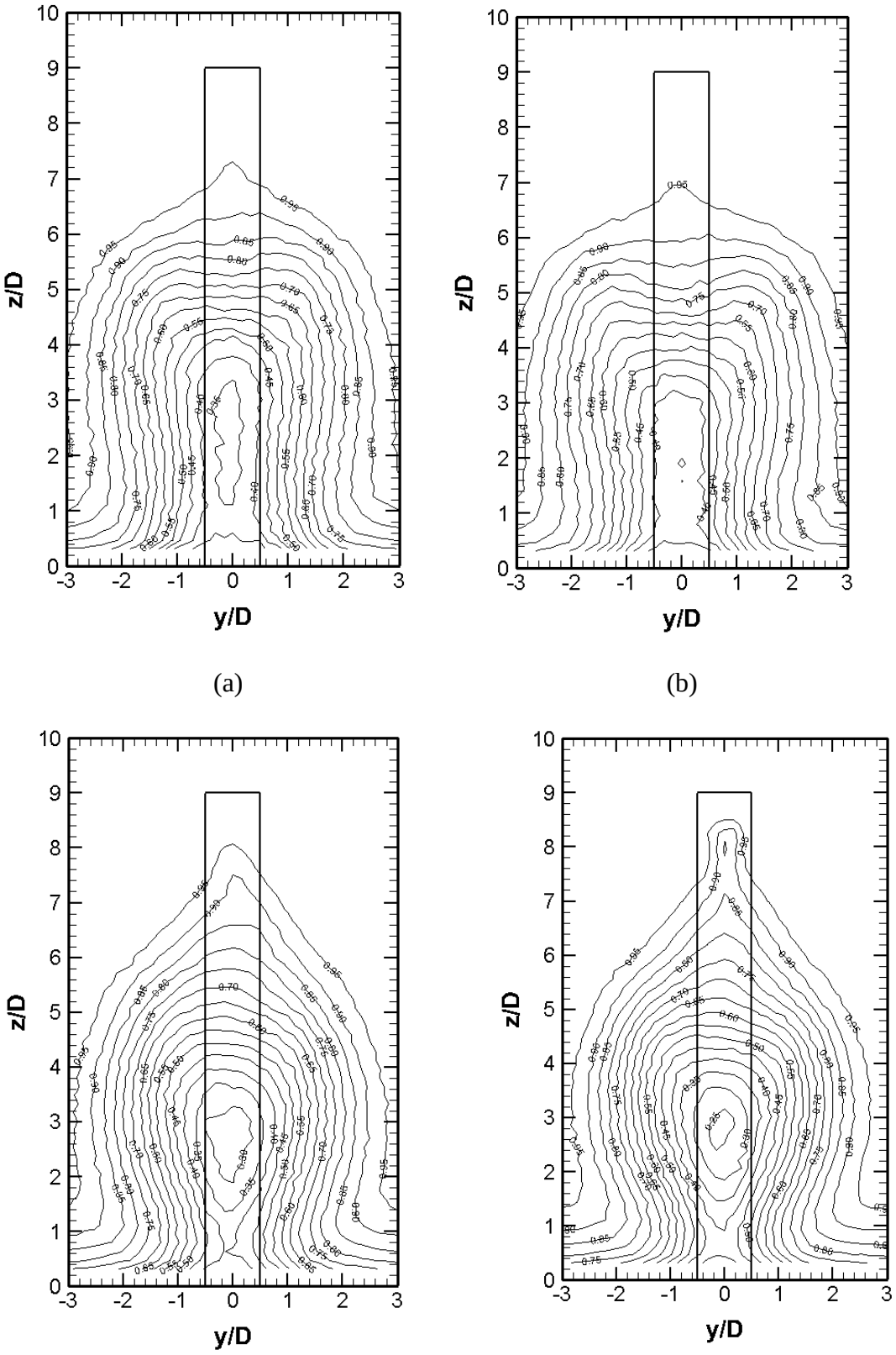

Figure 5.2: Streamwise mean velocity contours in the wake of the square prism, AR = 9, x/D = 10: (a) L/D = 0, (b) L/D = 1, (c) L/D = 3, (d) L/D = 5, (e) L/D = 7. Contour increment of U/U_∞ = 0.05.

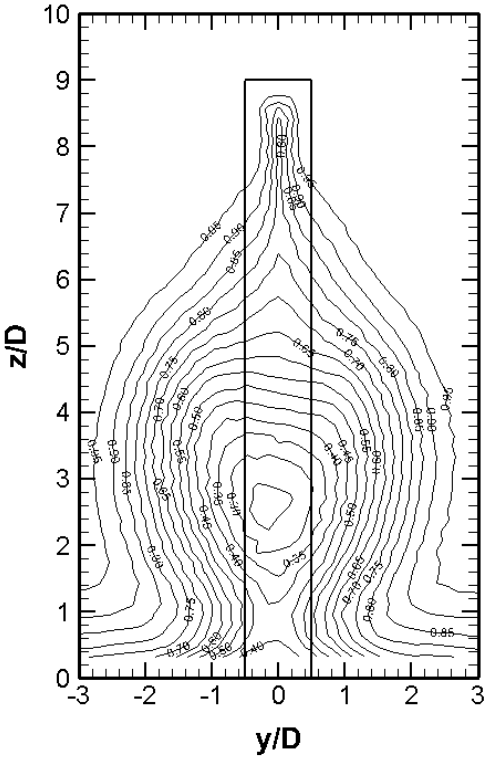

(e)

Figure 5.2 (continued)

With a short splitter plate, L/D = 1, Figure 5.2(b), the wake width (spread) increases. This widening of the wake may account for the small increase (2%) in drag as earlier observed (Section 4.2, Table 4.1). The wake height also reduces and the lowest mean streamwise velocity region ($\overline{U}/U_\infty$ = 0.4 contour, i.e. reduction in the velocity deficit) gets closer to the ground plane. Stronger splitter plate effects are first noticed with L/D = 3 (Figure 5.2(c)). This plate stretches (draws upwards) the wake along the prism height (flow around the prism becomes more two-dimensional). This is due to the additional drag of the splitter plate. The lowest mean streamwise velocity region ($\overline{U}/U_\infty$ = 0.3 contour) becomes smaller and moves closer to the ground plane (z/H = 0.3). For $L/D \geq 5$ (Figure 5.2(d,e)), the wake width becomes narrower especially closer to the ground plane (see ahead to Section 5.2.3), the velocity deficit ($\overline{U}/U_\infty$ = 0.25 contour) increased, and the splitter plate wake appears very close to the prism's free end.

5.2.3 Cross-stream Mean Velocity

The time-averaged cross-stream velocity field ($\overline{V}/U_\infty$) in the cross-stream (y-z) plane is shown as a contour plot in Figure 5.3. For the no splitter plate (L/D = 0) case, Figure 5.3(a), the flow is entrained towards the wake centreline (velocity vectors directed to the centreline) especially in the upper wake. This is not the case close to the ground plane where the entrainment is much weaker. The contours in Figure 5.3 are not perfectly symmetric on either side of the prism; this asymmetry may be due to a small misalignment of the prism compared to the freestream, a small misalignment of the plate relative to the prism and/or the freestream, a small misalignment of the seven-hole probe with the freestream, or a combination of these effects.

With a short splitter plate, L/D = 1, Figure 5.3(b), no significance difference is observed in the cross-stream velocity contours at x/D = 10. However, as the splitter plate length increases, L/D = 3, Figure 5.3(c), a very noticeable change occurs. Entrainment towards the wake centreline now occurs over the entire wake height. This is an indication of a strong velocity directed towards the splitter plate. This becomes stronger as the plate length increases, $L/D \geq 5$. This strong entrainment towards the centre of the wake may be responsible for narrowing the wake, especially for longer splitter plates as observed in Figure 5.2(d,e). This narrowing of the wake is associated with the reduction in drag coefficient of the prism (Section 4.2).

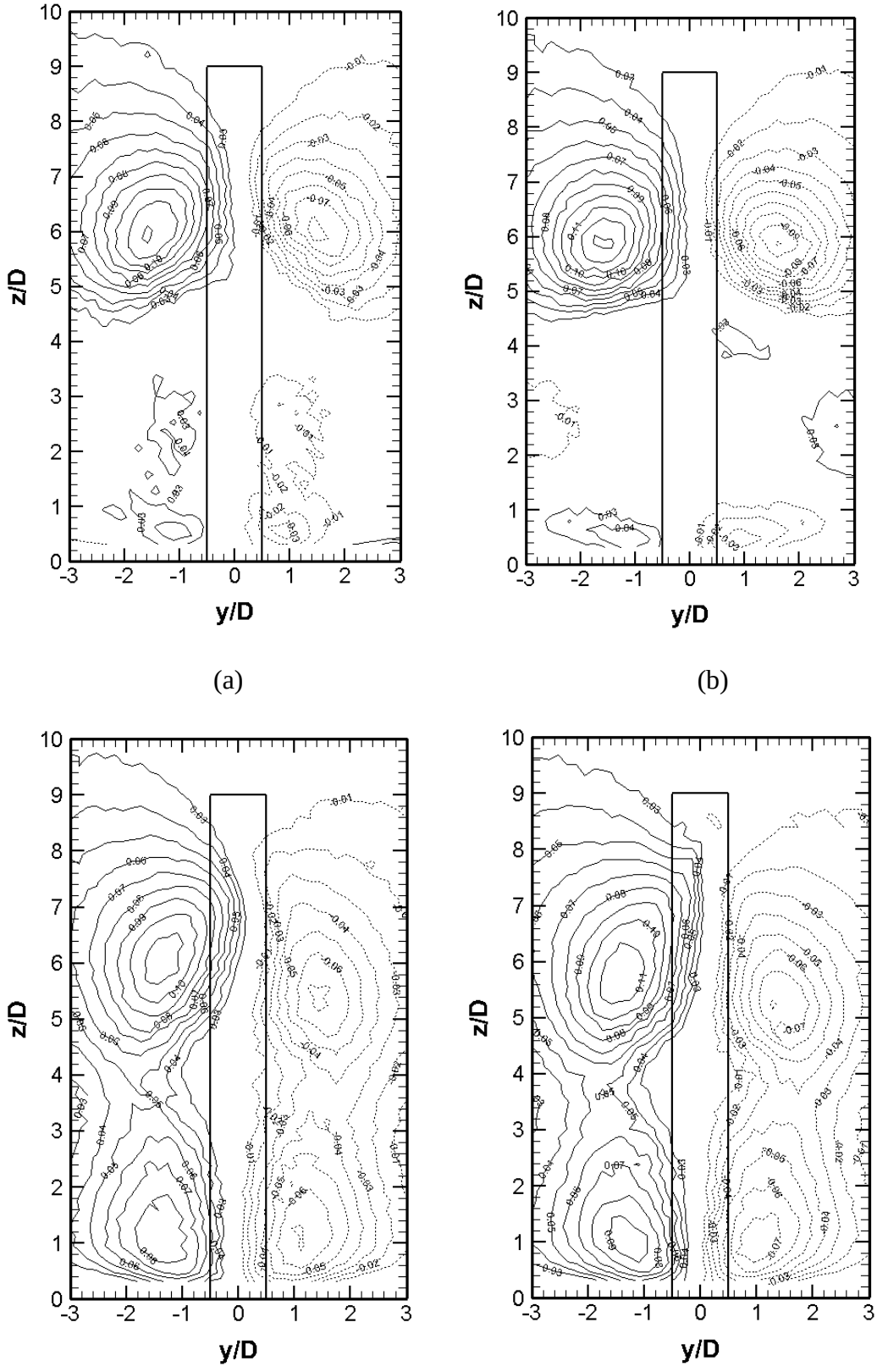

Figure 5.3: Cross-stream mean velocity contours in the wake of the square prism, AR = 9, x/D = 10: (a) L/D = 0, (b) L/D = 1, (c) L/D = 3, (d) L/D = 5, (e) L/D = 7. Contour increment of $\overline{V}/U_\infty$ = 0.01. Solid lines represent positive and dashed lines represent negative velocities.

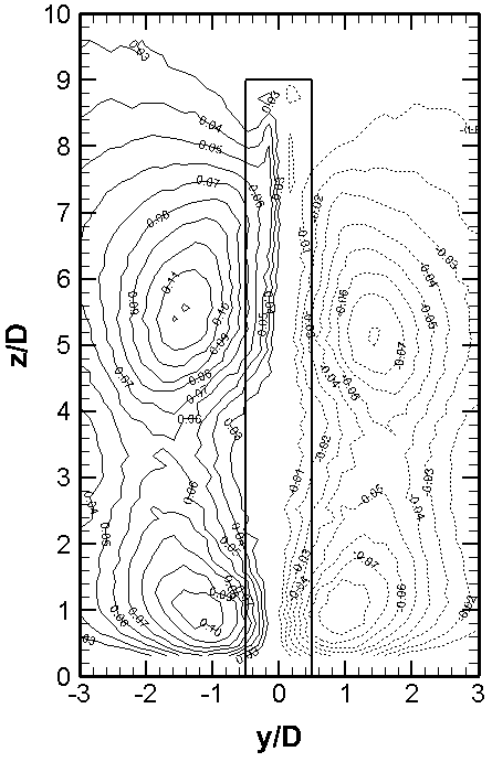

(e)

Figure 5.3 (continued)

5.2.4 Wall-normal Mean Velocity

The time-averaged wall-normal velocity field ($\overline{W}/U_\infty$) in the cross-stream (y-z) plane is shown as a contour plot in Figure 5.4. For the no splitter plate (L/D = 0) case, Figure 5.4(a), the presence of a strong downwash velocity (located between the tip vortex structures, see ahead to Figure 5.5), which originates from the prism's free end and descends into the wake, is observed. However, an upwash velocity field is absent, which contrasts with what is observed for a finite circular cylinder of the same aspect ratio (Adaramola et al., 2006). This could be a result of the difference in the probe streamwise positioning (x/D = 10 as against x/D = 6 for Adaramola et al. (2006)) as downwash and upwash strength both decrease with x/D.

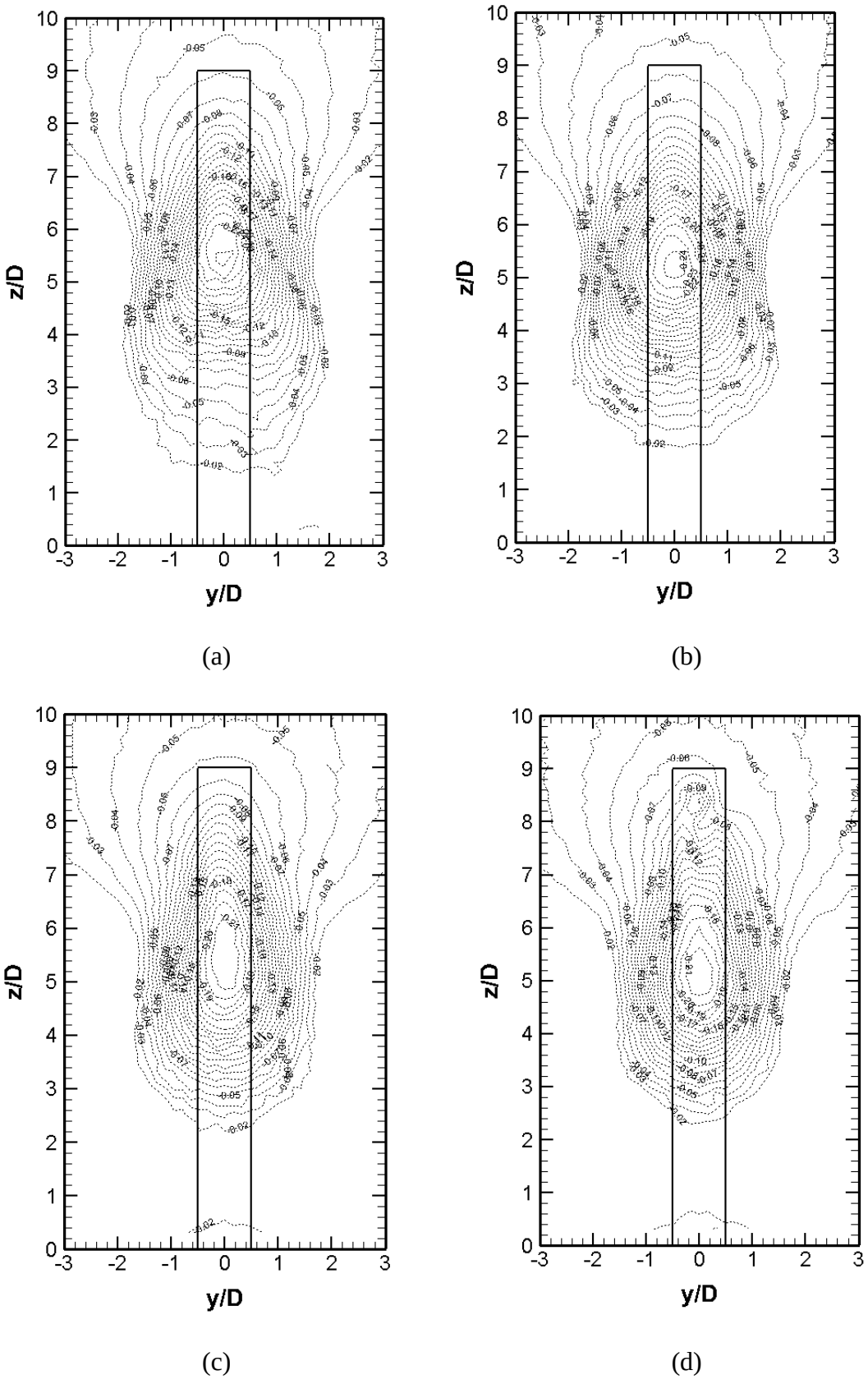

Figure 5.4: Wall-normal mean velocity contours in the wake of the square prism, AR = 9, x/D = 10: (a) L/D = 0, (b) L/D = 1, (c) L/D = 3, (d) L/D = 5, (e) L/D = 7. Contour increment of $\overline{W}/U_\infty$ = 0.01. Dashed lines represent negative (downward) velocity.

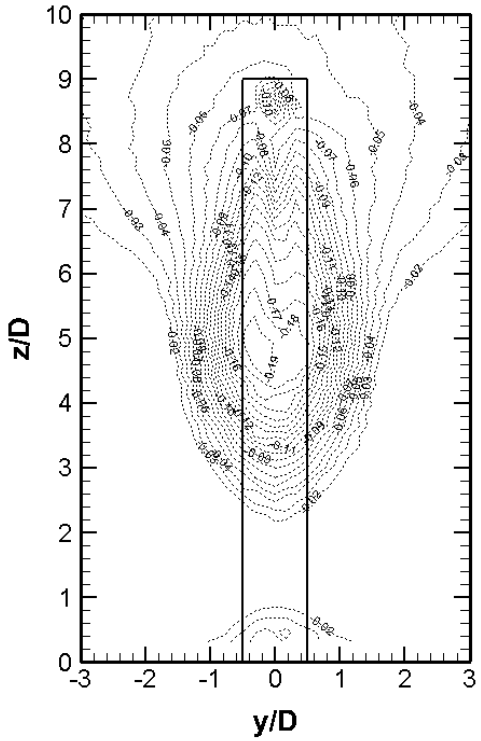

(e)

Figure 5.4 (continued)

For the prism-splitter plate combination of L/D = 1, Figure 5.4(b), the downwash region becomes wider and farther away from the ground plane (weaker downwash). With L/D = 3, Figure 5.4(c), the splitter plate narrows the downwash region and induces another flow region close to the ground plane. In addition, for longer splitter plates, $L/D \geq 5$, Figure 5.4(d,e), a small downwash region at the same height as the free end is observed. This also may be due to the induced flow from the splitter plate.

5.2.5 Time-averaged Streamwise Vorticity

The time-averaged streamwise vorticity field expressed in dimensionless form as $\omega_x D/U_\infty$ (where ω_x is the mean streamwise vorticity) in the cross-stream (y-z) plane is shown in Figure 5.5. For AR = 9, L/D = 0 (Figure 5.5(a)), the vorticity field shows a counter-rotating

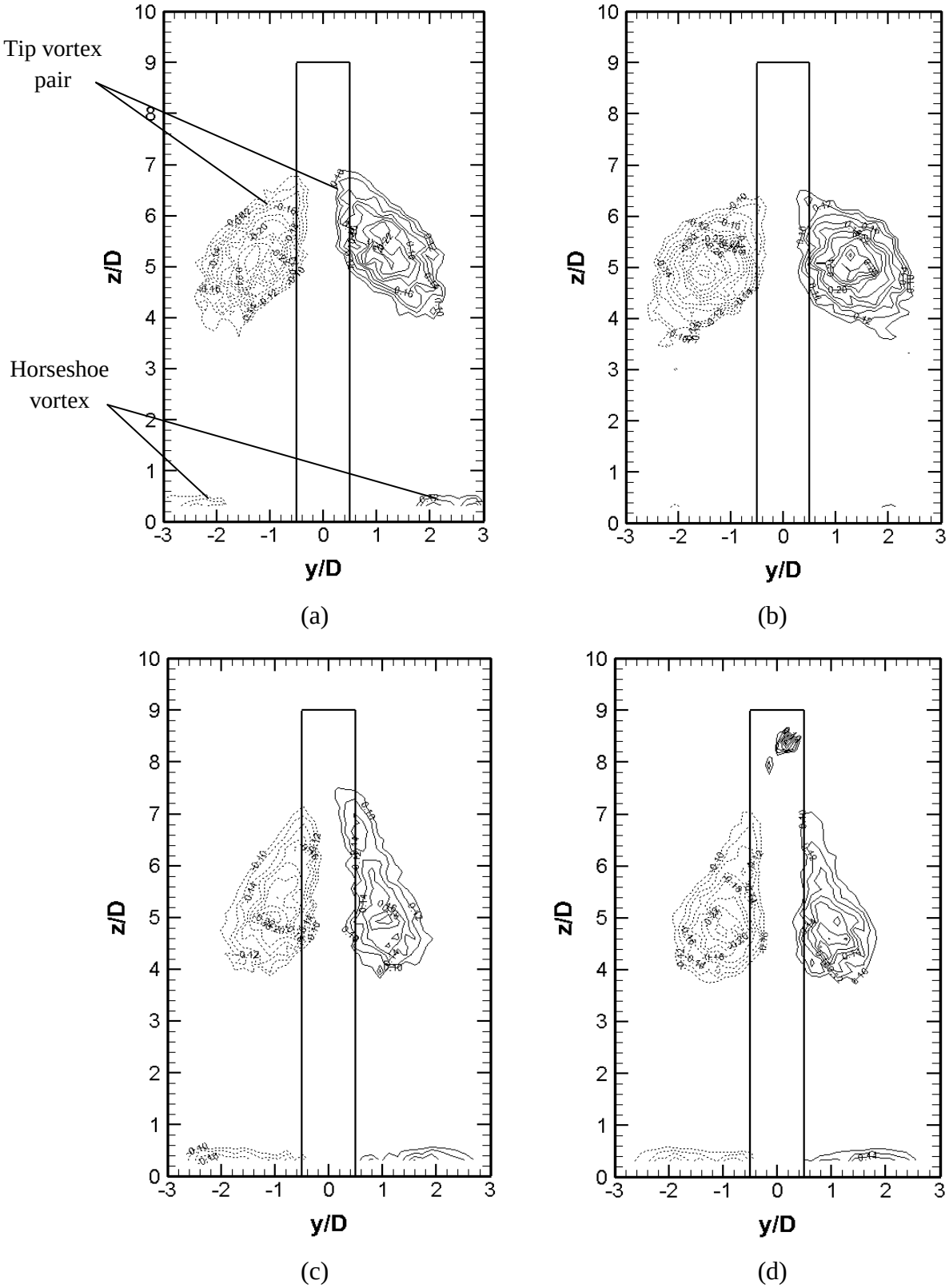

Figure 5.5: Non-dimensional, time-averaged streamwise vorticity contours in the wake of the square prism, AR = 9, x/D = 10: (a) L/D = 0, (b) L/D = 1, (c) L/D = 3, (d) L/D = 5, (e) L/D = 7. Contour increment of $\omega_x D/U_\infty$ = 0.02. Solid lines represent positive (CCW) vorticity; dashed lines represent negative (CW) vorticity.

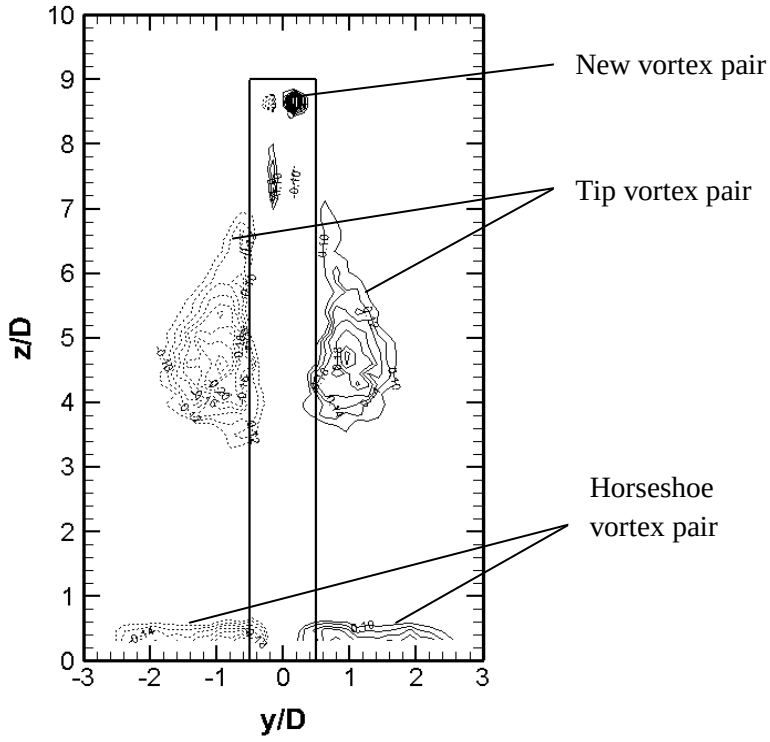

(e)

Figure 5.5 (continued)

vortex pair near the prism's free end (solid lines represent positive (CCW) vorticity, dashed lines represent negative (CW) vorticity). This represents the tip vortex structures. The base vortex pair usually found within the boundary layer closer to the ground plane for the finite circular cylinder (Sumner et al., 2004) is absent. Another distinct feature is the presence of the horseshoe vortex within the boundary layer. In the finite circular cylinder experiments of Sumner et al., (2004), the horseshoe vortex was weaker and was not observed.

For the prism-splitter plate combination of L/D = 1, Figure 5.5(b), the counter-rotating vortex pair near the prism's free end becomes more rounded in shape and closer to the ground plane. The horseshoe vortex is nearly absent in this figure. With L/D = 3, Figure 5.5(c), the counter-rotating vortex pair now becomes elongated (pulled) upwards by the splitter plate as a result of the additional drag induced by the plate. Also, the horseshoe vortex appears closer to the wake centreline as a result of the entrainment (Section 5.2.3) caused by the plate which

pulls the horseshoe vortex inwards. For longer splitter plates, $L/D \geq 5$, Figure 5.5(d,e), additional vortices induced by the plate-wake interaction are found very close to the free end (tip) of the prism. This is similar to what was observed for the wall-normal mean velocity (Figure 5.4(d,e)).

5.3 Wake Measurements for AR = 5

Similar to AR = 9 (Section 5.2), velocity vector field, streamwise mean velocity, cross-stream mean velocity contours, wall-normal mean velocity contours, and the time-averaged streamwise vorticity contours were obtained for the finite square prism of AR = 5 (represents a different wake structure). The results are presented below.

5.3.1 Velocity Vector Fields

The time-averaged mean cross-stream velocity vector field for AR = 5 is shown in Figure 5.6. For the no splitter plate ($L/D = 0$) case, Figure 5.6(a), the velocity vector field at $x/D = 10$ shows a strong downwash flow behind the prism and below the free end (tip), which extends to the ground plane. Like AR = 9, no noticeable upwash flow from the ground plane was seen near the ground plane. This contrasts with what was observed for a finite circular cylinder of the same aspect ratio (AR = 5) but similar to a finite circular cylinder of AR = 3 (Sumner et al., 2004). The flow forms a cyclic flow on both sides of the prism.

With a splitter plate of length $L/D = 1$, Figure 5.6(b), no appreciable difference is observed. However, the downwash flow becomes weaker as the splitter plate length increases, $L/D \geq 3$ especially at the upper wake (Figure 5.6(c,d,e)), and the cyclic flow on both sides of the prism disappears (pushed down).

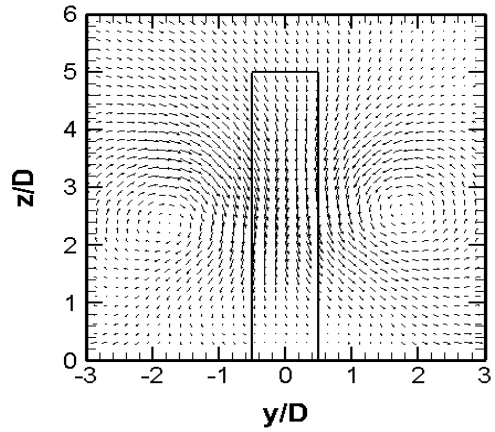

(a)

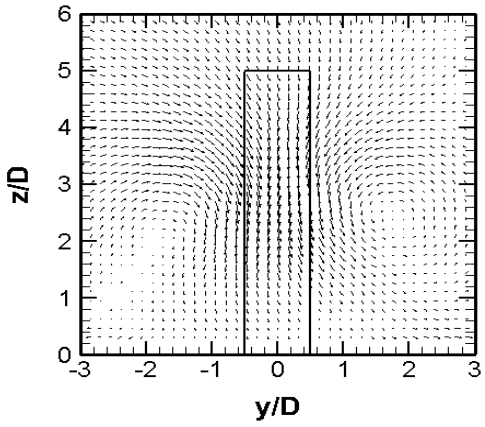

(b)

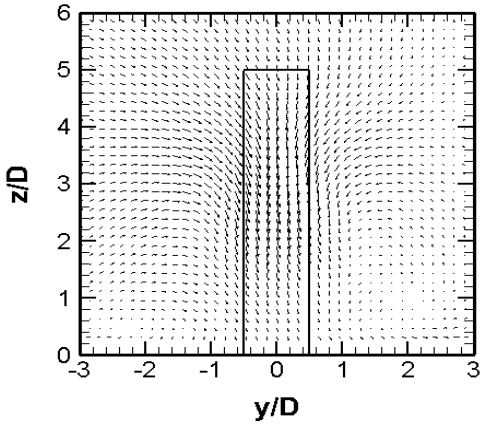

(c)

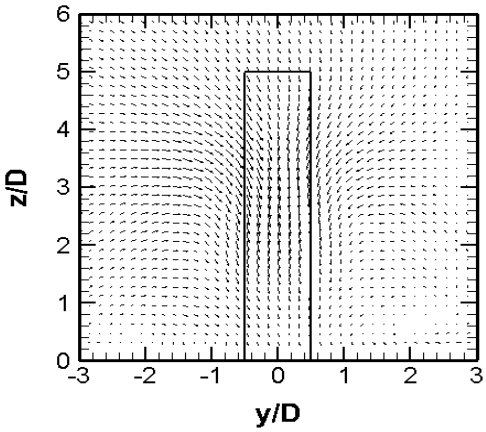

(d)

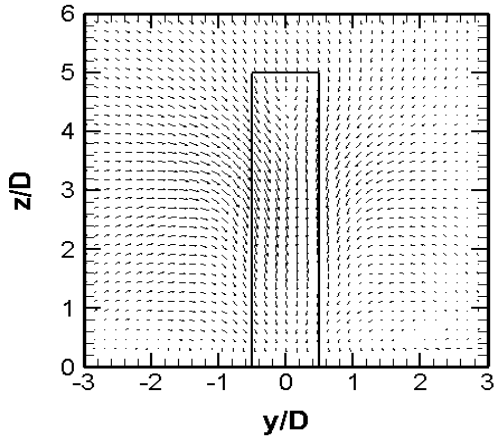

(e)

Figure 5.6: Mean velocity vector field in the wake of the square prism, AR = 5, x/D = 10: (a) L/D = 0, (b) L/D = 1, (c) L/D = 3, (d) L/D = 5, (e) L/D = 7.

5.3.2 Streamwise Mean Velocity

The time-averaged streamwise velocity field ($\overline{U}/U_\infty$) in the cross-stream (y-z) plane of prism AR = 5 is shown as a contour plot in Figure 5.7. For the no splitter plate (L/D = 0) case, Figure 5.7(a), the lowest mean streamwise velocities occur very close to the ground plane and the concentrated region close to the prism's mid-height is absent. This shows a different wake structure from AR = 9. These features contrast with that of a finite circular cylinder of the same aspect ratio but instead appear similar to that of AR = 3 (Adaramola et al., 2006). In addition, the lateral (y-direction) spread of the wake width is greater than for the prism of AR = 9 and for a finite circular cylinder of AR = 5 (Adaramola et al., 2006). Also, a double peak shape was obtained for the prism of AR = 5, suggesting a different wake structure compared to the AR = 9 prism and a finite circular cylinder of the same aspect ratio (AR = 5).

With a splitter plate of length L/D = 1, Figure 5.7(b), there is a noticeable effect of the plate. The double peak disappears as a result of a weaker downwash. For longer plates, $L/D \geq 3$, Figure 5.7(c,d,e), the wake of the plate becomes noticeable, the wake is stretched along the prism height (up to the prism's free end), the wake width becomes narrower, and the lowest mean streamwise velocities are higher, i.e. a reduction in velocity deficit. This contrasts with what was observed for AR = 9.

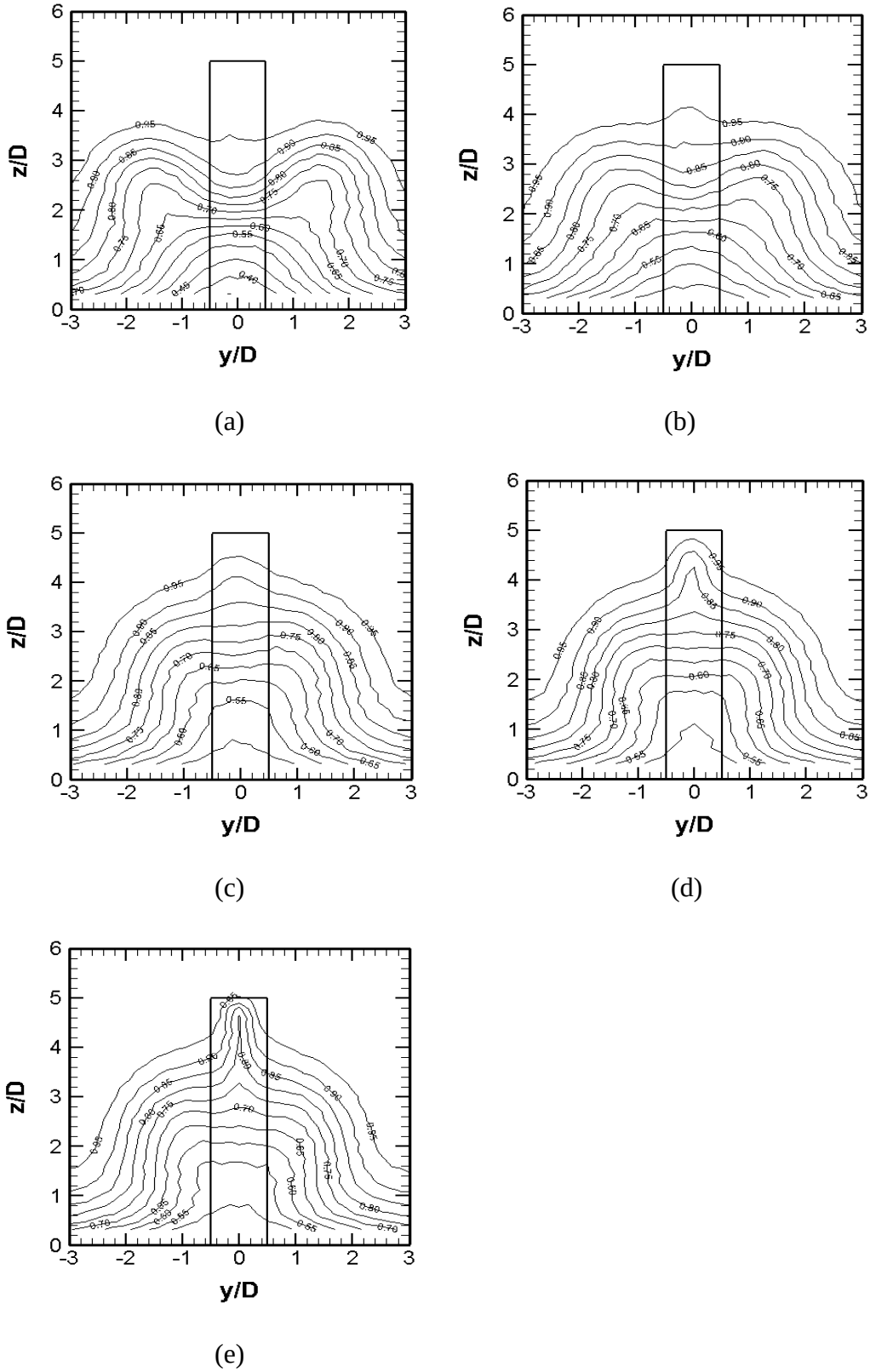

Figure 5.7: Streamwise mean velocity contours in the wake of the square prism, AR = 5, x/D = 10: (a) L/D = 0, (b) L/D = 1, (c) L/D = 3, (d) L/D = 5, (e) L/D = 7. Contour increment of $\overline{U}/U_\infty$ = 0.05.

5.3.3 Cross-stream Mean Velocity

The time-averaged cross-stream velocity field ($\overline{V}/U_\infty$) in the cross-stream (y-z) plane for AR = 5 is shown as a contour plot in Figure 5.8. For the no splitter plate (L/D = 0) case, Figure 5.8(a), flow is entrained towards the wake centreline especially in the upper wake. However, close to the ground plane, the flow direction is spreading outward. This is a distinct behaviour and supports why the wake width is wider than for AR = 9 and for a circular cylinder of the same aspect ratio.

With a short splitter plate, L/D = 1, Figure 5.8(b), no significant difference was observed for the upper wake; however, the lower wake cross-stream velocity becomes much weaker. As the splitter plate length increases, L/D = 3, Figure 5.8(c), a very noticeable change occurs. Entrainment towards the middle of the wake now occurs over the entire wake, i.e. all inward velocity gradually builds up. This is an indication of a strong velocity towards the splitter plate. This becomes stronger as the plate length increases, $L/D \geq 5$ (Figure 5.8(d,e)).

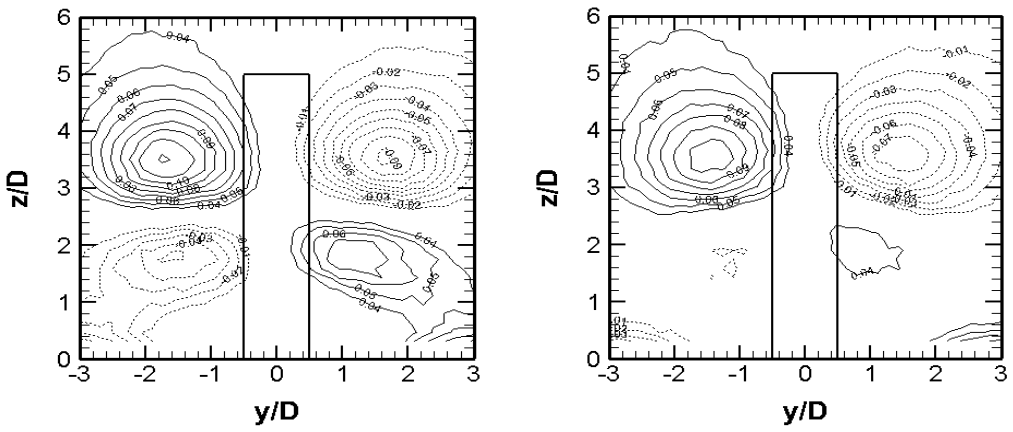

(a) (b)

Figure 5.8: Cross-stream mean velocity contours in the wake of the square prism, AR = 5, x/D = 10: (a) L/D = 0, (b) L/D = 1, (c) L/D = 3, (d) L/D = 5, (e) L/D = 7. Contour increment of $\overline{V}/U_\infty$ = 0.01. Solid lines represent positive and dashed lines represent negative velocities.

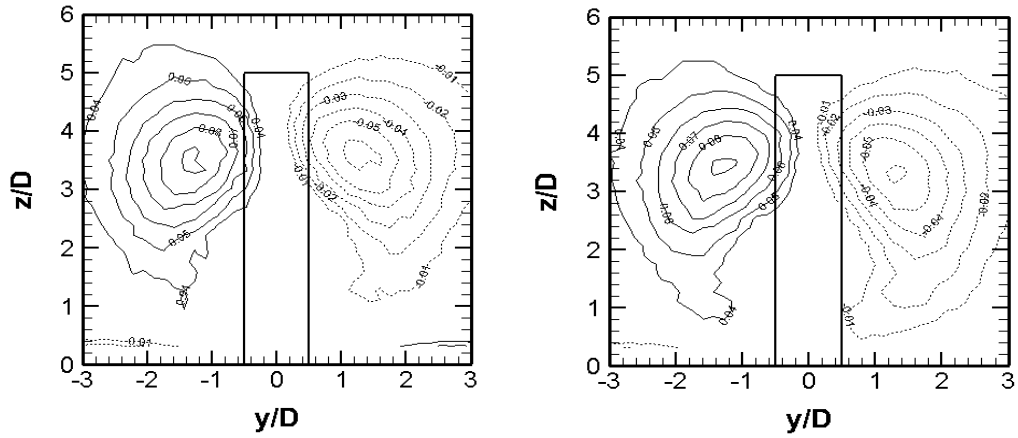

(c) (d)

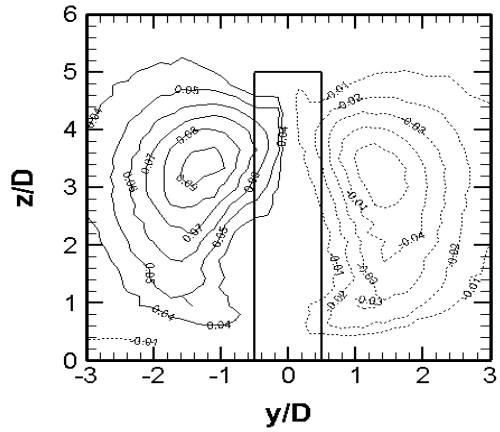

(e)

Figure 5.8 (continued)

5.3.4 Wall-normal Mean Velocity

The time-averaged wall-normal velocity (vertical) field ($\overline{W}/U_\infty$) in the cross-stream (*y*-*z*) plane for AR = 5 is shown as a contour plot in Figure 5.9. For the no splitter plate (L/D = 0) case, Figure 5.9(a), the presence of a strong downwash velocity which originates from the prism's free end and descends into the wake is observed. Like AR = 9, the upwash velocity field is absent, which contrasts with what is observed for a finite circular cylinder of the same aspect ratio (Sumner et al., 2004). When compared with AR = 9, the downwash velocity is

weaker (wider downwash region) and extends to the ground plane. This is another characteristic of the distinct wake structure of the AR = 5 prism.

For the prism-splitter plate combination of L/D = 1, Figure 5.9(b), the downwash region becomes narrower, which contrasts with AR = 9. With $3 \leq L/D \leq 5$, Figure 5.9(c,d), the splitter plate further narrows the downwash region. For a longer splitter plate, L/D = 7, Figure 5.9(e), a small downwash region close to the free end is observed. This is due to the induced flow by the splitter plate.

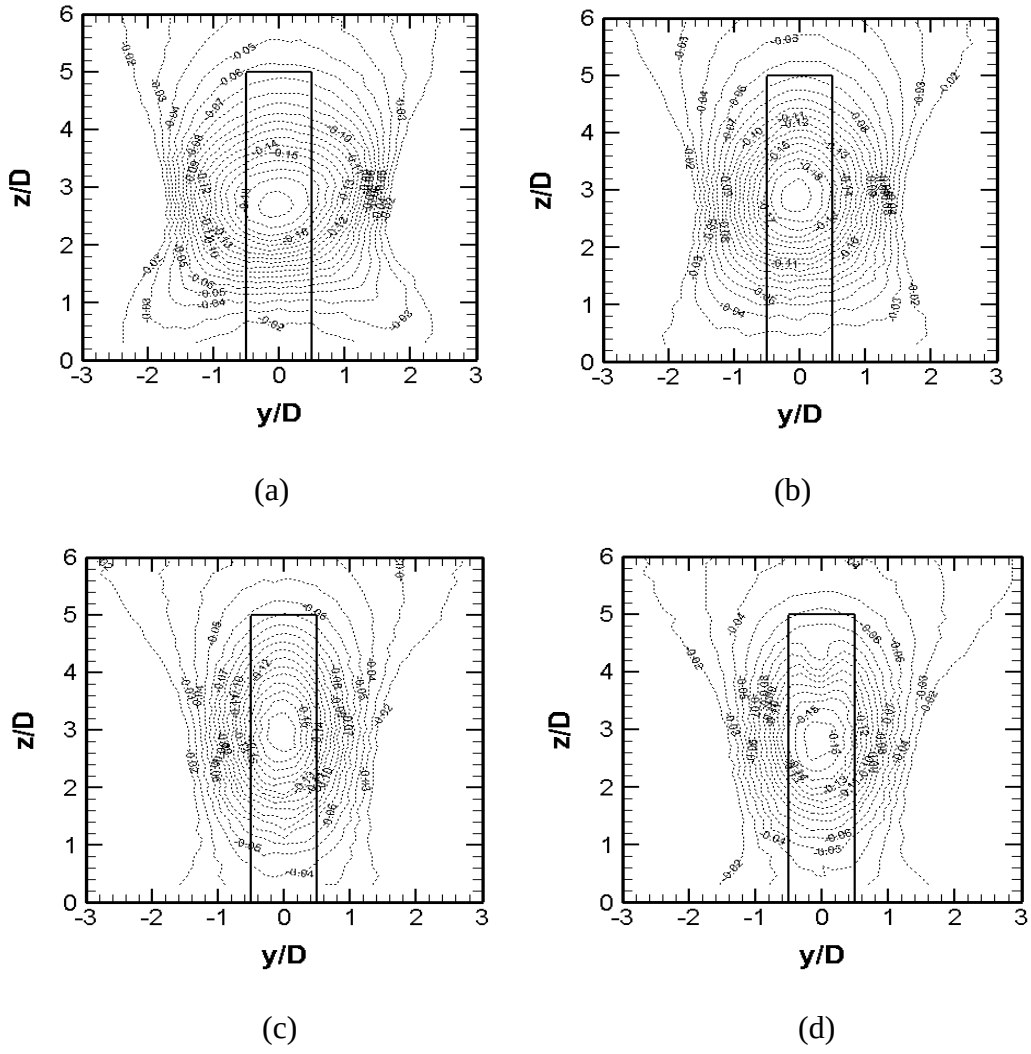

Figure 5.9: Wall-normal mean velocity contours in the wake of the square prism, AR = 5, x/D = 10: (a) L/D = 0, (b) L/D = 1, (c) L/D = 3, (d) L/D = 5, (e) L/D = 7. Contour increment of $\overline{W}/U_\infty$ = 0.01. Dashed lines represent negative (downward) velocity.

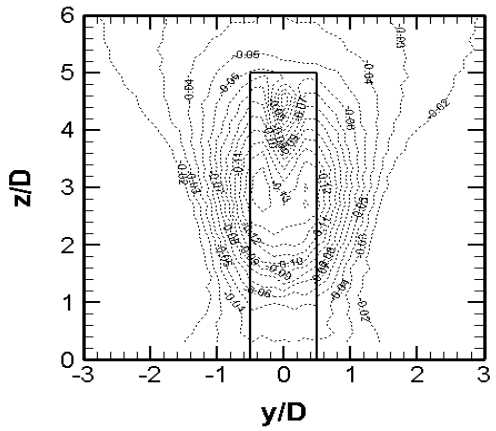

(e)

Figure 5.9 (continued)

5.3.5 Time-averaged Streamwise Vorticity

The time-averaged streamwise vorticity field expressed in dimensionless form as $\omega_x D/U_\infty$ in the cross-stream (y-z) plane for AR = 5 is shown in Figure 5.10. For L/D = 0 Figure 5.10(a), the vorticity field shows a counter-rotating vortex pair (the tip vortex structures) near the prism's free end. These structures are more circular in shape when compared with the prism of AR = 9. The base vortex pair found within the boundary layer closer to the ground plane for the finite circular cylinder of the same aspect ratio is absent. This is similar to what was observed for a circular cylinder of AR = 3 (Sumner et al., 2004). The horseshoe vortex within the boundary layer is also absent.

For the prism-splitter plate combination of L/D = 1, Figure 5.10(b), the counter-rotating vortex pair near the prism's free end has become more rounded in shape and weaker. The horseshoe vortex appears (though very weak). With L/D = 3, Figure 5.10(c), the counter-rotating vortex pair is being stretched upward (inclined to the wake centreline axis) by the splitter plate as a result of the additional drag induced by the plate. Also, the horseshoe vortex appears closer to the wake centreline as a result of the entrainment caused by the plate which pulls on the horseshoe vortex legs. For longer splitter plates, $L/D \geq 5$, Figure 5.10(d,e),

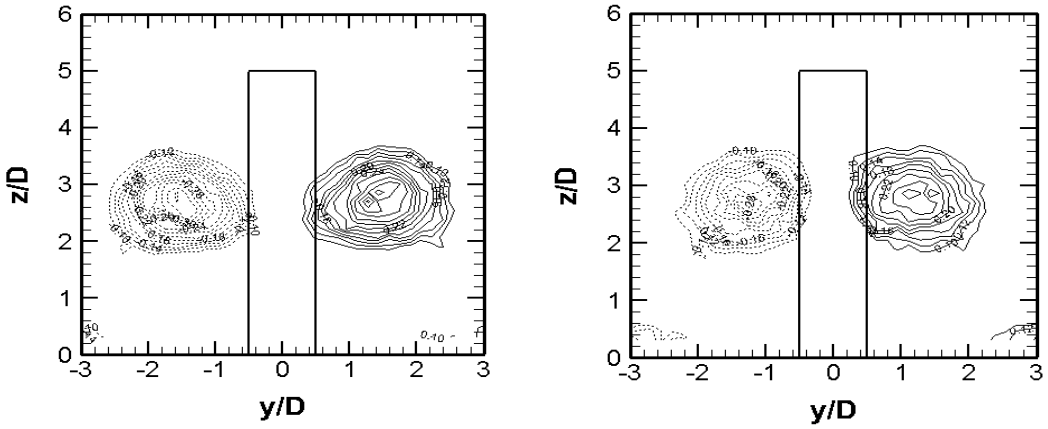

(a) (b)

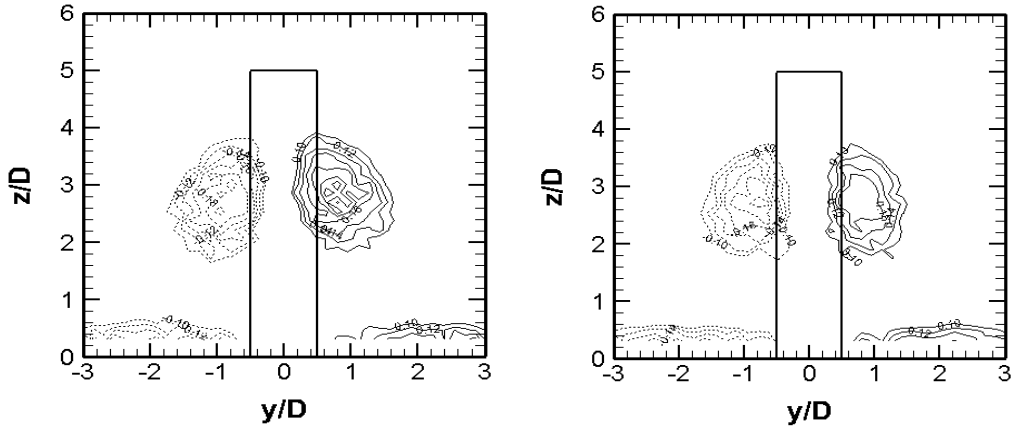

(c) (d)

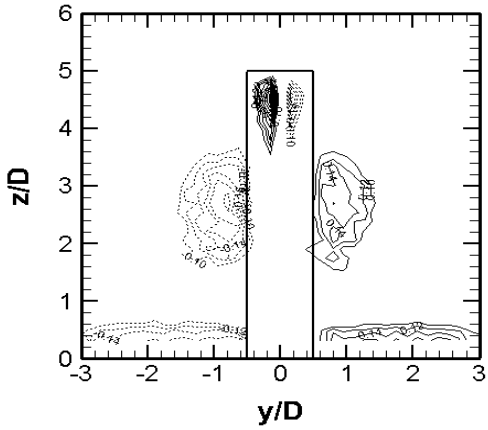

(e)

Figure 5.10: Non-dimensional, time-averaged streamwise vorticity contours in the wake of the square prism, AR = 5, x/D = 10: (a) L/D = 0, (b) L/D = 1, (c) L/D = 3, (d) L/D = 5, (e) L/D = 7. Contour increment of $\omega_x D/U_\infty$ = 0.02. Solid lines represent positive (CCW) vorticity; dashed lines represent negative (CW) vorticity.

additional vortices induced by the plate-wake interaction are found very close to the free end (tip) of the prism (similar to AR = 9).

5.4 Summary

The effects of a splitter plate on the mean velocity fields in the wake of finite square prisms of AR = 9 and 5 were investigated. For the finite square prism with no splitter plate ($L/D = 0$), a strong downwash flow was observed behind both prisms at $x/D = 10$. For AR = 9, the downwash weakens along the prism axis towards the ground plane. In contrast, the downwash flow for AR = 5 extends to the ground plane which suggests a different wake structure compared to the prism of AR = 9. For both prisms, no noticeable upwash flow from the ground plane was observed. With a splitter plate of length $L/D > 1$, downwash flow becomes weaker especially at the upper wake for the two aspect ratios.

Time-averaged measurements of the wake velocities (streamwise, cross-stream and wall-normal) and streamwise vorticity fields indicate the presence of a counter-rotating vortex pair near the prism's free end which represents the tip vortex structures. The tip vortex structures were found for the two aspect ratios tested and become inclined to the wake centreline axis, i.e. stretched upward when splitter plate was installed. No base vortex pair was observed and the horseshoe vortex appears for $L/D \geq 3$. For the streamwise mean velocity, the splitter plate ($L/D \geq 1$) narrows the wake especially close to the ground plane by stretching the wake along the prism height hence flow around the prism becomes more two-dimensional. The cross-stream mean velocity indicates that the flow is being entrained towards the wake centreline especially in the upper wake. However, with a splitter plate $L/D \geq 3$, the entrainment towards the centreline occurs over the entire wake height. The wall-normal mean velocity structure is similar to what was observed for the streamwise velocity vector field for both aspect ratios i.e. strong downwash, absence of upwash, downwash

extends to the ground plane for AR = 5 and downwash region becomes narrower for both prisms with $L/D \geq 3$.

CHAPTER SIX

CONCLUSIONS AND RECOMMENDATIONS

6.1 Conclusions

Passive bluff body flow control devices have been investigated for many decades and are applied in experiments. One such device is the splitter plate. The effectiveness of splitter plates at reducing the drag force and controlling vortex formation and shedding has been studied for two-dimensional bluff bodies (e.g. infinite circular cylinders and infinite prisms). It has been shown that the splitter plate influences the behaviour and interaction of the shear layers in the near-wake region and therefore suppresses vortex shedding and lowers the mean drag coefficient. Its effectiveness is sensitive to the plate length, L/D, thickness, T/D, gap, G/D, and location (downstream or upstream).

In the present study, the effect of a wake-mounted splitter plate on the flow around a finite-height surface-mounted square prism was studied experimentally. The experiments were carried out in a low-speed wind tunnel at Reynolds numbers of Re = 7.4×10^4 (corresponding to a freestream velocity of U_∞ = 40 m/s) and Re = 3.7×10^4 (corresponding to a freestream velocity of U_∞ = 20 m/s) for aspect ratios of AR = 9, 7, 5 and 3. The boundary layer thickness on the ground plane relative to the side length of the square prism was δ/D = 1.5. The splitter plates were mounted on the wake centreline with negligible gap (0.5 mm) between the prism base and the plate's leading edge. Splitter plate lengths relative to the prism side length ranged from L/D = 1 to 7 (1, 1.5, 2, 3, 5 and 7), T/D = 0.1 to 0.15, and the plate height was always equal to the prism height, i.e. H_{sp}/H = 1. Measurements of the mean drag force coefficient and vortex shedding frequency (at Re = 7.4×10^4) were obtained with a force balance and a single-component hot-wire anemometry, respectively. Strouhal number,

St, and power spectral measurements were made at the prism's mid-height and along its height.

For a surface-mounted finite-height circular cylinder, the splitter plate is less effective at reducing drag but more effective at suppressing vortex shedding when compared to an infinite cylinder (Igbalajobi et al., 2013). However, in addition to the plate's length, thickness and gap, its performance is also influenced by the cylinder aspect ratio, AR, boundary layer thickness, δ/D or δ/H, and possibly the plate height, H_{sp}/H (although this has not yet been investigated in the literature). To date, no specific information is available in the literature on how the splitter plate affects the drag and vortex shedding of a surface-mounted finite square prism and its wake structure.

For the finite square prism (without a splitter plate), it is noted that as the aspect ratio increases, C_D increases to a maximum value at AR = 5, then decreases to a constant value for AR = 7 and 9. A splitter plate (a passive flow control device) was effective at reducing the mean drag coefficient as well as weakening or suppressing vortex shedding from the prisms. With a splitter plate of length L/D = 1, a slight reduction in the mean drag coefficient was observed for all the aspect ratios except for AR = 9 where there was a small increase in the C_D. For longer plates, $L/D \geq 1.5$, the C_D for AR = 9 decreased to the no-splitter-plate value and then followed the C_D reduction trend like the other prisms (AR = 7, 5 and 3). Irrespective of the AR, C_D tended to become constant for $L/D \geq 3$. In general, the C_D decreased as L/D was increased. The highest reduction in drag was realized for square prisms AR $\leq$ 5 with splitter plates of $L/D \geq 5$, where there was an 11% drag reduction. For the prisms of AR = 9 and AR = 7, the drag reduction was much lower and almost negligible for some prism-plate combinations. In addition, the AR = 3 and 5 prisms followed a particular drag reduction pattern (see Figure 4.1(b)) that suggested the same flow behaviour and which was distinct from the other two aspect ratios. This behaviour supported the existence of a different flow

pattern for these two prisms which suggested that, for the present experimental conditions, AR = 3 and 5 were below the critical aspect ratio.

Based on these thesis results, it can be concluded that a suitably selected splitter plate (of particular length ratio, L/D) can be used to reduce the mean drag force coefficient of a surface-mounted finite-height square prism. However, when compared with an infinite cylinder and infinite prism, it is less effective as a passive flow control device. This may be due to the complexity and three-dimensionality of the flow field around the finite square prism. In contrast, the splitter plate is a more effective drag reduction device for a finite square prism than a finite circular cylinder.

On all four prisms tested, the splitter plates were effective at reducing the magnitude of the Strouhal number, and either weakening or suppressing vortex shedding, depending on the prism's AR and the plate's length, L/D. For AR = 3, a splitter plate of length $L/D = 2$ was sufficient to suppress the vortex shedding at the prism's mid-height. For AR > 3, a splitter plate of length $L/D = 3$ completely suppressed vortex shedding at the prism's mid-height. In all, a splitter plate of length $L/D \geq 3$ completely suppressed vortex shedding at the prism's mid-height for all the prisms tested. Shorter plate lengths only reduced the magnitude of the Strouhal number.

Strouhal numbers along the prisms height were measured. Irrespective of the aspect ratio, a splitter plate of length $L/D \geq 3$ was sufficient to suppress vortex shedding along the entire height of the prisms. More broad-banded vortex shedding peaks (an indication of weaker vortex shedding activity) were seen before vortex suppression occurred.

Based on these results, it can be concluded that a suitably selected splitter plate (of particular length ratio, L/D) can be used to suppress vortex shedding of a surface-mounted finite-height square prism. When compared with an infinite cylinder and infinite prism, the splitter plate is a more effective passive flow control device for a finite square prism. In

contrast, the splitter plate is less effective vortex shedding suppression device for a finite square prism when compared to a finite circular cylinder, especially for small aspect ratios (AR $\leq$ 7). This could be as a result of the different wake structures and recirculation zones of these two bluff bodies.

In order to have a better understanding of the wake structure behind the prism, the time-averaged wake velocity field measurements were taken. The measurements were made with a seven-hole probe. The experiments were conducted at a Reynolds number of Re = 3.7×10^4 for aspect ratios of AR = 9 and AR = 5 only. These aspect ratios represent an example of the two main wake structures for the finite square prism. Splitter plate lengths of L/D = 1, 3, 5 and 7 only were used.

Contrasting wake structures were observed for the two aspect ratios tested. For the velocity vector field, a strong downwash flow behind, and from the free end of the prism, was observed for both prisms. However, the flow reached the vicinity of the ground plane for AR = 5, thereby suppressing the upwash flow. With AR = 9, the downwash flow never reached the vicinity of the ground plane as it weakened towards the middle of the wake. No noticeable upwash flow from the ground was observed for AR = 9 as well. With a splitter plate of considerable length, L/D > 1, downwash becomes weaker for both prisms.

For the streamwise, cross-stream, and wall normal velocities, the splitter plate stretched (drew upwards) the wake along the prism height, and the wake width became narrower especially closer to the ground plane. This made it possible for the reduction in the mean drag coefficient. This is because the flow is entrained towards the wake centreline, narrowing the wake. The horseshoe vortex appeared closer to the wake centreline as a result of the entrainment, which pulled the horseshoe vortex inwards.

In general, the results of this research indicate that a wake-mounted splitter plate (of suitable length, L/D) can be effective at reducing the drag coefficient, and controlling,

weakening, or suppressing vortex shedding from a surface-mounted finite-height square prism. The results also give some information on the wake of a finite square prism-plate combination.

6.2 Recommendations

The effects of splitter plates on the flow around square prisms have not been extensively studied. Hence, variations of some parameters are needed to further understand the effectiveness of the splitter plate. In the present study, only the splitter plate lengths were varied while other parameters remained unchanged throughout the experiments. For further studies (future work), the following should be taken into consideration:

(i) Varying the height of the splitter plate relative to the prism's height i.e. H_{sp}/H, to see if the same effects can be achieved with a shorter plate height; the shorter plate height may mean less influence on the downwash velocity field;

(ii) Studying the combined effect of angle of incidence, aspect ratio and splitter plate, although the positioning of the splitter plate may be problematic when the prism is angled relative to the oncoming flow;

(iii) Moving the splitter plate further downstream thereby increasing the gap, G/D, between the prism's rear surface and the plate's leading edge;

(iv) Further study of what happens within the recirculation zone behind the prism (with splitter plate installed), including making velocity measurements closer to the prism and the splitter plate which may require a different velocity measurement technique, such as particle image velocimetry (PIV) or laser Doppler velocimetry (LDV), since the flow may be recirculating closer to the prism and plate;

(v) Examine the effect of hot-wire probe location or position on the vortex shedding and time average velocity measurements, given that a fixed position was used in the present experiments, similar to Igbalajobi et al. (2013).

REFERENCES

Adaramola, M.S., Akinlade, O.G., Sumner, D., Bergstrom, D.J., and Schenstead, A.J., 2006. "Turbulent wake of a finite circular cylinder of small aspect ratio", *Journal of Fluids and Structures*, Vol. 22, pp. 919-928.

Adaramola, M.S., Sumner, D., and Bergstrom, D.J., 2010. "Effect of velocity ratio on the streamwise vortex structures in the wake of a stack", *Journal of Fluids and Structures*, Vol. 26, pp. 1-18.

Akilli, H., Sahin, B., and Tumen, N., 2005. "Suppression of vortex shedding of circular cylinder in shallow water by a splitter plate", *Flow Measurement and Instrumentation*, Vol. 16, pp. 211-219.

Ali, M.S.M., Doolan, C.J., and Wheatley, V., 2011. "Low Reynolds number flow over a square cylinder with a splitter plate", *Physics of Fluids*, Vol. 23, 033602, 12 pp.

Anderson, E.A., and Szewczyk, A.A., 1997. "Effects of a splitter plate on the near wake of a circular cylinder in 2 and 3-dimensional flow configurations", *Experiments in Fluids*, Vol. 23, pp. 161-174.

Apelt, C.J., West, G.S., and Szewczyk, A.A., 1973. "The effects of wake splitter plates on the flow past a circular cylinder in the range $10^4 < R < 5\times10^4$", *Journal of Fluid Mechanics*, Vol. 61, pp. 187-198.

Apelt, C.J., and West, G.S., 1975. "The effects of wake splitter plates on bluff-body flow in the range $10^4 < R < 5\times10^4$: Part 2", *Journal of Fluid Mechanics*, Vol. 71, pp. 145-160.

Bearman, P.W., and Trueman, D.M., 1972. "An investigation of the flow around rectangular cylinders", *The Aeronautical Quarterly*, Vol. 23, pp. 229-237.

Bryer, D.W., and Pankhurst, R.C, 1971. *Pressure-Probe Methods for Determining Wind Speed and Flow Direction*, National Physical Laboratory, Department of Trade and Industry, The Campfield Press, St. Albans, UK.

Cardell, G.S., 1993. “Flow past a circular cylinder with a permeable splitter plate”, Ph.D. Thesis, California Institute of Technology.

Choi, H., Jeon, W.P., and Kim, J., 2008. “Control of flow over a bluff body”, *Annual Review of Fluid Mechanics*, Vol. 40, pp. 113-139.

Dehkordi, B.G., and Jafari, H.H., 2010. “On the suppression of vortex shedding from circular cylinders using detached short splitter-plates”, *ASME Journal of Fluids Engineering*, Vol. 132, 044501, 4 pp.

Dutta, S., Muralidhar, K., and Panigrahi, P.P., 2003. “Influence of the orientation of a square cylinder on the wake properties”, *Experiments in Fluids*, Vol. 34, pp. 16-23.

Gad-el-Hak, M., 2000. *Flow Control: Passive, Active, and Reactive Flow Management*, Cambridge University Press, Cambridge, UK.

Gallington, R.W., 1980. “Measurement of very large flow angles with non-nulling seven-hole probe”, *Aeronautics Digest*, USAFA-TR-80-17, pp. 60-88.

Gerrard, J.H., 1966. “The mechanics of the formation region of vortices behind bluff bodies”, *Journal of Fluid Mechanics*, Vol. 25, pp. 401-413.

Hasan, M.A.Z., and Budair. M.O., 1994, “Role of splitter plates in modifying cylinder wake flows”, *AIAA Journal*, Vol. 32, pp. 1992-1998.

Huang, R.F., Lin, B.H., and Yen, S.C., 2010. “Time-averaged topological flow patterns and their Influence on vortex shedding of a square cylinder in crossflow at incidence”, *Journal of Fluids and Structures*, Vol. 26, pp. 406-429.

Hwang, J.Y., Yang, K.S., and Sun, S.H., 2003. “Reduction of flow-induced forces on a circular cylinder using a detached splitter plate”, *Physics of Fluids*, Vol. 15, pp. 2433-2436.

Igarashi, T., 1984. “Characteristics of the flow around a square prism”, *Bulletin of the JSME*, Vol. 27, pp. 1858-1865.

Igbalajobi, A., McClean, J.F., Sumner, D., and Bergstrom, D.J., 2013. “The effect of a wake-mounted splitter plate on the flow around a surface-mounted finite-height circular cylinder”, *Journal of Fluids and Structures*, Vol. 37, pp. 185-200.

Kawamura, T., Hiwada, M., Hibino, T., Mabuchi, T., and Kumada, M., 1984. “Flow around a finite circular cylinder on a flat plate”, *Bulletin of the JSME*, Vol. 27, pp. 2142-2150.

Knisely. C.W., 1990. “Strouhal numbers of rectangular cylinders at incidence: a review and new data”, *Journal of Fluids and Structures*, Vol. 4, pp. 187-196.

Kwon, K., and Choi, H., 1996. “Control of laminar vortex shedding behind a circular cylinder using splitter plates”, *Physics of Fluids*, Vol. 8, pp.479-486.

Lee, B.E., 1975. “The effect of turbulence on the surface pressure field of a square prism”, *Journal of Fluid Mechanics*, Vol. 69, pp. 263-282.

Lyn, D.A., Einav, S., Rodi, W., and Park, J.H., 1995. “A laser-Doppler velocimetry study of ensemble-averaged characteristics of the turbulent near wake of a square cylinder”, *Journal of Fluid Mechanics*, Vol. 304, pp. 285-319.

Mansingh, V., and Oosthuizen, P.H., 1990. “Effects of splitter plates on the wake flpw behind a bluff body”, *AIAA Journal*, Vol. 28, pp. 778-783.

Martinuzzi, R., and Tropea, C., 1993. “The flow around surface-mounted, prismatic obstacles in a fully developed channel flow”, *ASME Journal of Fluids Engineering*, Vol. 115, pp. 85-92.

McClean, J.F., and Sumner, D., 2012. “Aerodynamic forces and vortex shedding for surface-mounted finite square prisms and the effects of aspect ratio and incidence angle”, Proceedings of the ASME 2012 Fluids Engineering Division Summer Meeting (FEDSM2012), Rio Grande, Puerto Rico, USA, July 8-12, 2012, Paper No. FEDSM2012-72005.

McClean, J. F., and Sumner, D., 2014. “An experimental investigation of aspect ratio and incidence angle effects for the flow around surface-mounted finite-height square prisms”, *ASME Journal of Fluids Engineering*, Vol. 136, 081206, 10 pp.

Nakamura, Y., 1996. “Vortex shedding from bluff bodies with splitter plates”, *Journal of Fluids and Structures*, Vol. 10, pp. 147-158.

Norberg, C., 1993. “Flow around rectangular cylinders: Pressure forces and wake frequencies”, *Journal of Wind Engineering and Industrial Aerodynamics*, Vol. 49, pp. 187-196.

Obasaju, E.D., 1983. “An investigation of the effects of incidence on the flow around a square section cylinder”, *The Aeronautical Quarterly*, Vol. 34, pp. 243-259.

Okamoto, S., Tsunola, K., Takagi, T., Okada, E., and Kitani, K., 1995. “Turbulent near wake behind square cylinder of finite length on ground plane”, Proceedings of the ASME/JSME Fluids Engineering and Laser Anemometry Conference and Exhibition, FED-Vol. 229, pp. 195-216.

Park, W.C., and Higuchi, H., 1998. “Numerical investigation of wake flow control by a splitter plate”, *KSME International Journal*, Vol. 12, pp. 123-131.

Rostamy, N., 2012. “Fundamental studies of the wake structure for surface-mounted finite-height cylinders and prisms”. Ph.D. Thesis, Department of Mechanical Engineering, University of Saskatchewan.

Rostamy, N., McClean, J.F., Sumner, D., Bergstrom, D.J., and Bugg, J.D., 2012. “Local flow field of a surface-mounted finite square prism,” 7th International Colloquium on Bluff Body Aerodynamics and Applications (BBAA7), Shanghai, China, September 2-6, 2012.

Sakamoto, H., Moriya, M., Taniguchi, S., and Arie, M., 1982. "The form drag of a three dimensional bluff bodies immersed in turbulent boundary layers", *ASME Journal of Fluids Engineering*, Vol. 104, pp. 326-334.

Sarioglu, M., and Yavuz, T., 2000. "Vortex shedding from circular and rectangular cylinders placed horizontally in a turbulent flow", *Turkish Journal of Engineering and Environmental Sciences*, Vol. 24, pp. 217-228.

Sarode, R.S., Gai, S.L., and Ramesh, C.K., 1981. "Flow around circular- and square-section models of finite height in a turbulent shear flow", *Journal of Wind Engineering and Industrial Aerodynamics*, Vol. 8, pp. 223-230.

Smits, A.J., 2000. *A Physical Introduction to Fluid Mechanics*, New York: John Wiley

Sumner, D., 2002. "A comparison of data-reduction methods for a seven-hole probe", *ASME Journal of Fluids Engineering*, Vol. 124**,** pp. 523-527.

Sumner, D., Heseltine, J.L., and Dansereau, O.J.P., 2004. "Wake structure of a finite circular cylinder of small aspect ratio", *Experiments in Fluids*, Vol. 37, pp. 720-730.

Taylor, I., and Vezza, M., 1999. "Prediction of unsteady flow around square and rectangular section cylinders using discrete vortex method", *Journal of Wind Engineering and Industrial Aerodynamics*, Vol. 82, pp. 247-269

Unal, M.F., and Rockwell, D., 1987. "On vortex formation from a cylinder. Part 2. Control by splitter-plate interference", *Journal of Fluid Mechanics*, Vol. 190, pp. 513-529.

Wang, H.F., Zhou, Y., Chan, C.K., Wong, W.O., and Lam, K.S., 2004. "Flow structure around a finite-length square prism", Proceedings of the 15th Australasian Fluid Mechanics Conference, December 13-17, 2004.

White, F.M., 2003. *Fluid Mechanics*, 5th Edition, McGraw-Hill, New York.

Yen, S.C., and Yang, C.W., 2011. “Flow patterns and vortex shedding behaviour behind a square cylinder”, *Journal of Wind Engineering and Industrial Aerodynamics*, Vol. 99, pp. 868-878.

Yen, S.C., and Yang, C.W., 2012. “Characteristic flow field behind a square-cylinder using upstream mesh fences”, *ASME Journal of Fluids Engineering*, Vol. 134, 091202, 9 pp.

Zdravkovich, M.M., 1981. “Review and classification of various aerodynamic and hydrodynamic means for suppressing vortex shedding”, *Journal of Wind Engineering and Industrial Aerodynamics*, Vol. 7, pp. 145-189.

Zilliac, G.G., 1993. “Modelling, calibration, and error analysis of seven-hole pressure probes”, *Experiments in Fluids*, Vol. 14, pp. 104-120.